

Modeling of Solid Reaction Behavior in Direct Heated Rotary Kilns

Dissertation

For the award of the degree

Doktoringenieur

(Dr.-Ing.)

By

M. Sc. Abdulkadir Ahmed Alnour A.Abdelwahab

Date of birth: 04. April 1977 in Algrifa, Libya

Accepted by

The Faculty of Process and Systems Engineering
of the Otto-von-Guericke-University of Magdeburg

Reviewers:

Prof. Dr.-Ing. Frank Beyrau (Chairman)

Institute of Fluid Dynamics and Thermodynamics,
Universität Magdeburg, Germany.

Prof. Dr.-Ing. Fabian Herz (Reviewer and supervisor)

Institute of Fluid Dynamics and Thermodynamics,
Universität Magdeburg, Germany.

Prof. Dr.-Ing. Echehard Specht (Reviewer)

Institute of Fluid Dynamics and Thermodynamics,
Universität Magdeburg, Germany.

Prof. Dr.-Ing. Rayko Stanev (Reviewer)

Department of Physical Metallurgy and Thermal Equipment,
University of Sofia, Bulgaria

Submitted on : 02.06.2017

Graduation Colloquium on : 28.06.2017

Acknowledgements

Firstly, deepest gratitude and thanks goes to God, the almighty for giving me immense strength and confidence for the successful completion of my doctoral's (Alhamdulillah).

I would like to express my thankfulness and gratitude to my country **Libya** for the financial support during my research.

I would like to express my sincere gratitude and appreciation to my supervisor **Prof. Dr.-Ing. Fabian Herz**, for his continual support, encouragement and financial support. His knowledge, experience, guidance, and patience have also benefited me immensely. Further acknowledgment goes to **Prof. Dr.-Ing. Echehard Specht**, the person who have accepted me for doctoral study in OVGU Magdeburg and for teaching me invaluable knowledge throughout the course of my study. With his initial support, this great dream of mine can finally turn to reality and review my thesis

I would also like to express my deepest gratefulness to **Prof. Dr.-Ing. Rayko Stanev** for his repetitive support, for reviewing this dissertation and for valuable comments and suggestions.

I wish to thank all my colleagues in the Institute for Fluid Mechanics and Thermodynamics at Otto von Guericke University Magdeburg for their assistance, friendship and many happy and enjoyed times. Special thanks go to our friendly secretary; **Christin Hasemann** *for her help*.

I would like to thank all the Libyan friends in Magdeburg for their endless sharing and companionship, and also to all my friends in Magdeburg and anywhere else in Germany.

The continuous encouragement given by my loving parents, who brought me into the world and raised me, is greatly acknowledged and appreciated. All my friends and relatives in Libya, who have loved and supported me, are faithfully acknowledged.

Abdulkadir Abdelwahab, Magdeburg June 2017

Preface

This dissertation is submitted to Otto von Guericke University Magdeburg for the degree of Doctor of Engineer. The research described herein was conducted under the supervision of Prof. Dr.-Ing. Fabian Herz between July 2014 and June 2017. To the best of my knowledge, this work is original, except where suitable references are made to previous works. Neither this nor any substantially similar dissertation has been submitted for any degree, diploma or qualification at any other university or institution.

Abdulkadir Abdelwahab

Magdeburg, Germany

June, 2017

Abstract

Rotary kilns are extensively used industrially for thermal treatment of a variety of materials. There has been an ever higher demand on the optimization of these processes, which in turn requires an understanding of the interplay of various operational and design parameters in detail. Conventionally, empirical correlations are employed for optimization. However, efforts have also been made to simulate the processes theoretically. A process model was developed at the Otto-von-Guericke-University Magdeburg which has a capability of explaining the coupled phenomenon of heat transfer and bulk bed, motion behavior inside the rotary kiln. In this model, chemical reactions inside the bulk bed are not considered.

For this reason, the present work is focused on the reaction behavior in the bulk bed of rotary kilns. Eight different thermal processes are selected due to their industrial importance and analyzed including chemical bulk reactions. The reaction mechanisms of these processes are written in terms of conversion degrees which are obtained by using theoretical models from the literature. Different sets of ordinary differential equations explaining the reaction terms for each process are developed, which are then implemented in the system of equations presented in the overall process. The new developed “reaction process model” is programmed and numerically solved in MATLAB.

This new model predicts the axial temperature profile of the gas phase, bulk bed, surface of inner wall and the outer shell. It can also provide information on filling degree, residence time of solids, conversion degree (reaction behavior) and heat losses through the wall of the kiln. The model is validated with measurements on the industrial rotary kilns, experimental analysis at a pilot scale rotary kiln and literature data. The simulation results agree well with the data obtained from these different sources.

The new developed model can be used to predict the process behavior under the influence of the process parameters. Especially the quality of the product can be defined exactly. At the same time, it can assist in the optimization of the process as well as training of the personnel operating with the processes in rotary kilns.

Zusammenfassung

Drehrohröfen werden industriell für eine Vielzahl thermischer Behandlungen verschiedener Materialien eingesetzt. Es besteht ein hoher Bedarf an Optimierung solcher Drehrohröfen-Prozesse, was jedoch detaillierte Kenntnisse über das Zusammenspiel der verschiedenen Betriebs- und Designparameter erfordert. Üblicherweise werden empirische Korrelationen für die Optimierung herangezogen, wobei auch Fortschritte auf dem Gebiet der theoretischen Prozesssimulation gemacht wurden. An der Otto-von-Guericke-Universität Magdeburg wurde ein Prozessmodell entwickelt, mit dem sich die Zusammenhänge von Wärmeübertragung und Bewegungsverhalten des Feststoffs in Drehrohröfen beschreiben lassen. Dieses Modell berücksichtigt jedoch keine Feststoffreaktionen.

Aus diesem Grund liegt der Fokus dieser Arbeit auf dem Reaktionsverhalten des Feststoffbetts in Drehrohröfen. Acht verschiedene Thermoprozesse wurden auf Grund ihrer industriellen Bedeutung ausgewählt und hinsichtlich ihrer chemischen Feststoffreaktionen untersucht. Die Reaktionsmechanismen dieser Prozesse wurden auf Basis der Umsatzgrade beschrieben, welche mit Hilfe von theoretischen Modellen aus der Literatur ermittelt wurden. Es wurden gewöhnliche Differentialgleichungen zur Beschreibung der chemischen Reaktionen jedes Einzelprozesses aufgestellt und anschließend in einem Gleichungssystem zusammengefasst, um den Gesamtprozess abzubilden. Dieses neue „Reaktionsverlauf-Modell“ wurde mit MATLAB programmiert und numerisch gelöst.

Dieses neue Modell berechnet die axialen Temperaturprofile der Gasphase, des Feststoffbetts sowie der inneren und äußeren Mantelwand. Es liefert ebenfalls Informationen über den Füllungsgrad, die Verweildauer des Feststoffs, den Umsatzgrad (Reaktionsverhalten) sowie Wärmeverluste durch die Ofenwand. Das Modell wird mit Messungen an industriellen Drehrohröfen, experimentellen Untersuchungen an einer Pilotanlage und Daten aus der Literatur validiert. Die Simulation zeigt gute Übereinstimmung mit den Vergleichsdaten.

Das neu entwickelte Modell kann zur Vorhersage des Prozessverhaltens unter dem Einfluss verschiedener Prozessparameter genutzt werden. Dadurch lässt sich die Produktqualität exakt definieren. Zudem kann es zur Prozessoptimierung sowie zu Schulungszwecken im Umgang mit Drehrohröfen eingesetzt werden.

Table of Contents

Acknowledgement	II
Abstract	III
Zusammenfassung	IV
Table of contents	V
Nomenclature	VIII
Chapter 1 Introduction	1
1.1 Rotary kilns and its application	1
1.2 Problem statement	5
1.3 Thesis Outline	7
Chapter 2 Mathematical process model	9
2.1 Heat transfer	9
2.2 Solid transport in rotary kilns	14
2.2.1 Axial transport and residence time	14
2.2.2 Transverse motion of particles	15
2.3 Process model description	18
Chapter 3 Reaction terms within the bulk bed	25
3.1 Cement	25
3.1.1 Cement processing	25
3.1.2 Process model implementation	33

3.2 Limestone	36
3.2.1 Limestone processing	36
3.2.2 Process model implementation	39
3.3 Magnesite	43
3.3.1 Magnesite processing	43
3.3.2 Process model implementation	46
3.4 Dolomite	49
3.4.1 Dolomite processing	49
3.4.2 Process model implementation	49
3.5 Siderite	52
3.5.1 Siderite processing	52
3.5.2 Process model implementation	53
3.6 Titanium oxide	56
3.6.1 Titanium oxide processing	56
3.6.2 Process model implementation	58
3.7 Kaolin	61
3.7.1 Kaolin processing	61
3.7.2 Process model implementation	63
3.8 Aluminum dross	66
3.8.1 Aluminum dross processing	66
3.8.2 Process model implementation	67
Chapter 4 Experiments in a pilot rotary kilns	73
4.1 Experimental setup and procedure	73

4.2 Aluminum dross	77
4.3 Siderite	80
Chapter 5 Experiments in industrial rotary kiln based on literature data	83
5.1 Magnesite	83
5.1.1 Kiln and process parameters	83
5.1.2 Results and validation	84
5.2 Dolomite	87
5.2.1 Kiln and process parameters	87
5.2.2 Results and validation	88
5.3 Titanium dioxide	91
5.3.1 Kiln and process parameters	91
5.3.2 Results and validation	92
Chapter 6 Experiments in industrial rotary kilns	96
6.1 Cement	96
6.1.1 Kiln and process parameters	96
6.1.2 Results and validation	97
6.2 Limestone	100
6.2.1 Kiln and process parameters	100
6.2.2 Results and validation	101
6.3 Kaolin	104
6.3.1 Kiln and process parameters	104
6.3.2 Results and validation	105

Chapter 7: Conclusion and Future work	108
7.1 Conclusion	108
7.2 Future work	109
REFERENCES	111
APPENDIX	118

NOMENCLATURE

Latin letter symbols

A	Area	m^2
A_S	Surface area of the free bed surface	m^2
c_p	Heat capacity	J/kg/K
D_h	Hydraulic diameter	m
D	Diameter of the kiln/drum	m
d_p	Particle diameter	mm
E	Specific energy	J/kg
F	Filling degree	%
Fr	Froude number	-
g	Gravitational acceleration	m/s^2
\dot{H}	Enthalpy	W
h_u	Calorific value	J/kg
$\Delta h_{R,S}$	Molar reaction enthalpy	J/mol
h	Bed height	m
L	Length	m
l	Circumference/ perimeter	m
m	Mass	kg
\dot{M}	Mass flow rate of the solid	kg/h
MRT	Mean Residence Time	min
\tilde{M}	Molar mass	kg/kmol
n	Rotational speed	-
Nu	Nusselt number	-
p	Pressure	Pa
p_{eq}	Equilibrium pressure	Pa
p_{max}	Pre-exponential coefficient	Pa
Pr	Prandtl number	-
\dot{Q}	Heat flow	W
\tilde{R}	Universal gas constant	J/kmol/K
R	Radius	m
Re	Reynolds number	-
T_a	Surrounding temperature	$^{\circ}C;K$
T	Temperature	$^{\circ}C;K$

t	Time	s
v	Velocity	m/s
\dot{V}	Volumetric flow rate	m ³ /h
x	Concentration (Based on mass)	kg _i /kg
z	Location axial position of the kiln	m

Greek letter symbols

σ	Stefan-Boltzmann constant	W/m ² /K ⁴
α	Heat transfer coefficient	W/m ² /K
θ	Dynamic angle of repose	rad
ω	Angular rotation speed	rad/s
γ	Filing angle	rad
ε	Emissivity	-
λ	Thermal conductivity	W/m/K
λ	Excess air number	-
ρ	Density	kg/m ³
ν	Kinematic viscosity of the fluid	m ² /s

Subscript or superscript

0	Inlet of a rotary kiln z = 0
α	Convection
ε	Radiation
λ	Contact
∞	Infinite
conv	Convection
eff	Effective
G	Gas
G,m	Gas, mean
GS	Gas to solid
GS,eff	Gas – Solid effective(convection + radiation)
GS, α	Gas – Solid convection
GS, ε	Gas – Solid radiation
GW	Gas to wall

GW,eff	Gas – Inner wall effective(convection + radiation)
GW, α	Gas – Inner wall convection
GW, ε	Gas – Inner wall radiation
WS	Wall to solid
ls	limestone
L	Outlet of a rotary kiln $z = L$
Loss	Loss
m	Mean
max	Maximum
P	Particle
R	Regenerative
rad	Radiation
S	Solid
Shell	Outer kiln shell
W	Kiln wall

Abbreviations

ODE	Ordinary order differential equations
CIS	Commonwealth of independent states
GDP	Gross domestic product

1 Introduction

1.1 Rotary kilns and its application

A rotary kiln is being used extensively in chemical, mineral and metallurgical industries. Fundamentally, rotary kilns are heat exchangers where granular materials are thermally treated. With typical sequences of operation like are drying, heating and chemical reactions that cover a broad range of temperatures. The rotary kiln is a horizontal circular cylinder, supported by support stations and driven via a girth gear and drive train. An industrial rotary kiln can be 230 m long and can have up to 7m of internal diameter [Wocadlo (1994)]. It is inclined at some angle (1° - 4°) to the horizontal and rotates at low revolutions (1-5) rpm around its longitudinal axis. This inclination forces the material to transport in axial direction. The rotary kiln is normally lined with refractory material of different quality depending upon the different temperature zones in the kiln. A rotary kiln with its typical components is shown in figure 1-1 schematically.

The material enters the kiln at the higher end while fuel and air is blown into the rotary kiln at the opposite lower end. Thus the raw material and combustion gases flow countercurrent to each other. On entering the kiln material is preheated or dried and preheated depending on the condition (dry or wet) of the raw material. The preheated material is then burnt at a higher temperature in the flame region. The material undergoes the physical and chemical changes in this zone to yield the product. After reaching the maximum temperature in the region of the flame end, the material temperature decreases.

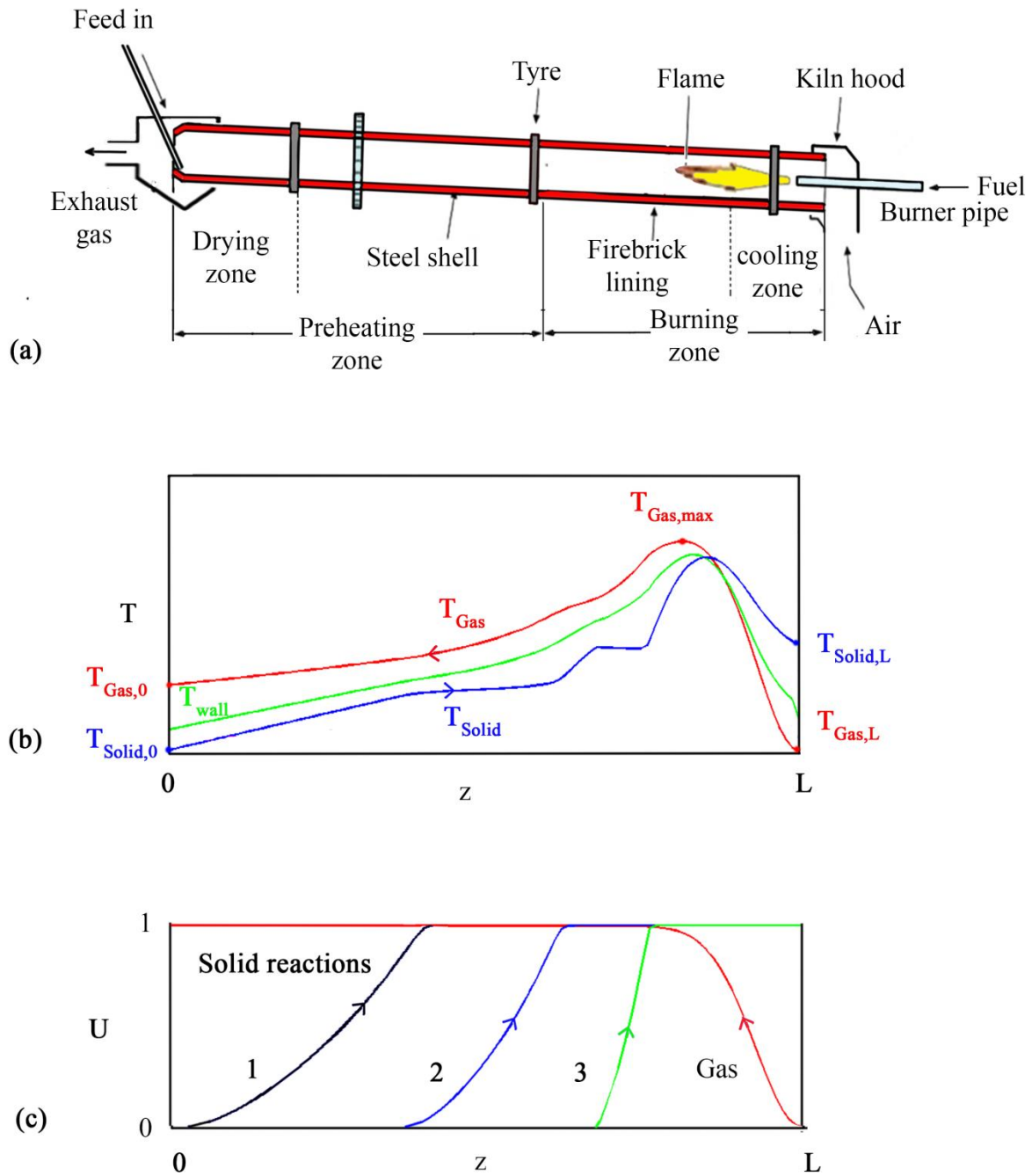


Figure 1-1 a) General layout of a direct fired, counter-current rotary kiln b) axial profile of temperature c) axial profile of conversion degree

The qualitative axial temperature profile of the gas phase, the bulk bed and the interior and outer wall surface of a directly heated rotary kiln in counter flow operation are shown in Figure 1-1(b) at the inlet opening of the rotary kiln at $z = 0$, the bulk material is fed in the kiln at a given temperature ($T_{\text{Solid},0}$), which usually corresponds to the ambient temperature. The fuel and air with a temperature ($T_{\text{Gas},L}$), are blown from the opposite side at $z = L$. The heat generated by burning the fuel with air in the flame increases the gas temperature which reaches its maximum ($T_{\text{Gas},\text{max}}$) in the region where flame ends. After the gas has reached its maximum the temperature decreases to the exhaust gas temperature ($T_{\text{Gas},0}$) due to heat transfer to the wall and the bulk bed. Heat is transferred from gas to solid only when the temperature of the gas is higher than the bulk bed. Otherwise, the bulk heats the gas and is cooled thereby to the product temperature ($T_{\text{Solid},L}$). Consequently, the maximum temperature of the bed is always found slightly before the outlet of the rotary kiln.

The material undergoes chemical or physical reaction at a certain process temperature. The temperature of the solid increases axially as it flows. For each of these reactions, a conversion degree can be defined as the percentage of reactants converted to products inside a chemical reactor and is represented by U . Its value varies from $U = 0$ for no reaction to $U = 1$ for complete reaction. The conversion degree equals to zero ($U = 0$) before material reaches this reaction temperature and beyond this temperature chemical reaction proceeds and consequently temperature and mass changes until the end of the reaction at $U = 1$. Conversion degree of material within the kiln varies from $U = 0$ to $U = 1$. The conversion degree of fuel increases from $U = 0$ before combustion to $U = 1$ at a point where flame ends (L_{flame}) corresponding to the maximum temperature of the gas ($T_{\text{Gas},\text{max}}$). The axial profile of conversion degree of material and fuel are shown in Figure 1-1 (c). Over the decades, constructive and process-technical developments have been implemented in a rotary kiln so that now a large number of processes can be carried out in a rotary kiln. An overview of some thermal processes with the corresponding bulk material temperatures is given in table 1-1.

Table 1-1: Application of rotary kiln processes

Processes	Example	Temperature
Warming	Chippings (for asphalt)	150-200°C
Granulation	Fertilizer, Expanded clay	
Drying	Botanicals (grain, forage, etc.)	60-300°C
	Mineral materials (sand, slag, etc.)	100-300°C
	Slurry (coal slurry)	To 1000°C
	Salts, Coke	
Pyrolysis	Botanicals (e.g. wood chips, biomass)	200-600°C
	Waste (e.g. textiles, plastics)	200-600°C
	Polymers (PAN, phenol, formaldehyde resins)	900-950°C
	Activated carbon	To 1100°C
Gasification	Organic components in soils	600-900°C
	Waste	400 – 900°C
Dehydration	Gypsum	300-700°C
	Salts	
Reduction	Ores (e.g. nickel ore)	600-1200°C
	Strontium sulfate	1100-1200°C
	Barium sulfate	600-800°C
	Tungsten oxide	1200-1300°C
Roasting	Ores	To 1300°C
	Tungsten carbide	750-850°C
	Mercury	700-800°C
Calcination	Aluminium oxide	1000-1600°C
	Lime	1200-1300°C
	Dolomite	1200-1700°C
	Magnesite (Causter)	600-800°C
	Manganese carbonate	650-700°C
	Soda	To 950°C
	Quartz sand	1200-1600°C
	Kaolin	1000-1200°C
	Zirconium dioxide	To 1200°C
	Petroleum coke	1200-1400°C
	Titanium dioxide	800-1000°C
Hard ferrite	1100-1300°C	
Sintering	Cement	1450-1500°C
	Fireclay	1200-1600°C
	Magnesite (sinter)	1800-2200°C
	Ferrite	1050-1300°C
	Polymer	To 150°C
Annealing	Pigments	1200-1300°C
	Expanded clay	800-1200°C
	Granite gravel (color setting)	700-900°C
Smelting	Metal scrap (e.g. lead alloys)	To 1000°C
Combustion	Hazardous waste, commercial waste	1100-1200°C

1.2 Problem statement

There has been ever higher demands on the quality of products manufactured in a rotary kiln which in turn requires the optimization of the processes being carried out in rotary kiln. The optimization or dimensioning of rotary kilns involves higher investment and operating costs. The processes in rotary kilns are energy intensive owing to higher temperatures. Thus, to design a rotary kiln or to optimize the process by taking into account the economic factors, the underlying process must be first understood precisely in particular the knowledge of the process behavior with variation in influential variables is indispensable. Table 1-2 lists most important parameters which may affect the process inside a rotary kiln.

Table 1-2: Variable parameters in the rotary kiln process

Category	Variable parameter
Dimensioning	Kiln diameter
	Kiln length
	Kiln Inclination
Operational	Product mass flow
	Kiln rotational speed
	Gas throughput
Heating	Fuel type
	Flame length
	Flame shape
	Heat distribution
Bulk	Particle size
	Particle size distribution
	Particle shape/flowability
	Angle of repose
	Density
	Specific heat capacity
	Thermal conductivity
	Reaction behavior

Since the interaction between these parameters is largely unknown, empirical relations are most commonly used in designing a kiln or optimizing the process. Thus, in practice, a kiln is designed and operated at higher values of dimensional and operating parameters than theoretically necessary to ensure the required product quality. This results in higher

investment and operating costs. Also, the operator lacks the knowledge about the process behavior. Hence, sets of parameters which may give the desired product quality with relatively lower operating cost cannot be defined. Moreover, measurements for example heat transfer in industrial rotary kilns are not possible. If a process parameter at large-sized installations is varied, a steady state is reached after a few days or weeks, due to the long response time behavior of the kiln. Thus, a study to determine the parameters for a real industrial kiln would lead to an enormous loss of production. A rotary kiln must be designed by taking into account four aspects of engineering and technical standpoint. These are the heat transfer, the material motion through the rotary kiln, the mass transfer between gas and solid phases, and the chemical reaction which in turn require the knowledge of temperature profiles of gas, bulk bed, at inner surface of the refractory wall, and outer shell etc. It is difficult to measure these profiles by installing thermal sensor due to the high temperature and the abrasion within the bulk bed. Also, optical sensor can't be installed because of the high quantity of the dust.

Mathematical modelling can be employed therefore for designing a rotary kiln in order to optimize their performance. It can potentially decrease both investment and operating costs. Recently, Herz (2012) has developed a mathematical process model by discretizing the kiln into infinitesimally small volume elements and then by solving the set of differential equations for these elements. This model has coupled the phenomenon of heat transport, motion behavior of solids, and bulk bed transport. It gives output data on the temperature profiles of gas, bulk bed, at inner surface of the refractory wall, and outer surface of the shell. It also defines the heat losses through the wall, composition of exhaust gases, and outlet temperature of gas and solid.

The objective of the present work is to improve the above mentioned model by taking into consideration the heat of reaction additionally. It is crucial to formulate an improved version of this model which could be capable of explaining the wide range of applications in industry as listed in table 1-1. Keeping in view the difficulties associated with measurements of the important parameters, mathematical modelling is employed in this

study. The improved model will be validated for different material in this work whereas materials have been selected according to their industrial importance. Three different types of validation are used: First, validation with the data obtained through experiments at technical scale laboratory rotary kiln. Second, validation with operational data provided by the industry. Third, validation with data reported in previous literature.

1.3 Thesis Outline

This thesis is arranged as follows:

Chapter 1 provides a general description of an industrial rotary kiln and an overview of various industrial applications of this kiln. It also discusses the problem statement and the goal of this research.

Chapter 2 describes the process of heat and mass transfer inside the rotary kiln. This chapter also describes the model which could explain the coupled phenomenon of heat transfer and motion behavior of solids and bulk bed transport inside the rotary kiln.

Chapter 3 gives the details of the process of producing the selected materials in industry. The modification of the process model, discussed in chapter 2 for each material, is presented here. These modified models are obtained by considering the heat of reactions.

Chapter 4 presents the experimental setup of the technical scale rotary kiln. The experimental results for the selected materials like aluminum dross and siderite are discussed here. This chapter also demonstrates the comparison between and the experimental results and simulations.

Chapter 5 enlists the process data of industrial rotary kilns from literature. The simulation results for the selected materials such as magnesite, dolomite, and gypsum and titanium oxide are also presented in this chapter. The simulation results are validated in this chapter.

Chapter 6 presents the operational data for the industrial scale rotary kiln. It also discusses the simulation results for materials like cement, limestone and kaolin by taking this data in consideration. The simulation results are also validated with industrial data in this chapter.

Chapter 7 concludes this research, summarizes the key findings of this work and gives the recommendations for the future work.

2 Mathematical process model

2.1 Heat transfer

The mechanism of heat transfer in direct heated rotary kilns is shown in figure 2-1

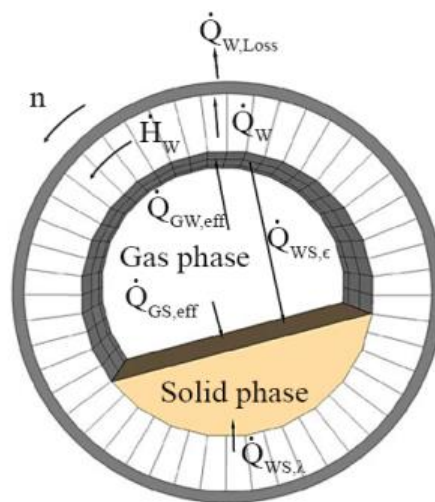


Figure 2-1: Heat transfer in direct heated rotary kilns [Nafsun (2016)].

The Flame and combustion gases act as a source of heat which transfers heat to both the solid bed and free wall through radiation and convection. Heat flows from gas to solid and also from freeboard gases to the free wall surface through combination of convection and radiation. These heat flows through superimposing of convection and radiations are defined as the effective heat flows and are represented by $\dot{Q}_{GS, eff}$, $\dot{Q}_{GW, eff}$ respectively. A part of the heat transferred to the wall is absorbed by the wall, while the other is reflected from the wall back to surface of the solid bed surface, $\dot{Q}_{WS, \epsilon}$. A part of the absorbed heat is conducted through the wall, \dot{Q}_W and is lost to the environment, $\dot{Q}_{W, Loss}$ through radiation and convection between outer shell and ambient. The other part of heat absorbed by the

wall, \dot{H}_w and transported with the rotation of the wall to the contact region between the inner wall and the solid bed, and serve as regenerative heat transfer, \dot{Q}_R where the heat is then conducted from the covered wall surface to the covered solid bed, $\dot{Q}_{ws,\lambda}$. The above explained heat flows are calculated by using equations 2-1 to 2-3

$$\dot{Q}_{GS,eff} = \dot{Q}_{GS,\alpha} + \dot{Q}_{GS,\varepsilon}, \quad (2-1)$$

$$\dot{Q}_{GW,eff} = \dot{Q}_{GW,\alpha} + \dot{Q}_{GW,\varepsilon}, \quad (2-2)$$

$$\dot{Q}_{W,shell} = \dot{Q}_{shell,\alpha} + \dot{Q}_{shell,\varepsilon}, \quad (2-3)$$

where $\dot{Q}_{GS,\alpha}$ and $\dot{Q}_{GS,\varepsilon}$ are the convection and radiation heat transfer between gas and solid respectively. $\dot{Q}_{GW,\alpha}$ and $\dot{Q}_{GW,\varepsilon}$ are convection and radiation heat transfer between gas and wall. $\dot{Q}_{shell,\alpha}$ and $\dot{Q}_{shell,\varepsilon}$ are the convection and radiation heat transfer between shell and ambient

The heat transfer mechanisms depend on the contact areas between gas and wall, wall and solid, and gas and solid respectively. Which are shown in figure 2-2

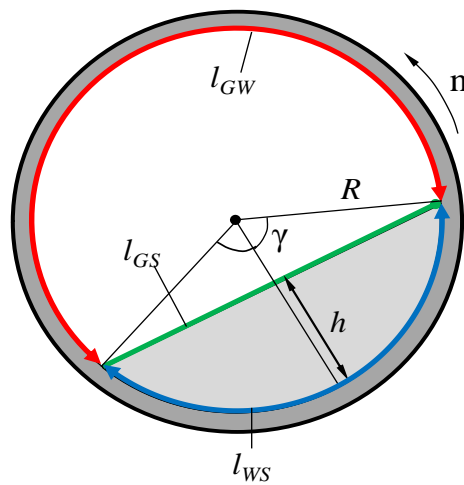


Figure 2-2: Geometrical representation of the contact surfaces in rotary kilns [Nafsun (2016)].

The heat transfer areas are defined by the circumference, l , the inner kiln radius, R , the half angle occupied by the solid bed i.e. filling angle, γ , and the cylinder length, L . The bed height, h decreases in axial direction as the material flows through the kiln from upper to lower end. As the bed height decreases, the local heat transfer area varies, which affects the corresponding heat transfer. The circumference is divided into three lengths which are listed below:

1) l_{GW} is the exposed wall circumference where convective and radiative heat transfer take place in the freeboard region. The resulting heat transfer area A_{GW} is

$$A_{GW} = l_{GW} \cdot L = 2 \cdot R \cdot (\pi - \gamma) \cdot L. \quad (2-4)$$

2) l_{WS} is the covered wall circumference where contact heat transfer takes place between the covered wall and the covered bed. The contact heat transfer is

$$A_{WS} = l_{WS} \cdot L = 2 \cdot R \cdot \gamma \cdot L. \quad (2-5)$$

3) l_{GS} is the chord length of the free solid surface which is responsible for the convective and radiative heat transfer between the freeboard gas and the exposed solid surface. The area of the exposed bed surface, A_{GS} is

$$A_{GS} = l_{GS} \cdot L = 2 \cdot R \cdot \sin\gamma \cdot L. \quad (2-6)$$

The convection part of heat transfer mentioned in equations 2-1 to 2-3 can be calculated by using models. Following equations can give these heat transfer rates.

$$\dot{Q}_{GS,\alpha} = \alpha_{GS,conv} \cdot A_{GS} \cdot (T_G - T_S) \quad \text{with} \quad \alpha_{GS,conv} = \frac{Nu \cdot \lambda_G}{D_h}, \quad (2-7)$$

$$\dot{Q}_{GW,\alpha} = \alpha_{GW,conv} \cdot A_{GW} \cdot (T_G - T_W) \quad \text{with} \quad \alpha_{GW,conv} = \frac{Nu \cdot \lambda_G}{D_h}, \quad (2-8)$$

$$\dot{Q}_{shell,\alpha} = \alpha_{shell,conv} \cdot A_{shell} \cdot (T_{shell} - T_W) \quad \text{with} \quad \alpha_{shell,conv} = \frac{Nu \cdot \lambda_G}{D_h}, \quad (2-9)$$

where λ_G is thermal conductivity of gas, D_h is the hydraulic diameter and Nu is the nusselt number.

For rotary kiln application, the heat transfer by convection occurs due to forced convection it can be represented with nusselt number, which is the ratio between convection heat flows to conductive heat flow of fluid .The nusselt number can be calculated by an equation given by Gnielinski (1995):

$$Nu_{z,standard} = 0.0214 \cdot (Re_G^{0.8} - 100) \cdot Pr_G^{0.4} \cdot \left[1 + \frac{1}{3} \cdot \left(\frac{D_h}{z} \right)^{\frac{2}{3}} \right], \quad (2-10)$$

$$\text{With } Re_G = \frac{v_G \cdot D_h}{\nu_{G,m}} \quad \text{and} \quad v_G = \frac{\dot{V}_G}{A_G}, \quad (2-11)$$

where Re is Reynolds number, Pr is Prandtl number, v_G is the fluid velocity, D_h is the characteristic length of the system, ν is the kinematic viscosity and z is the local axial position of the kiln.

The recirculation affects the local convective heat transfer strongly due to the increased turbulence Woche et al. (2005 and 2007) measured the local nusselt number with varying ratios of diameter of burner to the diameter of kiln and found the local nusselt number to be factor of 6 to 7 greater than the average value of local nusselt number given by equation 2-10. Woche et al. (2005 and 2007) gave the following correlations for the local nusselt number in the axial direction in relation to the ratio of axial position to the diameter of the kiln ($\frac{z}{D_h}$) as

$$\frac{Nu_{G,z}}{Nu_{G,\infty}} = 1.71 \cdot \frac{z}{D_h} + 1.37 \quad \text{for } (0 \leq \frac{z}{D_h} \leq 3), \quad (2-12)$$

$$\frac{Nu_{G,z}}{Nu_{G,\infty}} = 1 + \left(\frac{Nu_{G,max}}{Nu_{G,\infty}} - 1 \right) \exp \left[0.3 \cdot \left(\frac{z_{max} - z}{D_h} \right) \right] \quad \text{for } (3 \leq \frac{z}{D_h} \leq \frac{L}{D_h}), \quad (2-13)$$

The maximum value of nusselt number exists when this ratio is approximately equals 3

$$\frac{Nu_{z,\max}}{Nu_{G,\infty}} = 6.5 \quad \text{for} \quad \left(\frac{z_{\max}}{D_h} \approx 3\right), \quad (2-14)$$

where $Nu_{G,z}$ is the local nusselt number at any position (z), $Nu_{G,\infty}$ is the value of nusselt number at $z/L=27$ and holds

$$Nu_{G,\infty} = Nu_{G,\text{standard}} \cdot \quad (2-15)$$

The radiation part of heat transfer mentioned in equations 2-1 to 2-3 are defined by

$$\dot{Q}_{GS,\varepsilon} = \varepsilon_{GS} \cdot \sigma \cdot A_{GS} \cdot (T_G^4 - T_S^4), \quad (2-16)$$

$$\dot{Q}_{GW,\varepsilon} = \varepsilon_{GW} \cdot \sigma \cdot A_{GW} \cdot (T_G^4 - T_W^4), \quad (2-17)$$

$$\dot{Q}_{shell,\varepsilon} = \varepsilon_{shell} \cdot \sigma \cdot A_{shell} \cdot (T_{shell}^4 - T_S^4), \quad (2-18)$$

where ε_{GS} , ε_{GW} and ε_{shell} are the effective emissivity between the gas and the solid, gas and wall, shell and ambient respectively. These effective emissivities can be calculated by models of Schupe (1974), Jeschar et al. (2004).

Regenerative heat flows from the covered wall to the covered bed can be determined by using the model of Agustini et al. (2008).

$$\dot{Q}_R = \alpha_R \cdot A_{WS} \cdot (T_W - T_S), \quad (2-19)$$

$$\alpha_R = \frac{1}{\left(\frac{1}{\alpha_{WS,\lambda}}\right) + \left(\frac{1}{\alpha_{GW}} \cdot \frac{\gamma}{\pi - \gamma}\right) + \left(\frac{1}{\alpha_T} \cdot \frac{\gamma}{\pi}\right)}, \quad (2-20)$$

where α_T is the heat transportation coefficient, $\alpha_{WS,\lambda}$ is the contact heat transfer coefficient, α_{GW} is the heat transfer coefficient between gas and the wall.

A more detailed description can be found in Herz, (2012).

2.2 Solid transport in rotary kilns

2.2.1 Axial transport and residence time

The bulk material is fed into the rotary kiln at a defined rate. The solids inside the rotary kiln adjust the certain profile of axial solid bed height along the length of the rotary kiln under the effect of difference of height between the inlet and outlet opening of rotary kiln, the rotation and inclination of the rotary kiln as shown in the figure 2-3.

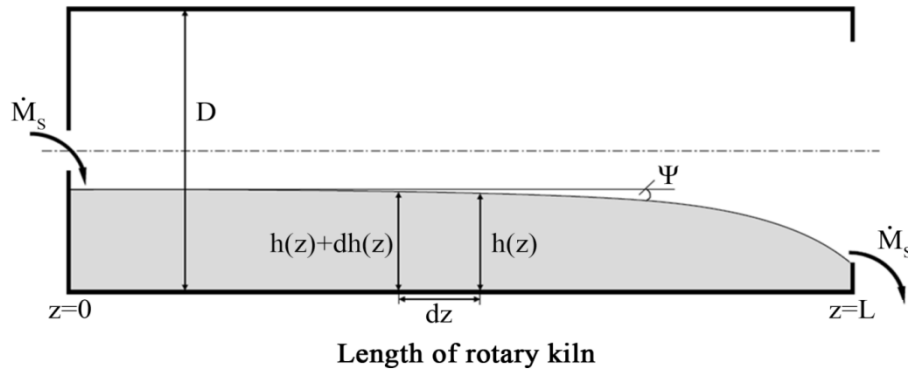


Figure 2-3: Axial bed height profile.

The profile of filling degree can serve the determination of the mean residence time of the solid material as well as the determination of the heat transfer surfaces at each axial position of the rotary kiln.

A mathematical model which illustrates the axial transport inside the kiln was first derived by Saeman (1951).

$$\frac{dh}{dz} = \tan \psi = \frac{3 \cdot \tan \Theta}{4 \cdot \pi \cdot n} \cdot \frac{\dot{M}_s}{\rho_s} \left[R^2 - (h - R)^2 \right]^{\frac{3}{2}} + \frac{dR}{dz} - \frac{\tan \beta}{\cos \Theta}, \quad (2-21)$$

where \dot{M}_s is the mass flow rate of solids in kg/s, ρ_s is the density of the solid in kg/m³, R is the radius of the kiln in m, β is the inclination angle in rad, Θ is the dynamic angle of repose in rad and n is the rotational speed in rpm.

The mean residence time is defined as the average time spent by the bulk material inside the kiln beginning from material entry to the kiln until the out let leaves the kiln. Numerous equations have been proposed to predict the residence time [Sai et al. (1992)]. In most of these studies, only average hold-up, M and mass feed-rate, \dot{M}_s were considered in prediction of the residence time.

The Mean Residence Time, MRT is defined as below,

$$MRT = \frac{M}{\dot{M}_s}, \tag{2-22}$$

The depth profile $h(x)$ of the solids and thus the kiln hold-up, M kg can be calculated as:

$$M = \rho_s \cdot R^2 \cdot \int_0^L (\gamma - \sin \gamma \cdot \cos \gamma) dz, \tag{2-23}$$

γ is the local filling degree in rad, ρ_s is the density of the solid in kg/m^3 , R is the radius of the kiln in m.

2.2.2 Transverse motion of particles

Mellmann (2001) described different modes of transverse motion in a rotating cylinder as described in (Table 2-1):


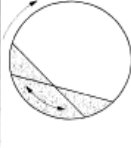


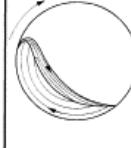
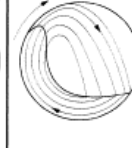
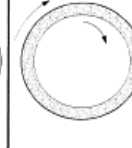
Basic form	Slipping motion		Cascading ("tumbling") motion			Cataracting motion	
	Sliding	Surging	Slumping	Rolling	Cascading	Cataracting	Centrifuging
Schematic							
Physical process	Slipping		Mixing			Crushing	Centrifuging
Froude number Fr [-]	$0 < Fr < 10^{-4}$		$10^{-5} < Fr < 10^{-3}$	$10^{-4} < Fr < 10^{-2}$	$10^{-3} < Fr < 10^{-1}$	$0.1 < Fr < 1$	$Fr \geq 1$
Application	no use		Rotary kilns and reactors; rotary dryers and coolers; mixing drums			Ball mills	no use

Table 2-1: Characteristics of different types of transverse motion [Mellmann, 2001]

- Sliding is seen when frictional forces are too small (smooth cylinder) to hold the particles to remain in contact with the cylinder wall. In this motion the bed of particles remain at the same place as the wall of rotary kiln rotates under the bed.
- Surging is noticed when whole solid body slides back when it is brought at a higher position due to the rotation of the kiln. Sliding motion is transitioned to surging motion with increase in the filling degree and the rotation speed.
- Slumping takes place when a segment of bulk material at the shear wedge becomes unstable and empties down the incline.
- Rolling occurs when particles flow continuously with a constant slope along the surface.
- Cascading occurs at relatively high rate of rotation in which the particles cascade or shower down the free surface.
- Cataracting motion behavior is presented by the particles in cascading motion when the filling degree and rotation of kiln is further increased. The particles leave the contact with the wall and are thrown out in the free space inside the kiln.
- Centrifuging occurs at critical and high speeds in which the bed material attaches to the wall of the kiln and rotates with the rotating drum wall.

Transverse solid motion is influenced by kiln parameters and properties of the bulk. As could be seen in Table 2-1 Different major regimes of the motion behavior of the solid material inside the kiln can be identified on the basis of the Froude number and the filling degree. Froude number is the ratio between centrifugal forces and gravitational forces.

$$Fr = \frac{\omega^2 \cdot R}{g} \quad \text{with} \quad \omega = \frac{2 \cdot \pi \cdot n}{60}, \quad (2-24)$$

where n is the rotational speed in rpm, R is the inner kiln radius in m and g is the gravitational force in m/s^2 .

The filling degree F is defined as the ratio of the cross sectional area of the solid bed, $A_{\text{solid bed}}$ to the total cross sectional area of the drum, A_{drum} .

$$F = \frac{A_{Solidbed}}{A_{drum}} = \frac{\gamma - \sin \gamma \cos \gamma}{\pi} \quad \text{with} \quad \gamma = \arccos\left(1 - \frac{h}{R}\right), \quad (2-25)$$

where γ the filling angle in rad, R is is the kiln radius in m and h is the height of the solid bed in m.

Rolling motion is preferred in comparison to the all motion types listed in table 2-1 in industrial applications as it ensures the better mixing of solid particles in the bed. It is characterized as a continuous flow of particles at the surface with nearly constant slope as shown in the figure 2-4. This slope is defined as the dynamic angle of repose Θ which depends on material properties of solid bed and wall friction.

The solid bed undergoing rolling motion can be divided into two layers namely active layer and passive layer as shown in figure 2-4. Active layer is also called the mixing zones as mixing of the particles in the bed takes place in this zone while the passive layer is termed as the stagnant zone. The dotted line ACB represents the boundary between these layers. The continuous circulation of the particles in active layer during the rolling motion promotes good mixing and results in uniform temperature distribution inside the bed.

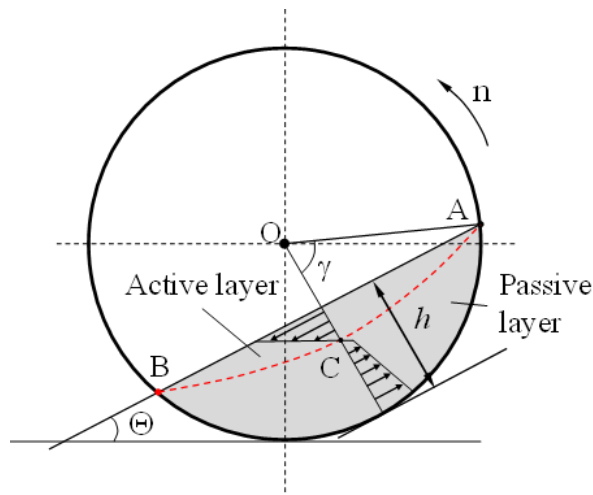


Figure 2-4: Geometrical characteristics of rolling [Herz, 2012].

2.3 Process Model description

Several mathematical models have been developed to describe processes in rotary kilns. Imber and Paschkis (1962) studied the length of the kiln required to achieve a certain temperature under two limiting cases i.e 'well-mixed' and 'not mixed' for the bed. The maximum length is required in a non-mixed condition while well-mixed condition corresponds to minimum length of the kiln. The actual length is an average of both these values of length. They have discussed the methods to calculate these values of the length. They have used the Gilberts work to compute the values modified heat transfer coefficients [Imber and Paschkis (1962)]. It is also shown that the condition of well-mixed yields better fitting results with the reported results than obtained in case of non-mixed condition. Their model does not consider the material transport and reaction mechanism in solid and gas bed. Saas et al. (1967) developed a model in order to predict the rate of heat transfer inside the rotary kiln. They studied a kiln charged with wet solids. They obtained differential equations by employing the assumption that at any given cross section of the kiln the temperatures of gas, solid, inner and outer wall of kiln are independent of radial location. These equations were solved using Runge Kutta method. The model was validated with the actual operating data from the cement kiln and the iron ore kiln. Their results were very close to reality and also far superior in comparison to the results of already available correlations Perry (1950, 1963). However, the influence of chemical reaction was not considered by the researchers.

A dynamic model for temperature profile in cement kiln was formulated by Spang (1972). They took into account the surrounding temperature while modelling the coal/oil flame. The mass and velocity of gas and solid are assumed to be constant along the length of the kiln. The rates of chemical reactions are calculated using Arrhenius law. The results were reported in terms of axial profile for gas, solid bed, inner and outer wall and the composition of the bed. Though this model is very successful in explaining the kiln behavior qualitatively especially in burning zone, its quantitative validation could not be performed due to the lack of experimental data.

Pearce (1973) developed a model to describe the temperature profile and the heat transfer coefficients for the gas and the solid for the dolomite and the magnesite kilns. The analytical equations were developed and were iteratively solved. The heat lost through the wall of the kiln was not considered. The models were validated by the data from the industrial dolomite and magnesite kilns.

Manitus et al. (1974) formulated a stationary mathematical model for the production of the aluminum oxide. The mass and energy balanced were written by considering the reaction inside the bed and the heat transfer between each phase. The equations obtained were solved by using Euler method. The model was validated with the data from two industrial kilns.

The rotary kiln used for production of titanium oxide was modelled by Belanger (1978). The mass and energy balance equations were written and were solved as boundary value problem using Newton-Raphson method. The model predicted the temperature profiles of gas, solid, and wall. The results of the model were validated with the data from two industrial scale rotary kilns.

A quasi-3D model was developed by Boateng and Barr (1996) by coupling of 1D axial model with the 2D cross sectional model in order to calculate the temperature distribution inside the bed and at the refractory wall. The transport phenomenon inside the bed and the freeboard gas was considered. The bed- wall equations were solved for the cross section using finite volume method.

A comprehensive model for the rotary cement kiln was presented by Mastorakos et al. (1999) which could calculate the energy transferred from flame to the clinker and heat loss from the kiln. Three separate models were coupled namely CFD axisymmetric code for gas alongwith Monte- Carlo method for radiation, finite volume method for the temperature of the kiln wall and energy and species conservation considering chemical reactions for the formation of clinkers. The heat transfer coefficients on the contact between wall and solid as well as between shell and surrounding were assumed to be constant. They showed that the 40 % of heat supplied drive the chemical reactions which

lead to the clinker formation and 10% of heat is lost to the ambient. The predictions of this model were found to agree with the measurements at full scale cement rotary kiln.

Georgallis et al. (2005) developed a 3D steady state model for production of lime in rotary kiln in order to predict the heat transfer and flow inside the kiln. The model is obtained through coupling of three sub-models. These models are, Hot wire model for modelling the combustion of the fuel through finite volume method, Bed model using the finite element method to solve the 3D energy and species transport equations, and The Wall/refractories model to predict the heat losses from the kiln. This model was validated with the trials at the kiln at University of British Columbia.

The above explained models explain a number of processes in rotary kiln but none of them could couple the heat transfer mechanism, chemical reaction kinetics and the transport of solid bed in axial and transverse directions. Some models assumed the constant heat transfer coefficients along the kiln length. As the heat transfer phenomenon depends both on location and temperature so this assumption is an adequate criterion.

Another models neglect the transport axial and transverse of the bed. However, the bed height changes in the in axial direction which causes the heat transfer surface of kiln wall and the bed to change significantly. Thus, the axial transport of the bed cannot be neglected. Some models are designed for the specific process in the specific equipment so their applicability for other processes cannot be insured.

Consequently there was a need of the model which could be used for various processes and could describe the phenomenon of heat transfer and solid transport and their interaction with each other during the thermal process inside the rotary kiln.

A mathematical process model was developed by Herz (2012) seems to tackle these issues very well. It describes the coupled phenomenon of heat transfer, motion behavior and solid transport. This model however neglects the heat of reactions. This model will be modified by additionally considering the heat of reaction and is explained in detail as follows:

The kiln has been discretized into infinitesimally small volume elements and then the set of differential equations for these elements were solved. Figure 2-5 shows a volume element schematically. This model gives output data on the temperature profiles of gas, bulk bed, at inner surface of the refractory wall, and outer surface of the shell. This model has been validated with the data from lab scale and industrial scale and its prediction have shown a good agreement with the data.

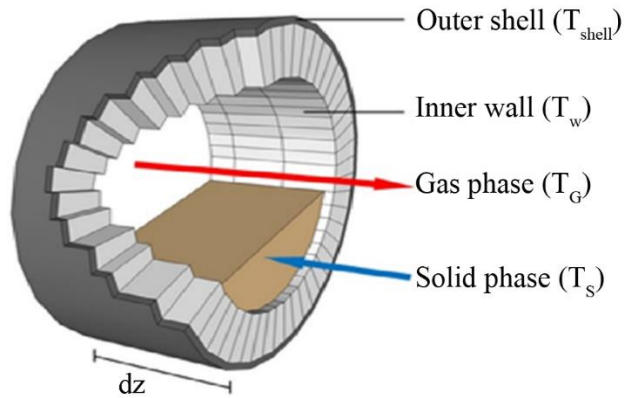


Figure 2-5: Schematic diagram of the defined phases in the process model [Herz, 2012].

The rotary kiln is discretized into infinitesimally small length elements dz in the axial direction. Heat is exchanged among gas phase, solid phase and wall within these elements over the cross-section of the rotary kiln as described in section 2.1. The conservation laws are set up to describe the change in the temperatures over these length elements dz . For the gas phase applies

$$d\dot{H}_G = dR_{Fuel} + d\dot{Q}_{GS,eff}(h, T_G, T_S) + d\dot{Q}_{GW,eff}(h, T_G, T_W). \quad (2-26)$$

The change of the enthalpy of the gas phase, \dot{H}_G is equal to the heat flow generated by conversion of the fuel, R_{Fuel} plus transferred heat from gas to solid $\dot{Q}_{GS,eff}$ and gas to wall $\dot{Q}_{GW,eff}$. the enthalpy term can be defined by change in the temperature of the gas and the change of capacity flow rate over the length by using equation (2-27):

$$\frac{d\dot{H}_G}{dz} = \frac{d\left[\dot{M}_G(z) \cdot c_{P,G}(T_G) \cdot T_G\right]}{dz} = \dot{M}_G(z) \cdot c_{P,G}(T_G) \cdot \frac{dT_G}{dz} + c_{P,G}(T_G) \cdot T_G \cdot \frac{d\dot{M}_G(z)}{dz}. \quad (2-27)$$

The mass flow of the combustion gas \dot{M}_G is

$$\dot{M}_G(z) = \dot{M}_{Fuel} \cdot (1 + \lambda \cdot L_d) + \dot{M}_{S,diss}(z), \quad (2-28)$$

where \dot{M}_{Fuel} is the fuel mass flow, L_d is stoichiometric air demand and λ is excess air number i.e. the ratio of the supplied amount of air to the stoichiometric air requirement.

Mass of combustion gas can vary depending on the nature of dissociating components in the bulk bed phase, $\dot{M}_{S,diss}(z)$ over the kiln length.

With the concentration of the combustion gas components the thermo-physical properties, such as the specific heat capacity can be determined. The specific heat capacity of the combustion gas is calculated by the weighted sum of the heat capacity of individual components. These heat capacities depend on the temperature of the combustion gas as described by Müller (1968).

$$c_{P,i}(T_G) = c_{P,i,n} \left(\frac{T_G}{T_n} \right)^{K_i}, \quad (2-29)$$

$$c_{P,G}(T_G) = \sum x_{g,i} \cdot c_{P,i}(T_G), \quad (2-30)$$

where $x_{g,i}$ and $c_{P,i,n}$ are the concentrations of individual components and the heat capacity respectively.

The local reaction rate of fuel, $\frac{dR_{Fuel}}{dz}$ is the locally released chemical energy which acts as a source term in the energy balance of the gas phase in equation (2-24):

$$\frac{dR_{Fuel}}{dz} = \frac{dU_{Fuel}}{dz} \cdot \dot{M}_{Fuel} \cdot h_{u,Fuel}, \quad (2-31)$$

where \dot{M}_{Fuel} is the fuel mass flow and $h_{u,Fuel}$ is the calorific value of the fuel.

The energy balance for solid can be written as following:

$$d\dot{H}_s = d\dot{Q}_{GS,eff}(h, T_G, T_S) + d\dot{Q}_{WS,\lambda}(h, T_W, T_S) + d\dot{Q}_{WS,\varepsilon}(h, T_W, T_S) \pm \sum dR_{S_i}. \quad (2-32)$$

The change in the solid enthalpy flow, \dot{H}_s is composed of the heat transferred from the gas to the solid $\dot{Q}_{GS,eff}$ and the wall to the solids and the reaction enthalpy, R_s of the solids.

According to equation (2-32), enthalpy of solid change in the axial direction and can be calculated by change in the temperature of the solid and the change of solid flow rate over the length.

$$\frac{d\dot{H}_s}{dz} = \frac{d\left[\dot{M}_s(z) \cdot c_{P,S}(T_S) \cdot T_S\right]}{dz} = \dot{M}_s(z) \cdot c_{P,S}(T_S) \cdot \frac{dT_S}{dz} + c_{P,S}(T_S) \cdot T_S \cdot \frac{d\dot{M}_s(z)}{dz}, \quad (2-33)$$

Along the rotary kiln, the mass flow can change in dependence on the reactions of bulk materials for example mass loss due to conversion reactions taking place in the kiln. These reactions may cause the gas release or absorption which can drastically change the mass flow rate inside the kiln. The mass flow of solids along the length of kiln is

$$\dot{M}_s(z) = \dot{M}_{S,in} - \dot{M}_{S,diss}(z). \quad (2-34)$$

The heat of reaction is represented by the term, dR_{S_i} in equation (2-32). It can have both positive and negative values according to the thermodynamics (exothermic or endothermic) of the reaction and is defined by

$$\frac{dR_{S_i}}{dz} = \sum \frac{dU_{S_i}}{dz} \cdot \dot{M}_S(z) \cdot \Delta h_{u_i} \quad (2-35)$$

where U_{S_i} is the conversion degree, and Δh_{u_i} is the reaction enthalpy of the component.

The reaction term in above equations will be explained in details in chapter 3.

To account for the heat losses through the furnace wall, the surface temperatures of the inner wall and the outer shell are determined iteratively by means of energy balance on a wall element and ultimately coupled to the differential equations of the gas and solid phase. For a wall element it is defined:

$$d\dot{Q}_{GW,eff}(h, T_G, T_W) = d\dot{Q}_{Wa}(h, T_W, T_{Shell}, T_a) + d\dot{Q}_R(h, T_W, T_S) + d\dot{Q}_{WS,\epsilon}(h, T_W, T_S), \quad (2-36)$$

where $\dot{Q}_{GW,eff}$ is the effective heat transfer from the gas to the wall, \dot{Q}_{Wa} is the radiation heat transfer from the wall to the environment, \dot{Q}_R is the regenerative heat flow, $\dot{Q}_{WS,\epsilon}$ is the heat transfer from wall to solid bed. The equations (2-26), (2-32) and (2-36) are coupled with $\frac{dh}{dz}$ and the characteristic parameters listed in the heat flows like height, h of the bulk bed, temperature of the gas, T_G and solid phase, T_S , the surface temperatures of the inner wall, T_W , the temperature of the ambient, T_a and the temperature of the shell wall T_{Shell} .

The overall model consists of mutually coupled, ordinary first order differential equations, which are linked to a set of non-linear algebraic equations for the phenomenological description of heat transfer, fluid flow and bulk material motion and thermodynamic properties. Furthermore, they will be coupled with a set of ordinary differential equations (ODE) which explain the reaction behavior of the bulk material (see eqn 2-35). The system of equations is solved as a boundary value problem for that the values of the temperatures of the feed material ($T_{S,0}$) and the temperature of the gas at burner end ($T_{G,L}$) are available. MATLAB version 2016b is used to solve this problem.

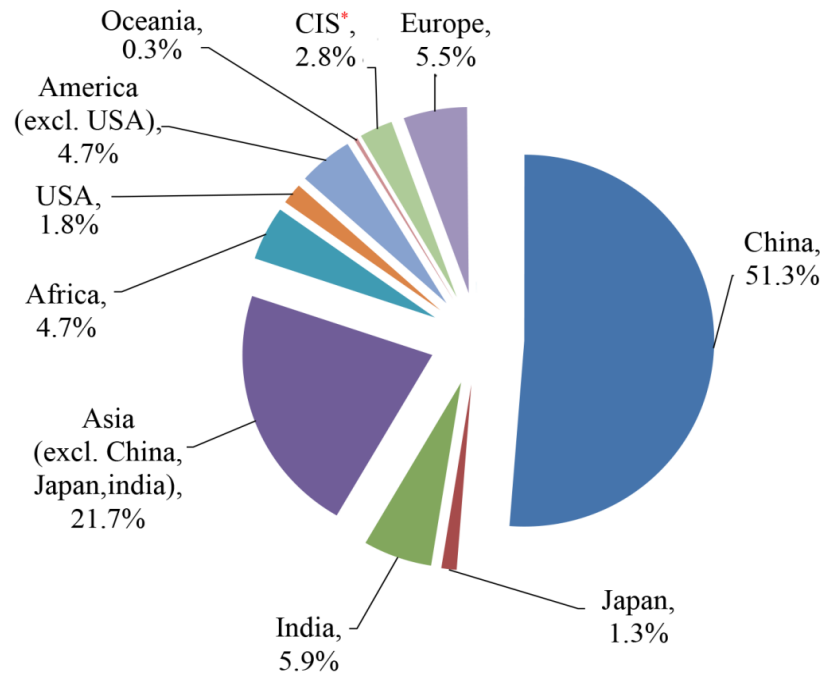
3 Reaction terms within the bulk bed

3.1 Cement

3.1.1 Cement processing

Cement is a water-based binder used to bind building materials like mortar and concrete together. The ability of cement to hold the structure together makes it the most common construction material among others. The demand for cement has increased in the past tremendously resulting in tripling of total global cement capacity in just 23 years i.e. from 1 billion ton (Bnt) in 1986 to 3 Bnt in 2009 [minerals.usgs.gov]. In 2015, a total of 4.6 Bnt of cement was produced worldwide, with 51.3 % in China, 5.5 % in the European Union, 5.9 % in India and 1.8 % in the US (figure 3-1) [cembureau.be].

In 2014, the German cement plants produced around 0.32 Bnt of cement for a turnover of approximately 2.5 billion euros [cembureau.be]. The desire for improved living standards across the globe and ongoing infrastructure development ensures that cement will remain an extremely important commodity for construction. Global cement production and its consumption is forecasted to rise from the estimated 3.3 Bnt in 2010 to almost 5.9 Bnt by 2025 [Global Cement Magazine]. This represents an overall expansion of approximately 78% related to 2010.



*CIS:Commonwealth of Independent States

Figure 3-1: World cement production 2015 (4.6 billion tonnes), by region and countries in % [Global Cement Magazine].

Raw material for cement production

Cement is produced through a closely controlled chemical combination of calcium, silicon, aluminum, iron and other ingredients. The main constituents of the raw materials required for cement production are calcium oxide (CaO), silicon dioxide (SiO₂), aluminum oxide (Al₂O₃) and iron oxide (Fe₂O₃). Typical sources of these oxides are limestone, chalk, marble, clays (kaolinite, illite, feldspar) or shale, tuff, oil shale, bauxite and iron ore [vdz-online.de]. The small amounts of sand and iron can also be added to adjust the composition of the mixture [Perry and Green (1999), Boateng (2008)]. Apart from the main components, these raw materials also contain small quantities of other metals. As an example a typical composition of Portland cement as the most common type of cement is shown in table 3-1.

Table 3-1: Typical constituents of Portland cement

Component	Mass
Calcium oxide, CaO	61–67%
Silicon dioxide, SiO ₂	19–23%
Aluminum oxide, Al ₂ O ₃	2.5–6%
Iron oxide, Fe ₂ O ₃	0–6%

Fuel for cement production

Cement production is an energy intensive process and uses around 3.4-5 MJ/kg_{clinker} of energy for dry process and 5-6 MJ/kg_{clinker} for wet process [Bye (2011)]. The energy used in this process is traditionally obtained by burning fossil fuels like oil, gas and coal. The usage of fossil fuels renders the process to be expensive. Over the years the trend is to replace the fossil fuels with alternate fuels like tyres, waste oil, commercial and residential waste, scrap wood, etc. The energy from waste can be recovered in cement kilns. Also the non-combustible components in the waste such as ash or slag can become the part of cement thereby decreasing the need to dispose these materials.

The proportion of alternative fuels in the total thermal energy consumption in cement industry was around 63 per cent in 2014 in Germany. Table 3-2 lists the most common alternative fuels being used in cement production.

Table 3-2: Alternative fuels for the cement industry

Liquid waste fuels	Tar, chemical wastes, distillation residues, waste solvents, used oils, wax suspensions, petrochemical waste, asphalt slurry, paint waste
Solid waste fuels	Petroleum coke (“petcoke”), paper waste, rubber residues, pulp sludge, used tires, battery cases, plastics residues, wood waste, domestic refuse, rice chaff, refuse derived fuel, nut shells, oil-bearing soils, sewage slug
Gaseous waste fuels	Landfill gas, pyrolysis gas

Manufacturing of cement

There are four processes to manufacture the cement at an industrial scale namely I) wet process II) semi-wet process III) semi-dry process IV) dry process. All these processes involve the similar main stages i.e. (a) preparation of raw meal (b) production of clinkers (c) grinding of clinkers and blending figure 3-2. These processes differ significantly in preparation of the raw meal. The dry process is the most employed process in cement production due to its cost-efficiency. Additionally, preheaters and pre-calciner are added to the dry process to further increase the efficiency of the dry process. Figure 3-2 shows a process flow diagram of modern cement manufacturing plant. Each stage among the above mentioned stages can involve multiple unit operations or processes and are explained in detail in the following.

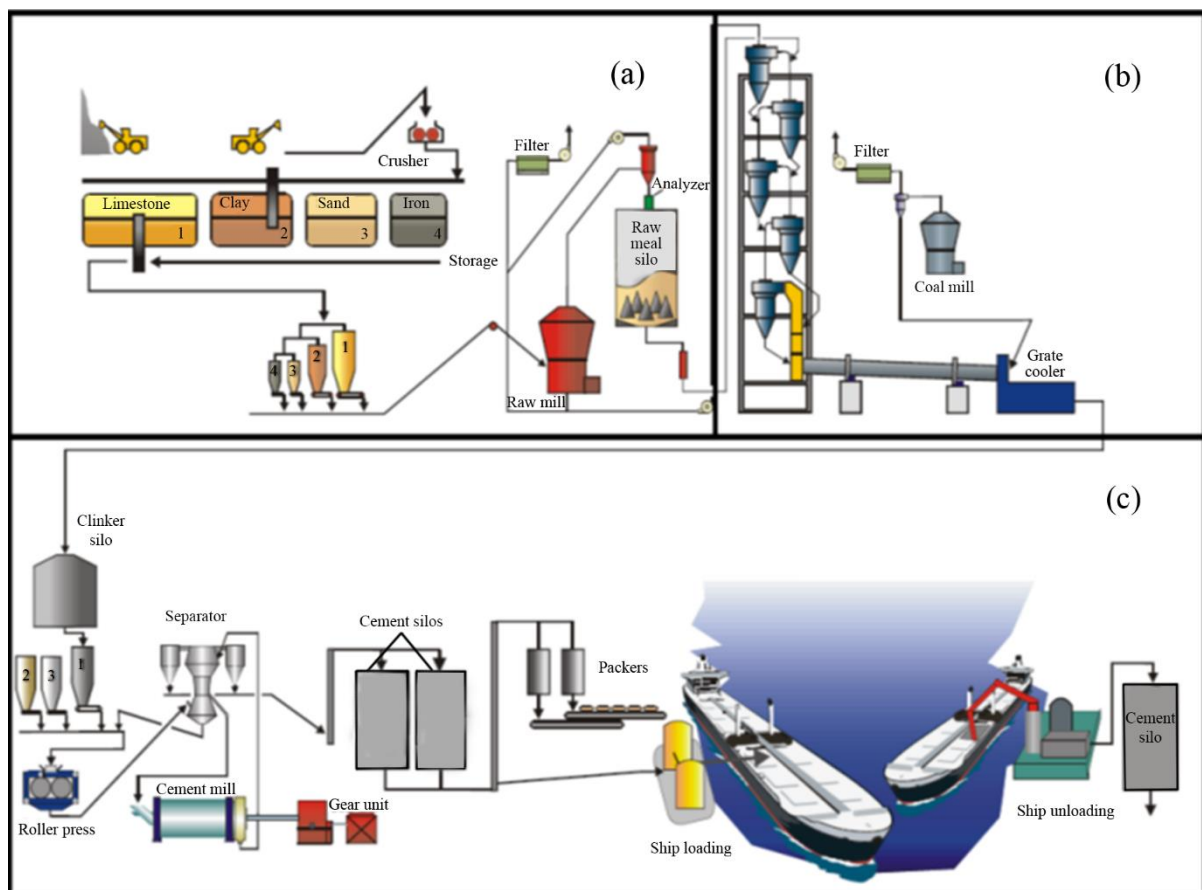


Figure 3-2: Process flow diagram of cement manufacturing a) Preparation of raw material b) Production of clinkers c) Production of cement.

Preparation of Raw Meal

Cement plants are usually located closely either to the market or to the areas with sufficient quantities of raw materials. The purpose is to keep transportation costs low. Basic constituents for cement like limestone and clay are taken from quarries in these areas.

The raw materials are often blended with a variety of raw ingredients to obtain the raw material which could ensure the cement with desired chemical composition. The blended raw materials are ground into small particles in the form of a slurry (the wet process) or in dry form (the dry process) [Taylor (1990), Peray and Waddell (1972)]. In wet process, the feedstock is often prepared with a moisture content of >15 wt.% and then water is added in order to achieve a slurry with a water content of 25-50 wt.% in the wet process. The wet method ensures a high uniformity of raw meal. However, the added water must be evaporated during burning. Since the evaporation of the water is very energy intensive, the production of cement through wet method has decreased over the years. The dry process is the most employed process in cement production due to its cost-efficiency. The process description of modern cement plant is discussed here (dry method-based including preheaters and pre-calciners) followed by an insight into other processes of cement manufacturing.

Production of the clinker

Pre-heating

The raw meal enters the preheater tower which is 50-120 m high and consists of 4-6 cyclones as shown in figure 3-3(a). It is heated by direct contact with counter-current hot flue gases coming from the calciner. The temperature of the raw meal increases from 200 °C to 800 °C in a very short time. Moisture and organic compounds are released or converted in the preheater.

Calcination

The preheated material enters the calciner as shown in figure 3-3(b) at about 800 °C. The hot gases coming from the rotary kiln provide the energy required for calcination (decarburization) reaction which is endothermic in nature. An additional energy is also

needed for this reaction and is provided by the combustion of the fuel. Tertiary air i.e. hot air coming from the clinker cooler is used as combustion air. The fuel used in this stage accounts up to the 60% of the fuel utilized in the cement manufacturing. 90-95% degree of decarburization is achieved in this step [Nørskov et al. (2012)]. and the material reaches a temperature of about 900 °C [vdz-online.de].

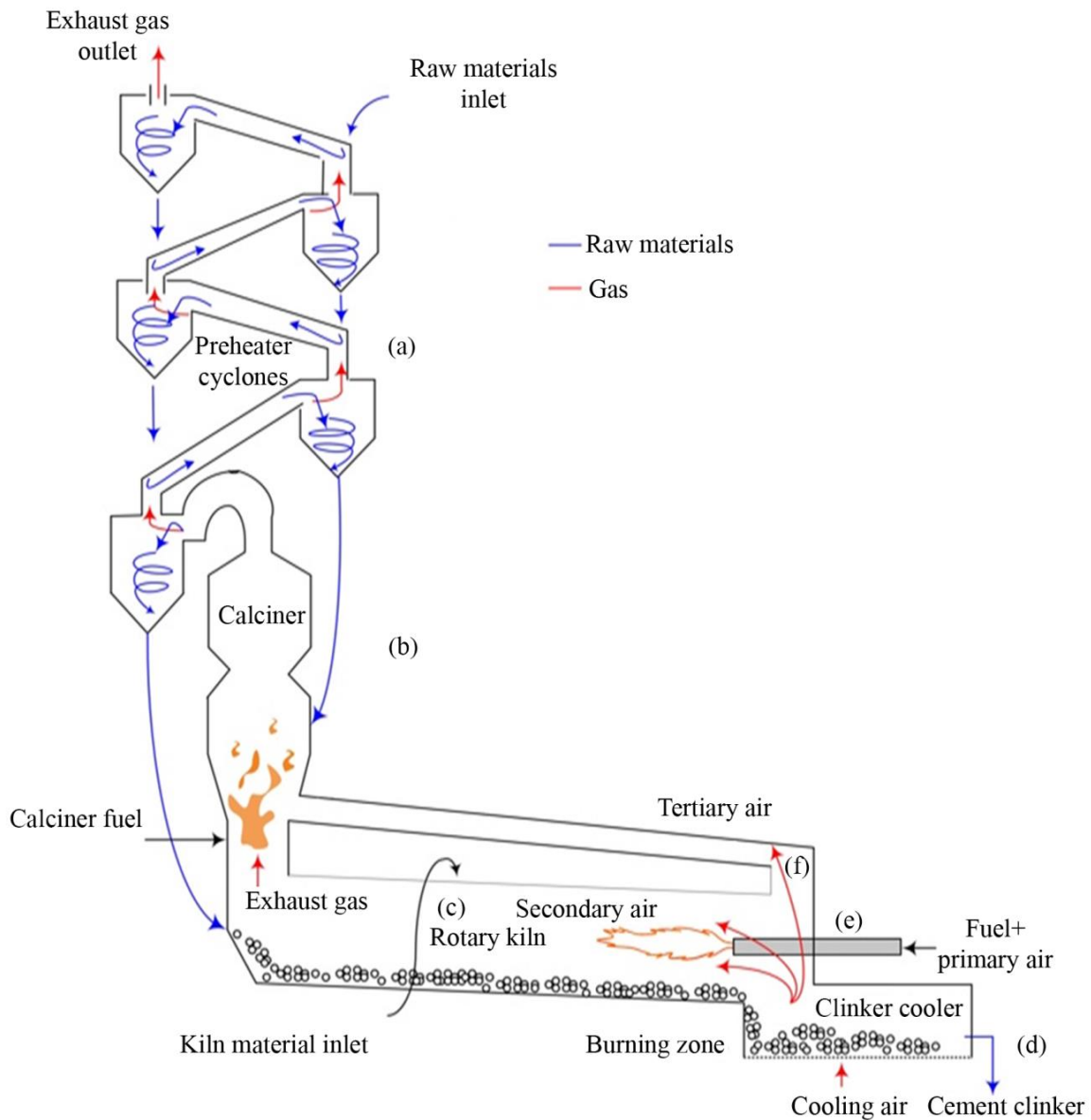


Figure 3-3: An in-line calciner pre-heating system a) preheater tower b) the pre-calciner c) rotary kiln d) the clinker cooler e) burner and secondary air inlet f) tertiary air pass [Nørskov et al. (2012)].

Clinkerization

The pre-calcined solid material enters the kiln at the elevated end. Fuel along with primary air enters the kiln at lower end of the kiln. The fuel undergoes combustion and produces a flame with temperatures of around 2000 °C. Secondary air from the clinker cooler is also utilized for combustion (Fig. 3-3e). The calcined meal is heated by the gas and hot kiln wall to reach a temperature up to ~1500 °C. The material undergoes several chemical reactions and mineralogical changes in the different zones of the kiln i.e decomposition of the uncalcined CaCO_3 and formation of the clinker, formation of the belite, alite, aluminate, and ferrite phases. The clinker consists of silicates, aluminates and ferrites of calcium. Table 3-3 enlists the major components of the clinker along with their chemical formulas.

Table 3-3: Major compounds of Clinker

Compounds	Chemical formula	Notation	Name
Tri-calcium silicate	$3\text{CaO} \times \text{SiO}_2$	C_3S	Alite
Di- calcium silicate	$2\text{CaO} \times \text{SiO}_2$	C_2S	Belite
Calcium aluminate	$3\text{CaO} \times \text{Al}_2\text{O}_3$	C_3A	Aluminate
Calcium ferrite	$4\text{CaO} \times \text{Al}_2\text{O}_3 \times \text{Fe}_2\text{O}_3$	C_4AF	Ferrite

Clinker cooling

The clinker leaves the kiln at a temperature of around 1200-1500 °C. The clinker must be cooled down rapidly to 100 °C. The cooling of clinkers does not only make their handling and transportation easier by reducing their temperature but also improves the overall efficiency of the process by recovering heat from the hot clinker. This recovered heat is used for preheating the air, utilized in the burning process both in the kiln and/or the pre-calciner.

Grinding of clinkers and blending

The cooled clinkers are ground, typically in ball mill to obtain a fine powder. This fine powder is called cement. Cement is blended with gypsum anhydrite to obtain a better control on the setting of cement on hydration. Other additives such as slag from blast

furnace, fly ash and limestone can also be added to ground clinker to obtain the other type of cements.

Process types

The different stages prior to sintering can occur in the kiln itself or in other equipment depending on the process of manufacturing of cement. Raw materials are dried in the kiln in the wet process. Preheating of the material is carried out in the kiln during wet and dry process involving long dry kilns while it is achieved in additional components like preheating tower in other dry processes. Figure 3-4 summarizes the various stages involved in the manufacturing process along with their location.

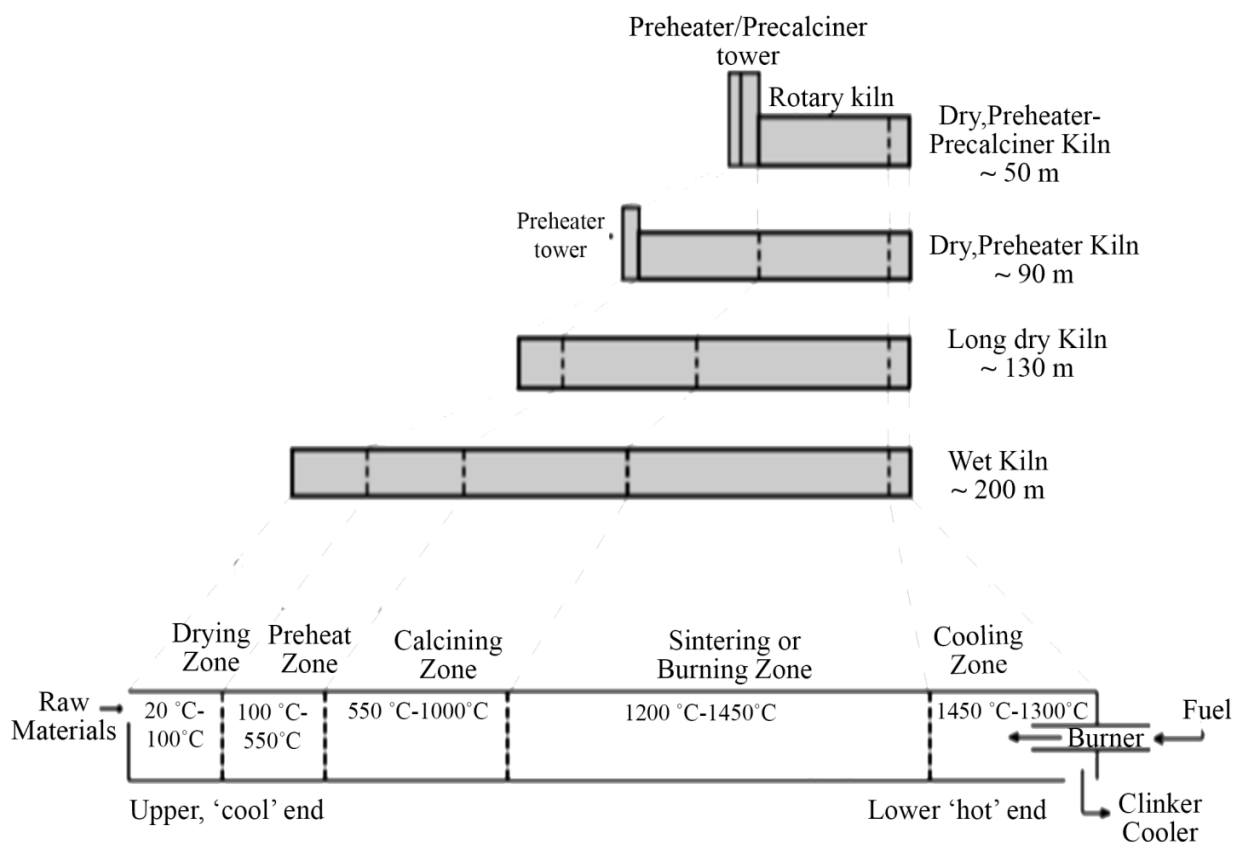


Figure 3-4: Various stages involved in the manufacturing process and their location.

3.1.2 Process model implementation

The material undergoes various physical and chemical changes during production of clinkers. The important reactions, their temperature range, and heat of these reactions are shown in table 3-4.

Table 3-4: Chemical and physical changes in the process [Mintus et al. (2006)].

Reaction	Chemical reaction	Temperature range	Heat of reaction
Water evaporation	$H_2O_{liq} \rightarrow H_2O_{vap}$	0-100 °C	+2493 kJ/kg H_2O [Spang (1972)]
Calcination	$CaCO_3 \rightarrow CaO + CO_2$	550-960 °C	+1780 kJ/kg $CaCO_3$ [Specht (1993)]
C₂S Belite formation	$2CaO + SiO_2 \rightarrow 2CaO \cdot SiO_2 (C_2S)$	900-1200 °C	-732 kJ/kg C_2S [Spang (1972)]
C₃S Alite formation	$C_2S + CaO \rightarrow 3CaO \cdot SiO_2 (C_3S)$	1200-1280 °C	+59 kJ/kg C_3S [Guruz and Bac (1981)]
C₃A Aluminate formation	$3CaO + Al_2O_3 \rightarrow 3CaO \cdot Al_2O_3 (C_3A)$	1200-1280 °C	+25 kJ/kg C_3A [Guruz and Bac (1981)]
C₄AF Ferrite formation	$4CaO + Al_2O_3 + Fe_2O_3 \rightarrow 4CaO \cdot Al_2O_3 \cdot Fe_2O_3 (C_4AF)$	1200-1280 °C	-25 kJ/kg C_4AF [Guruz and Bac (1981)]
Liquid clinker formation	$Clin\ ker_{Sol} \rightarrow Clin\ ker_{Liq}$	>1280 °C	+600 kJ/kg $clinker$ [Guruz and Bac (1981)]

Chemical reactions in the solid phase take place at the interface between crystals and are limited by both diffusion and kinetics. However the data on varying diffusion coefficient with temperature and composition in kiln is not available therefore these reactions are modelled as pseudo-homogeneous reactions [Spang (1972), Mastorkas et al. (1999)]. Spang (1972) had proposed a numerical model to describe the reaction mechanism of each component. The rates of chemical reactions based on Arrhenius law and each component reaction, is described by a mass fraction (X_i).

Ordinary differential equation (3-1 to 3-11) for axial evolution of the components involved in the reaction are written below:

$$\frac{dX_{CaO}}{dz} = \left(k_{CaCO_3} \cdot X_{CaCO_3} - k_{C_3S} \cdot X_{CaO} \cdot X_{C_2S} - k_{C_2S} \cdot X_{SiO_2} \cdot X_{CaO}^2 - k_{C_3A} \cdot X_{CaO}^3 \cdot X_{Al_2O_3} - k_{C_4AF} \cdot X_{CaO}^4 \cdot X_{Al_2O_3} \cdot X_{Fe_2O_3} \right) \cdot \frac{1}{v_S}, \quad (3-1)$$

$$\frac{dX_{SiO_2}}{dz} = \left(-\frac{\tilde{M}_{SiO_2}}{2\tilde{M}_{CaO}} \cdot k_{C_2S} \cdot X_{SiO_2} \cdot X_{CaO}^2 \right) \cdot \frac{1}{v_S}, \quad (3-2)$$

$$\frac{dX_{Al_2O_3}}{dz} = \left(-\frac{\tilde{M}_{Al_2O_3}}{4\tilde{M}_{CaO}} \cdot k_{C_4AF} \cdot X_{CaO}^4 \cdot X_{Al_2O_3} \cdot X_{Fe_2O_3} - \frac{\tilde{M}_{Al_2O_3}}{3\tilde{M}_{CaO}} \cdot k_{C_3A} \cdot X_{CaO}^3 \cdot X_{Al_2O_3} \right) \cdot \frac{1}{v_S}, \quad (3-3)$$

$$\frac{dX_{Fe_2O_3}}{dz} = \left(-\frac{\tilde{M}_{Fe_2O_3}}{4\tilde{M}_{CaO}} \cdot k_{C_4AF} \cdot X_{CaO}^4 \cdot X_{Al_2O_3} \cdot X_{Fe_2O_3} \right) \cdot \frac{1}{v_S}, \quad (3-4)$$

$$\frac{dX_{CO_2}}{dz} = \left(\frac{A_S}{A_G} \cdot \frac{\rho_S}{\rho_G} \cdot \frac{\tilde{M}_{CO_2}}{\tilde{M}_{CaO}} \cdot k_{CaCO_3} \cdot X_{CaCO_3} \right) \frac{1}{v_G}, \quad (3-5)$$

$$\frac{dX_{CaCO_3}}{dz} = \left(\frac{\tilde{M}_{CaCO_3}}{\tilde{M}_{CaO}} \cdot k_{CaCO_3} \cdot X_{CaCO_3} \right) \cdot \frac{1}{v_S}, \quad (3-6)$$

$$\frac{dX_{C_3S}}{dz} = \left(\frac{\tilde{M}_{C_3S}}{\tilde{M}_{CaO}} \cdot k_{C_3S} \cdot X_{CaO} \cdot X_{C_2S} \right) \cdot \frac{1}{v_S}, \quad (3-7)$$

$$\frac{dX_{C_2S}}{dz} = \left(-\frac{\tilde{M}_{C_2S}}{2\tilde{M}_{CaO}} \cdot k_{C_2S} \cdot X_{CaO}^2 \cdot X_{SiO_2} - \frac{\tilde{M}_{C_2S}}{\tilde{M}_{CaO}} \cdot k_{C_3S} \cdot X_{CaO} \cdot X_{C_2S} \right) \cdot \frac{1}{v_S}, \quad (3-8)$$

$$\frac{dX_{C_3A}}{dz} = \left(\frac{\tilde{M}_{C_3A}}{3\tilde{M}_{CaO}} \cdot k_{C_3A} \cdot X_{CaO}^3 \cdot X_{Al_2O_3} \right) \cdot \frac{1}{v_S}, \quad (3-9)$$

$$\frac{dX_{C_4AF}}{dz} = \left(\frac{\tilde{M}_{C_4AF}}{4\tilde{M}_{CaO}} \cdot k_{C_4AF} \cdot X_{CaO}^4 \cdot X_{Al_2O_3} \cdot X_{Fe_2O_3} \right) \cdot \frac{1}{v_S}, \quad (3-10)$$

$$\frac{dX_{H_2O}}{dz} = \left(k_{H_2O} \cdot X_{H_2O} \right) \cdot \frac{1}{v_G}, \quad (3-11)$$

where v_G is the gas velocity in m/s, ρ_G is the average gas density in kg/m³, A_G is the Cross-sectional area for gas flow m², v_S is the bed velocity in m/s, ρ_S is the bed density in kg/m³ and A_S is the cross-sectional area for bed in m².

A_S and A_G are calculated by

$$A_S = R^2[\gamma - 0.5 \sin(2\gamma)] \quad , \quad (3-12)$$

$$A_G = R^2[\pi - \gamma + 0.5 \sin(2\gamma)] \quad , \quad (3-13)$$

where γ is the filling degree in radians.

Arrhenius law can be written to obtain the rate constant of the reaction as

$$k_i = k_{A,i} \exp\left(\frac{-E_{a,i}}{R_{uni} \cdot T_S}\right), \quad (3-14)$$

where T_S is the solid temperature in K, R_{uni} is the universal gas constant, $k_{A,i}$ is the Arrhenius constant, and $E_{a,i}$ is the activation energy in J/mol and k_i reaction rate constant, and i represent the chemical species i.e. CaCO₃, C₂S, C₃S, C₄AF, C₃A, H₂O and CO₂. The values of $k_{A,i}$ and $E_{a,i}$ are given in table 3-5.

Table 3-5: Parameters of reaction kinetic of cement rotary kilns [Sadighi et al. (2010)].

Component	$k_{A,i}$ (1/s)	$E_{a,i}$ (J/kg/mol)
H_2O	1.9×10^4	4.2×10^7
$CaCO_3$	4.55×10^{31}	8×10^8
C_3S	1.3×10^5	2.5×10^8
C_2S	4.1×10^5	1.9×10^8
C_3A	8.3×10^6	1.9×10^8
C_4AF	8.3×10^8	1.8×10^8

With equation 3-1 to 3-14 the heat of reaction in the solid bed can be calculated as

$$dR_S = \frac{A_S \cdot \rho_S}{1 + X_{Al_2O_3} + X_{Fe_2O_3} + X_{SiO_2}} \cdot \left[-\Delta h_{u,CaCO_3} k_{CaCO_3} X_{CaCO_3} - \Delta h_{u,H_2O} k_{H_2O} X_{H_2O} \right. \\ \left. - \Delta h_{u,C_2S} k_{C_2S} X_{SiO_2} X_{CaO}^2 - \Delta h_{u,C_3S} k_{C_3S} X_{CaO} X_{C_2S} \right] \quad (3-15)$$

where X_{H_2O} , X_{CaCO_3} , X_{C_3S} , X_{C_2S} , $X_{Al_2O_3}$, $X_{Fe_2O_3}$, X_{SiO_2} , and X_{CaO} are the initial mass fractions of water, CaCO₃, C₃S, C₂S, Al₂O₃, Fe₂O₃, SiO₂ in relation to CaO i.e. kg of species per kg of CaO respectively.

During the reaction of the cement decomposition the release of H₂O and CO₂ vary along the kiln length and hence the mass of the material is subjected to mass change throughout the kiln,

$$\dot{M}_S(z) = \dot{M}_{S,0} - \left[\dot{M}_{S,0} \cdot x_{H_2O} \cdot U_S(z) - \dot{M}_{S,0} \cdot x_{CO_2} \cdot U_S(z) \right], \quad (3-16)$$

where $\dot{M}_{S,0}$ is the mass flow rate of cement.

3.2 Limestone

3.2.1 Limestone processing

Limestone is a sedimentary rock composed of the mineral calcite (CaCO₃) mostly with impurities like quartz, gypsum along with small amounts of other minerals. It is an important raw material for many process industries such as: water and waste water treatment, surface coats and paints, petroleum refining, chemical synthesis, fertilizer manufacturing, etc. Limestone contains a high concentration of calcium carbonate (CaCO₃) and is thermally decomposed to produce lime (CaO) and CO₂ in calcination.

Within the 60s till the late 80s lime production was grown steadily from 60 million tonnes in 1960 to 140 million tonnes in 1989.

The production dropped to 116 million tonnes in 2002 due to the economic recession. Lime production is increased drastically three-time to 360 million tonnes worldwide. In Germany, the production of the limestone reached around 6.9 million tonnes in

2015 [USGC.gov]. Figure 3-6 shows the percentage of lime and the major producer of the lime worldwide are shown. China and USA account more than 70% of the worldwide production, while Germany, Brazil, Russia and India account for 11%.

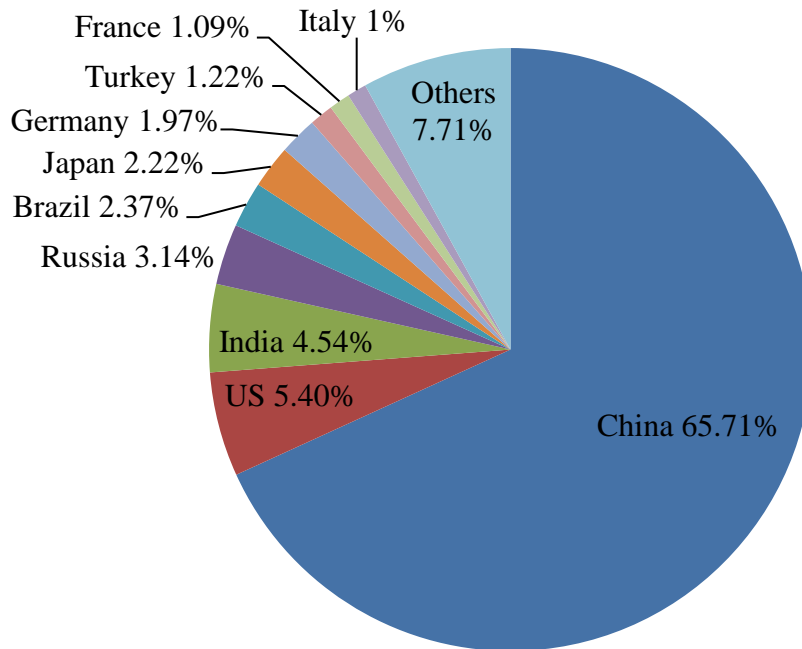


Figure 3-6: World lime production in 2015 [USGC.gov].

Limestone rocks with diameter of one meter are often crushed in primary crushers to size range of 100-250 mm. Depending on the nature of the rock (hardness, lamination, size, etc.) various types of primary crushers are used, such as: jaw crushers, gyratory crushers and impact crushers. Secondary crushers are used for crushing the limestone to obtain a size range of 5-80 mm. As the kiln charge does not have to be very fine. Jaw and impact crushers are also often used as secondary crushers. Material can be then subjected to grinding which produces two different fractions: first one is the coarse fraction where the particle size of the limestone is in the range between 30-70 mm, while the fine fraction represents the particle size below 30 mm. After grinding, the limestone is screened and then transported to storage silos, stockpiles or bunkers for storage prior to feeding into the lime kilns by using belt conveyors and/or bucket elevators. The limestone is sometimes washed in order to reduce the amount of natural sand and clay in washing drums or on screens before it can be fed into the kiln.

Two types of shaft kilns are used in calcining the limestone based on its particle size for the coarse fraction, while in contrast the fine fraction is calcined in rotary kilns.

The calcination of limestone is a highly energy intensive process which accounts for up to 60 % of total production cost of lime. A wide range of fuels including liquid fuels (heavy and/or light fuel oil), solid fuels (coal, coke/anthracite, plastics, paper, animal meal and sawdust) and gaseous fuels (natural gas, coke oven gas) are used in lime kilns.

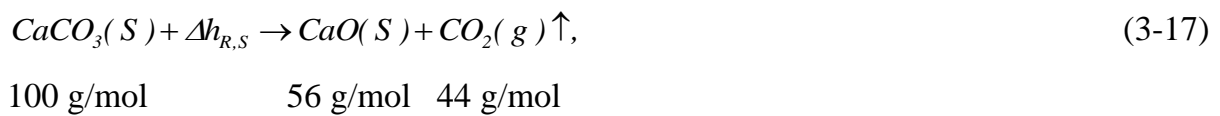
The limestone passes through four zones in a rotary kiln: drying zone, preheating zone, calcination zone and cooling zone during its thermal decomposition. To improve the thermal efficiency of the process, drying, preheating and part of calcination could also be carried out outside the kiln in cyclone preheater. In order to achieve higher degree of calcination, precalciner could also be used. These zones and the processes undergone by limestone are explained as follows:

Drying zone: Limestone loses its physical water by direct contact with the gases leaving the calcining zone. Preheating zone: Limestone is heated to temperature of about 800 °C by direct contact with the gases leaving the calcining zone. These gases are composed mainly of combustion products along with excess air and CO₂ from calcinations. Burning zone or calcining zone: The material is heated to 800 to 1300 °C in flame region in this zone. Decomposition of limestone starts in this region at around 800-850 °C. The temperature at which limestone is decomposed and its residence time in the kiln has major impact on the quality hence, the reactivity of the produced lime. At relatively lower temperature, the outer core of limestone changes to lime, while the inner core does not undergo complete calcination. Thus, the obtained product contains both unburnt carbonate and lime and is called under-burnt lime. As the temperature is further increased, all the introduced lime stone changes to lime thereby, producing a porous and highly reactive product named as soft burnt lime. At further increase in temperature at this stage causes the lime to react with leaving CO₂ to produce limestone again at the surface of the particle. The lime of decreased porosity and reactivity is obtained and is called hard burnt or dead burnt lime. It is suggested that the limestone must be exposed to low temperature with low residence time in kiln to achieve complete calcination. Cooling zone: After reaching the maximum temperature

in the region of the flame end, the material temperature decreases. This region is termed as cooling zone.

3.2.2 Process model implementation

Limestone is decomposed to CaO and CO₂ during calcination. Reaction which is an endothermic reversible reaction and is represented by the chemical equation



where $\Delta h_{R,S}$ is the molar enthalpy of the reaction.

During which CO₂ is generated and enters the kiln gas. The minimum temperature required for the calcination reaction to occur is around 815°C. However, temperatures above 1150°C result in over burning of the lime [Venkatesh (1992)].

Shrinking core model represents the mechanism of decomposition of limestone Cheng and Specht (2006). The sequence of steps during conversion of limestone to lime includes five sub-processes as shown in Figure 3-7.

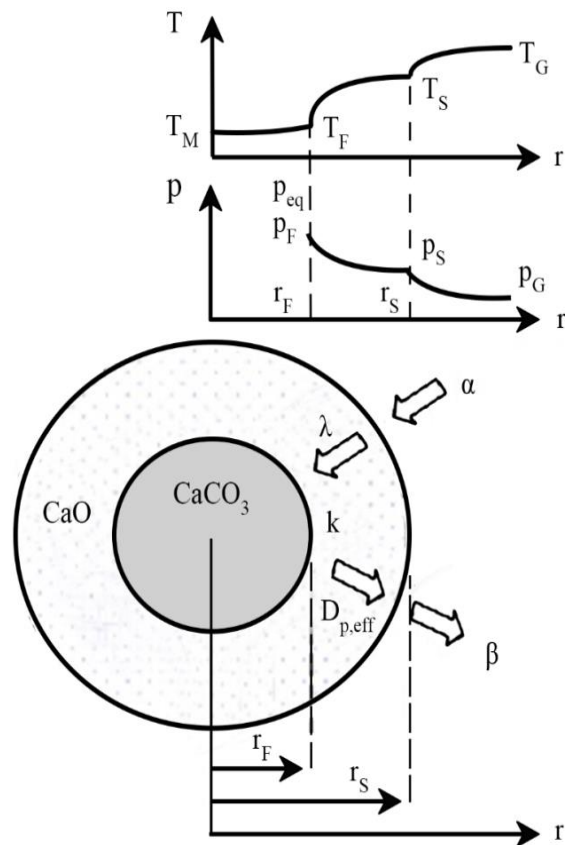


Figure 3-7: Temperature and partial pressure of CO_2 profiles during the calcination of limestone [Cheng and Specht (2006)].

Heat transfer from gas at temperature T_G to the partial surface at temperature T_S occurs through radiation and convection at radius r_S and is symbolized by α .

The heat transport by conduction through the porous lime layer to the reaction front (r_F) of the limestone layer at temperature T_F and is represented by λ .

The decomposition reaction of the CaCO_3 to CaO and CO_2 occurs at the interface which is denoted by k . The driving force of the reaction is the difference between the partial pressure of the CO_2 (p_F) and the equilibrium pressure of CO_2 (p_{eq}) at the interface i.e. radius r_F . The enthalpy of calcination reaction is much higher than the internal energy and as consequence, the heat transport into limestone particle is negligible and the core temperature (T_M) is only slightly lower than the T_F . Front pressure p_F is considerably higher than the partial pressure of the CO_2 at solid-gas interface (p_S) and bulk gas (p_G) because of the generation of CO_2 during the reaction.

The generated CO₂ at the reaction interface is transported through the porous lime layer to the outer surface of the particle represented with D_{p,eff} to maintain the continuity of calcination reaction at the reaction interface.

CO₂ leaves outer surface of the particle to the bulk gas with a partial pressure of CO₂ (p_G) through convective transport (β).

The model is established based on assumptions of particles of limestone being spherical, homogeneous chemical composition and structure of particle, and symmetrical heat supply. The reaction starts uniformly on the surface of solid, forms a smooth reaction front and progresses into the interior surface of particle continuously. Cheng and Specht (2006) analyzed the reaction coefficient and derived couple of differential equations for the shrinking core model to calculate the decomposition temperature (T_F) and the conversion degree (U_S) depending on time (t) as

$$\frac{dU_S}{dt} \cdot [R_\alpha + R_\lambda \cdot f_1(U_S)] = I, \quad (3-18)$$

$$\frac{dU_S}{dt} \cdot [R_\beta + R_D \cdot f_1(U_S) + R_K \cdot f_2(U_S)] = I, \quad (3-19)$$

where $f_1(U_S)$ and $f_2(U_S)$ are the form functions in dependence on particle assumed as spheres ($b = 2$) and are defined as

$$f_1(U_S) = 2 \cdot \left[(1 - U_S)^{-\frac{1}{3}} - 1 \right], \quad (3-20)$$

$$f_2(U_S) = \frac{1}{3} (1 - U_S)^{-\frac{2}{3}}, \quad (3-21)$$

where U_S is the conversion degree and R with subscripts α, λ, K, D_{P,eff}, β are the resistances of transport processes and are given by

$$R_\alpha = \frac{x_{CO_2} \cdot \Delta h_{CO_2} \cdot r_S}{T_G - T_F \cdot \alpha \cdot 2}, \quad (3-22)$$

$$R_\lambda = \frac{x_{CO_2} \cdot \Delta h_{u,CO_2}}{T_G - T_F} \cdot \frac{r_s^2}{4 \cdot \lambda}, \quad (3-23)$$

$$R_K = \frac{x_{CO_2} \cdot R_{CO_2} \cdot T_F}{p_{eq} - p_G} \cdot \frac{r_s}{K}, \quad (3-24)$$

$$R_D = \frac{x_{CO_2} \cdot R_{CO_2} \cdot T_F}{p_{eq} - p_G} \cdot \frac{r_s^2}{4 \cdot D_{p,eff}}, \quad (3-25)$$

$$R_\beta = \frac{x_{CO_2} \cdot R_{CO_2} \cdot T_F}{p_{eq} - p_G} \cdot \frac{r_s}{\beta \cdot 2}, \quad (3-26)$$

where x_{CO_2} is the concentration of CO₂ in limestone, e.g. 1190 kg_{CO2}/m³ for a pure limestone with a density of about 2700 kg/m³, $\Delta h_{u,CO_2}$ is the specific reaction enthalpy and has a value of 3820 kJ/kg_{CO2} at 900°C, k is the reaction rate coefficient in m/s, $D_{p,eff}$ is the pore diffusion coefficient in m²/s, p_{eq} is the equilibrium pressure in Pa, α is the heat transfer coefficient in W/m²/K, β is the mass transfer coefficient in m/s and λ is the thermal conductivity coefficient in W/m/K. Silva et al. (2009) related the decomposition temperature with equilibrium pressure as

$$p_{eq} = p_{max} \cdot \exp\left(-\frac{\Delta h_{R,S}}{R_{uni} \cdot T_S}\right), \quad (3-27)$$

where p_{max} is the pre-exponential coefficient or frequency factor 2.15×10^7 bar, $\Delta h_{R,S}$ is the molar reaction enthalpy with 168 kJ/mol at 900°C, R_{uni} is the universal gas constant (8.314 J/mol/K), T_S is the solid temperature in K.

Cheng and Specht (2006) determined the reaction rate coefficients (k_{CaCO_3}) from the linearized conversion curves for various types of limestone as shown in figure 3-8. The reaction rate coefficient ranged from 0.003 to 0.012 m/s and averaged to 0.005 m/s for most of their calculations independent of temperature.

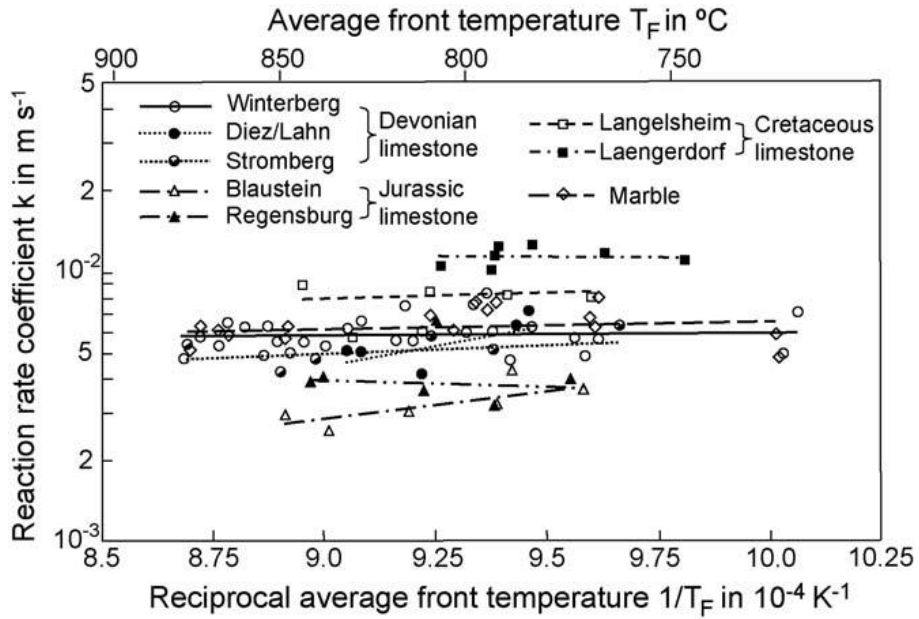


Figure3-8: Reaction rate coefficients of various types of limestone [Cheng and Specht (2006)].

As described before that only fine fractions of limestone are handled in the rotary kiln, it is assumed that the heat conduction and CO₂ diffusion in the porous lime layer is negligibly small which leads to a reduction of eqs 3-18 and 3-19 to eqs

$$\frac{dU_{s, CaCO_3}}{dt} \cdot [R_\alpha] = 1, \quad (3-28)$$

$$\frac{dU_{s, CaCO_3}}{dt} \cdot [R_\beta + R_K \cdot f_2(U_s)] = 1. \quad (3-29)$$

Then the spatial conversion of the limestone over the kiln length is given by:

$$\frac{dU_{s, CaCO_3}}{dz} = \frac{dU_{s, CaCO_3}}{dt} \cdot \frac{1}{v_p}, \quad (3-30)$$

with the particle velocity:

$$v_p = \frac{\dot{M}_s}{\rho_s} \cdot \frac{1}{A_s}, \quad (3-31)$$

$$A_s = R^2 \cdot (\gamma - \sin \gamma \cdot \cos \gamma). \quad (3-32)$$

The heat of reaction can be calculated with:

$$\frac{dR_{s, CaCO_3}}{dz} = \frac{dU_{s, CaCO_3}}{dz} \cdot \dot{M}_s(z) \cdot x_{CO_2} \cdot \Delta h_{u, CO_2}, \quad (3-33)$$

where $\Delta h_{u, CO_2}$ is the specific reaction enthalpy according to produced CO₂ with 3820 kJ/kg CO₂.

During the reaction of the limestone decomposition the release of CO₂ varies along the kiln length and hence the mass of the material is subjected to mass change throughout the kiln,

$$\dot{M}_s(z) = \dot{M}_{s,0} - \dot{M}_{s,0} \cdot x_{CO_2} \cdot U_{s, CaCO_3}(z), \quad (3-34)$$

where $\dot{M}_{s,0}$ is the inlet mass flow rate of limestone.

and the mass released from CO₂ to the gas phase

$$\dot{M}_{s, loss}(z) = x_{CO_2} \cdot [1 - U_s(z)] \cdot \dot{M}_{s,0} \quad (3-35)$$

3.3 Magnesite

3.3.1 Magnesite processing

Magnesite is formed by alteration of magnesium-rich rocks on their contact with carbonate-rich solutions during metamorphism. Magnesite has the same crystal structure as that of calcites and its properties are either identical or similar to those of calcite. Magnesite is cut, drilled, and polished to form beads which are used in making jewelry. Magnesite (MgCO₃) serves as a raw material for magnesia. Sintered or dead burned magnesia acts as an excellent refractory material in various industries such as steel industry, cement industry, lime industry etc [minerals.usgs.gov, GeoScience (2008), Hamilton (2000)]. Magnesite decomposes at high temperature to magnesium

oxide (MgO) and carbon dioxide (CO₂) which releases makes around 52% from the amount of the raw material [Ongstad et al. (1992), Sivertsen. et al. (2003)]. The world's production of magnesite was around 5.929 million tonnes in 2011. Due to the demand in the international market, the production increased greatly to reach 27.66 million tonnes in 2016 [statista.com]. China is the main producer of magnesite with 19 million tonnes.

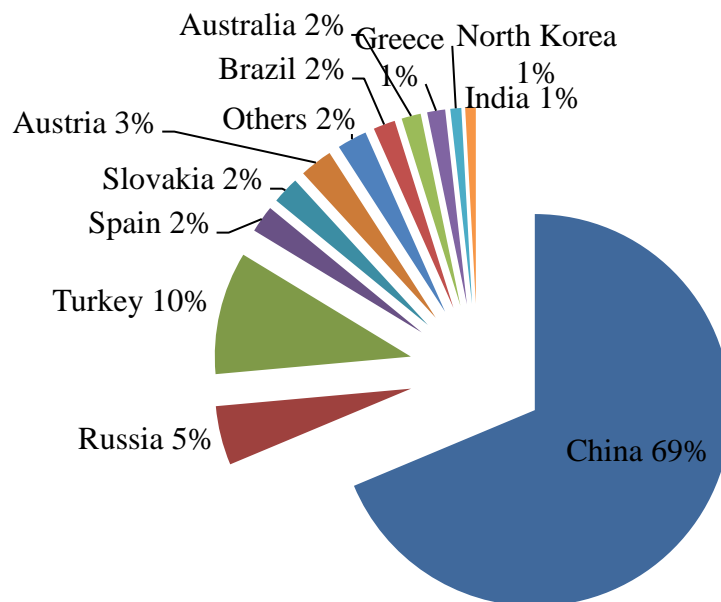


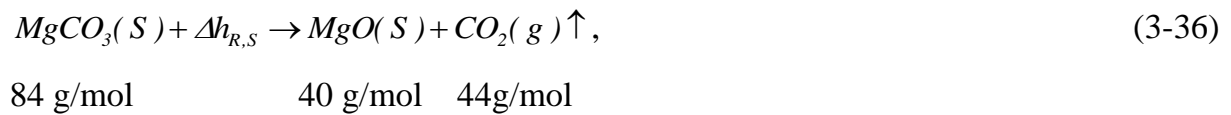
Figure 3-11: Worldwide magnesite production 2016 (1000 Mt) [Statista.com].

Magnesite is mined using open pit and underground mining. The preliminary treatment and first size reduction are achieved during the mining operation. Standard processing units are used for the preparation of raw materials such as crushing, grinding or milling and sieving plants. Various types of primary and secondary crushers are used depending on the nature of the rock, e.g. hardness, sizes. However, the size of the stones should not be too small and only a small amount of fines are permitted in the raw material. For preparing magnesite, a heavy sludge is prepared. Raw materials are sometimes washed in order to exclude impurities. Furthermore, permanent magnet separators are used for preparation of magnets. The kiln type is selected on the basis of raw material and production capacities. The quality of the product depends on the type of kiln and process.

Hearth furnace, a shaft kiln or a rotary kiln can be used for calcination of magnesite. Magnesite is calcined in rotary or shaft kiln to obtain dead burnt magnesia while hearth furnace or rotary kiln are used for the production of the caustic calcined magnesia from magnesite. During the calcination of magnesite in the rotary kiln, it undergoes the similar processes that of limestone during its calcination. But, the decomposition of magnesite takes place at a comparatively lower temperature i.e between 450 and 500 °C.

3.3.2 Process model implementation

Magnesium carbonate decomposes to magnesium oxide (MgO) and carbon dioxide (CO₂). This is an endothermic reaction and can be expressed with:



where $\Delta h_{R,S}$ is the molar enthalpy of the reaction and has value 117 kJ/mol or relative to the mass of produced CO₂ (Δh_{CO_2}) is 2645 kJ/ kgCO₂.

Decomposition of the magnesite can be simulated with the same mathematical model as for limestone. Thus, the shrinking core model can be used to describe the decomposition of magnesite. A Similar equation to equation 3-28 and 3-29 can give the conversion degree (U_s) depending on time (t) as

$$\frac{dU_{S,MgCO_3}}{dt} \cdot [R_\alpha] = 1, \quad (3-37)$$

$$\frac{dU_{S,MgCO_3}}{dt} \cdot [R_\beta + R_K \cdot f_2(U_s)] = 1. \quad (3-38)$$

Specht et al. (1986) determined the equilibrium pressure of CO₂ be approximated by the Arrhenius law

$$p_{eq} = p_{max} \cdot \exp\left(-\frac{\Delta h_{R,S}}{R_{uni} \cdot T_S}\right), \quad (3-39)$$

where p_{max} is the pre-exponential coefficient or frequency factor 2.7×10^8 bar, $\Delta h_{R,S}$ is the molar reaction enthalpy with 117 kJ/mol for $MgCO_3$ decomposition corresponding to 2660 kJ/(kg CO_2), R_{uni} is the universal gas constant (8.314 J/mol/K), T_S is the solid temperature in K.

Specht et al. (1993) studied the decomposition behavior of magnesite from different origins and calculated the reaction rate coefficient from the linearized decomposition behaviour curves which are shown in Figure 3-12. It is evident that the values of reaction rate coefficients differ from one kind of magnesite to another. However, they show nearly the same dependence on the temperature. These values corresponds to the Arrhenius equation

$$k_{MgCO_3} = 5 \times 10^{-2} \text{ to } 5 \times 10^{-1} \cdot \exp\left(-\frac{55 \text{ kJ mol}^{-1}}{R_{uni} \cdot T_S}\right). \quad (3-40)$$

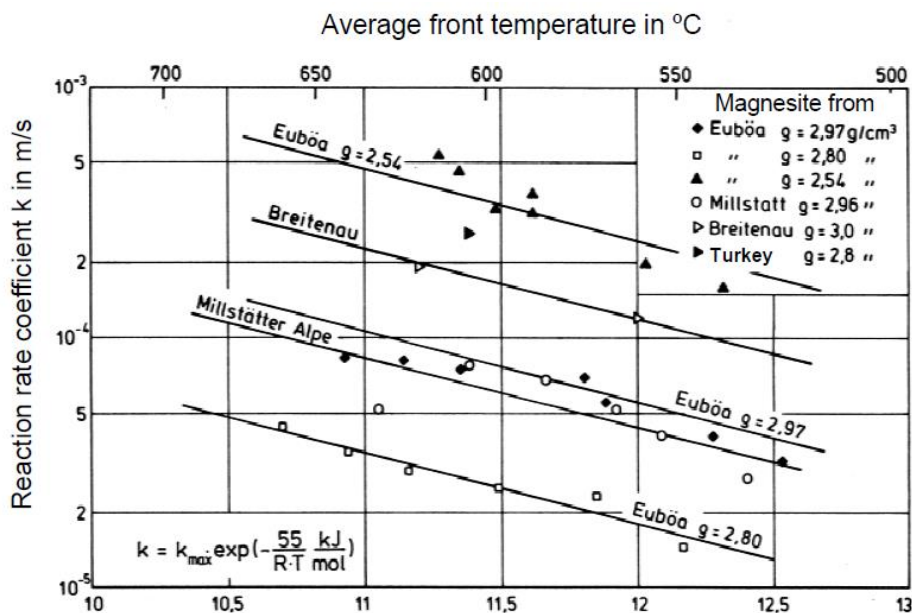


Figure 3-12: Reaction coefficients of magnesite decomposition [Cheng and Specht (2006)].

Then the spatial conversion of the magnesite over the kiln length is given by

$$\frac{dU_{S,MgCO_3}}{dz} = \frac{dU_{S,MgCO_3}}{dt} \cdot \frac{1}{v_p}, \quad (3-41)$$

and the heat of reaction can be calculated with

$$\frac{dR_{S,MgCO_3}}{dz} = \frac{dU_{S,MgCO_3}}{dz} \cdot \dot{M}_S(z) \cdot x_{CO_2} \cdot \Delta h_{u,CO_2}, \quad (3-42)$$

where the Δh_{CO_2} is the specific reaction enthalpy according to produced CO₂ on mass basis and has a value of 2645 kJ/kg_{CO₂}. During the reaction of the magnesite the expelled CO₂ gas varies along the kiln length and hence the mass of the material changes throughout the kiln and is described by the following reaction.

$$\dot{M}_S(z) = \dot{M}_{S,0} - \dot{M}_{S,0} \cdot x_{CO_2} \cdot U_{S,MgCO_3}(z) \quad (3-43)$$

where $\dot{M}_{S,0}$ is the inlet mass flow rate of magnesite.

And the mass losses due to the release of CO₂ to the bulk gas phase is calculated by

$$\dot{M}_{S,loss}(z) = x_{CO_2} \cdot [1 - U_{S,MgCO_3}(z)] \cdot \dot{M}_{S,MgCO_3} \quad (3-44)$$

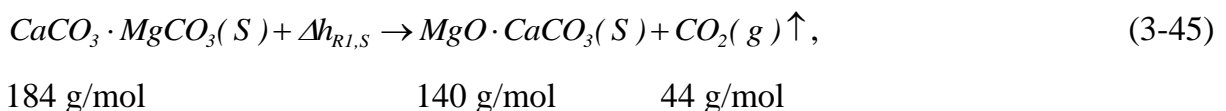
3.4 Dolomite

3.4.1 Dolomite processing

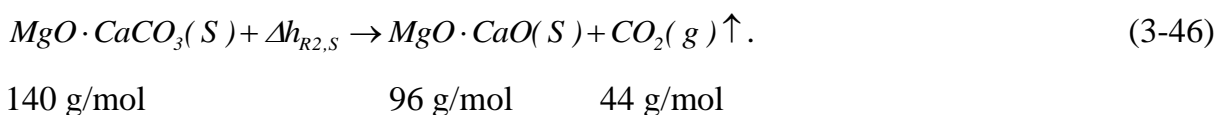
Dolomite ($\text{CaCO}_3 \cdot \text{MgCO}_3$) is comprised of magnesium carbonate (MgCO_3) and calcium carbonate (CaCO_3). Dolomite is mainly used in cement industry as the refractory material. It serves as a fluxing material in blast furnace operation for manufacturing of secondary steel and ferromanganese. To a lesser extent it is used in the glass industry for manufacturing plate glass and fiberglass, and in agriculture, as a fertilizer, soil conditioner and stock feed supplement. [Deer (1966), Vasconcelos et al. (1995), Deelman et al. (1999)]. The dolomite excavated through mining usually contains impurities like alumina, sulphur, iron etc. The level of these impurities dictates the end use of dolomite. Selective mining, careful stripping and blending are carried out for obtaining dolomite with a desired purity. Relatively pure dolomite is used in the production of refractories. The raw material is crushed and screened before feeding to the rotary kiln. It decomposes in two steps while passing through the kiln. In the first step CO_2 is released from the magnesite in dolomite at around 500°C and in the second step limestone decomposes at temperatures around $800\text{-}900^\circ\text{C}$. Both these reactions are endothermic in nature.

3.4.2 Process model implementation

The decomposition mechanism of dolomite can be sequentially in two stages. In the first step the decomposition of MgCO_3 takes place at a temperature range of $520\text{-}730^\circ\text{C}$.



In the second step, CaCO_3 decomposes at a temperature range of $780\text{-}900^\circ\text{C}$:



The general decomposition process can be described with to the shrinking-core-model similar to limestone and magnesite. The calcination process can be explained considering a partially decomposed piece of dolomite with two separate reaction fronts, which are progressing towards the particle center with different velocities. The conversion degree of magnesite and limestone present in dolomite can be calculated as a function of decomposition time t as

$$\frac{dU_{S, CaCO_3 \cdot MgCO_3}}{dt} \cdot [R_\alpha] = 1, \quad (3-47)$$

$$\frac{dU_{S, CaCO_3 \cdot MgCO_3}}{dt} \cdot [R_\beta + R_K \cdot f_2(U_S)] = 1, \quad (3-48)$$

And

$$\frac{dU_{S, MgO \cdot CaCO_3}}{dt} \cdot [R_\alpha] = 1, \quad (3-49)$$

$$\frac{dU_{S, MgO \cdot CaCO_3}}{dt} \cdot [R_\beta + R_K \cdot f_2(U_S)] = 1. \quad (3-50)$$

The equilibrium pressure of carbon dioxide during calcination of magnesite or limestone in dolomite can be approximated by the Arrhenius law [Cheng and Specht (2006)].

$$P_{eq,i} = P_{max,i} \cdot \exp\left(-\frac{\Delta h_{Ri,S}}{R_{uni} \cdot T_S}\right), \quad (3-51)$$

The subscript i is equal to 1 for magnesite and 2 for limestone in dolomite. The values of parameters used in these equations are listed in table 3-10.

Table 3-10: Parameters and their typical values

Parameter	CaCO ₃ ·MgCO ₃	MgO·CaCO ₃
Pre-exponent coefficient ($p_{max,i}$)	$2.7 \times 10^8 \text{ bar}$	$2.15 \times 10^7 \text{ bar}$
Proportion of CO ₂ ($x_{CO_2,i}$)	0.24 kg CO ₂ /kg MgCO ₃	0.238 kgCO ₂ /kgCaCO ₃
Molar reaction enthalpy ($\Delta h_{Ri,S}$)	117 KJ/molMgCO ₃	168 kJ/molCaCO ₃
Specific enthalpy ($\Delta h_{u,CO_2,i}$)	2660 kJ/kgCO ₂	3800 kJ/kgCO ₂

The reaction coefficients are determined by Specht et al. (1986) and are approximated with.

$$k_{CaCO_3 \cdot MgCO_3} = 5 \times 10^{-2} \text{ to } 5 \times 10^{-1} \cdot \exp\left(-\frac{55 \text{ kJ mol}^{-1}}{R_{uni} \cdot T_S}\right), \quad (3-52)$$

$$k_{MgO \cdot CaCO_3} = 220 \cdot \exp\left(-\frac{80 \text{ kJ mol}^{-1}}{R_{uni} \cdot T_S}\right). \quad (3-53)$$

The reaction rate coefficient for MgCO₃ component in first decomposition stage range from $3 \cdot 10^{-5}$ to $5 \cdot 10^{-4}$ m/s between 520 °C and 730 °C and coefficients for the second stage in the temperature range from 0.02 and 0.05 m/s between 780 to 900°C. Then the spatial conversion of the MgCO₃ and CaCO₃ over the kiln length can be given by

$$\frac{dU_{S,CaCO_3 \cdot MgCO_3}}{dz} = \frac{dU_{S,CaCO_3 \cdot MgCO_3}}{dt} \cdot \frac{1}{v_p}, \quad (3-54)$$

$$\frac{dU_{S,MgO \cdot CaCO_3}}{dz} = \frac{dU_{S,MgO \cdot CaCO_3}}{dt} \cdot \frac{1}{v_p}, \quad (3-55)$$

Then the heat of reaction can be calculated according to the following equation:

$$\begin{aligned} \frac{dR_{S,CaCO_3 \cdot MgCO_3}}{dz} &= \frac{dU_{S,CaCO_3 \cdot MgCO_3}}{dz} \cdot \dot{M}_{S,CaCO_3 \cdot MgCO_3}(z) \cdot x_{CO_2,CaCO_3 \cdot MgCO_3} \cdot \Delta h_{u,CO_2,CaCO_3 \cdot MgCO_3} \\ &+ \frac{dU_{S,MgO \cdot CaCO_3}}{dz} \cdot \dot{M}_{S,MgO \cdot CaCO_3}(z) \cdot x_{CO_2,MgO \cdot CaCO_3} \cdot \Delta h_{u,CO_2,MgO \cdot CaCO_3} \end{aligned} \quad (3-56)$$

During the reaction of the dolomite, release of the CO₂ gas varies along the kiln length and the resulting mass change throughout the kiln is given as

$$\begin{aligned} \dot{M}_S(z) = & \dot{M}_{S,0} - \left[\dot{M}_{S,0} \cdot x_{CO_2, CaCO_3 \cdot MgCO_3} \cdot U_{S, CaCO_3 \cdot MgCO_3}(z) \right. \\ & \left. + \dot{M}_{S,0} \cdot x_{CO_2, MgO \cdot CaCO_3} \cdot U_{S, MgO \cdot CaCO_3}(z) \right], \end{aligned} \quad (3-57)$$

where $\dot{M}_{S,0}$ is the mass flow rate of dolomite.

And the mass released from the CO₂ to the bulk gas phase is calculated by

$$\begin{aligned} \dot{M}_{S,loss}(z) = & \left\{ \dot{M}_{S,0} \cdot x_{CO_2, CaCO_3 \cdot MgCO_3} \cdot [1 - U_{S, CaCO_3 \cdot MgCO_3}(z)] \right. \\ & \left. + \dot{M}_{S,0} \cdot x_{CO_2, MgO \cdot CaCO_3} \cdot [1 - U_{S, MgO \cdot CaCO_3}(z)] \right\}. \end{aligned} \quad (3-58)$$

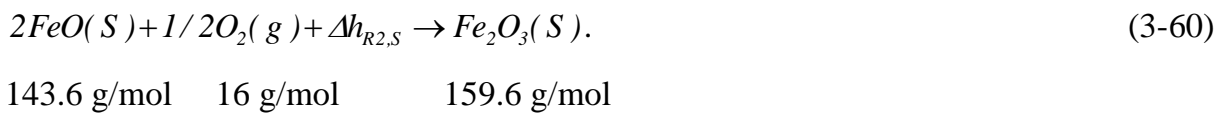
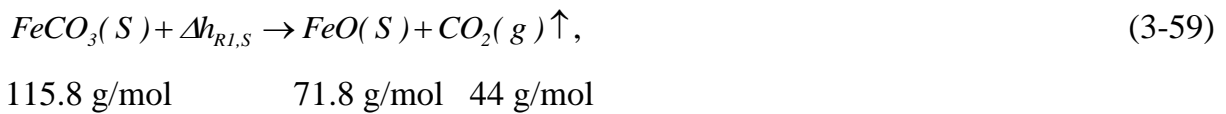
3.5 Siderite

3.5.1 Siderite processing

Siderite (FeCO₃) is one of the main potential sources of iron. It is found as an accessory mineral in some shales and carbonate rocks and in some barite and hematite ores and is composed of 48.2% iron, 37.99% CO₂ and 13.81% oxygen [Alkaç (2007)]. The final products of siderite on calcination are iron oxides including α -Fe₂O₃, γ -Fe₂O₃, Fe₃O₄ and FeO [Gallagher and Warne (1981)]. Siderite is a mineral which finds its application in a variety of industries and is preferred to limonite as a raw material in cement industry. It is used in the steam-iron process for hydrogen production and in the refining of ferrosilicon by removing aluminum. It is also used in the treatment of drilling mud for neutralizing hydrogen sulfide. The decomposition product of siderite is widely used as a natural brown pigment in the paint industry. Siderite occurrences in Europe include Neudorf in the Harz Mountains, Germany and Panasqueira, Portugal. In order to mine siderite ore, benches are developed and blasted. The ore is carried by trucks to the ore crushing plant where it is crushed and moved by belt conveyers. Ore is crushed to a maximum size of 38 mm and then separated from waste by a sink float process. Siderite ore is then recrushed to less than 6.5 mm, and with evenly before sintering.

3.5.3 Process model implementation

The thermal decomposition of mineral siderite produces iron oxide. The mechanism of the thermal decomposition of siderite depends on the kiln atmosphere. The final product is hematite (Fe_2O_3) in an oxidizing atmosphere (O_2 or air) or magnetite (Fe_3O_4) in a CO_2 atmosphere or in vacuum and wustite (FeO) in an inert atmosphere [Chai and Navrotsky (1994), Gotor et al. (2000), Jagtap et al. (1990)]. The decomposition of Siderite takes place in two stages as



The first step of $FeCO_3$ dissociation is an endothermic process and takes place in the temperature range of 475-540 °C. The second step is the oxidation of FeO which is an exothermic process and takes place in the range of 600-890 °C [Teodorovich (1961), Pan and Zhu (2002)]. Thermal decomposition of siderite influenced by many parameters such as heating temperature, gaseous atmosphere, crystallinity, porosity of the material, particle size and availability of oxygen [Alkaç (2007)]. Shrinking core model is used to model the endothermic reaction (calcination reaction), whereas Arrhenius approach is used for exothermic reaction (oxidation reaction).

The conversion degree of calcination can be calculated as a function of decomposition time t

$$\frac{dU_{S,FeCO_3}}{dt} \cdot [R_\alpha] = 1, \quad (3-61)$$

$$\frac{dU_{S,FeCO_3}}{dt} \cdot [R_\beta + R_K \cdot f_2(U_S)] = 1. \quad (3-62)$$

and oxidation of siderite can be calculated as the function of decomposition time

$$\frac{dU_{S,FeO}}{dt} = k_{FeO} \cdot f(U), \quad (3-63)$$

The equilibrium pressure for the calcination reaction is

$$p_{eq,FeCO_3} = p_{max,FeCO_3} \cdot \exp\left(-\frac{\Delta h_{R,FeCO_3,S}}{R_{uni} \cdot T_S}\right) \quad (3-64)$$

the reaction rate coefficient for calcination and oxidation can be calculated as

$$k_{FeCO_3} = k_{A,FeCO_3} \exp\left(\frac{-E_{a,FeCO_3}}{R_{uin} \cdot T_S}\right) \quad (3-65)$$

$$k_{FeO} = k_{A,FeO} \exp\left(\frac{-E_{a,FeO}}{R_{uin} \cdot T_S}\right) \quad (3-66)$$

Then the spatial conversion of the $FeCO_3$ and FeO over the kiln length can be given by the following equation respectively:

$$\frac{dU_{S,FeCO_3}}{dz} = \frac{dU_{S,FeCO_3}}{dt} \cdot \frac{1}{v_P}, \quad (3-67)$$

$$\frac{dU_{S,FeO}}{dz} = \frac{dU_{S,FeO}}{dt} \cdot \frac{1}{v_P}. \quad (3-68)$$

Then the heat of reaction can be calculated according to the following equation:

$$\begin{aligned} \frac{dR_{S,FeCO_3}}{dz} = & \left[\frac{dU_{S,FeCO_3}}{dz} \cdot \dot{M}_{S,FeCO_3}(z) \cdot x_{CO_2,S} \cdot \Delta h_{u,CO_2,FeCO_3} \right. \\ & \left. + \frac{dU_{S,FeO}}{dz} \cdot \dot{M}_{S,FeO}(z) \cdot x_{O_2,S} \cdot \Delta h_{u,O_2,FeO} \right]. \end{aligned} \quad (3-69)$$

The values of parameters used in these equations are listed in table 3-11.

Table 3-11: Parameters and their typical values

Parameter	FeCO ₃	FeO
Pre-exponent coefficient ($p_{max,i}$)	2.7×10^{13} bar	
Proportion (x_i)	0.379 kgCO ₂ /kg FeCO ₃	0.1 kgO ₂ / kg FeO
Molar reaction enthalpy ($\Delta h_{Ri,S}$)	110 kJ/mol FeCO ₃	168 kJ/mol CaCO ₃
Arhenius constant($k_{A,i}$)	0.05 1/s	5×10^4 1/s
Activation energy ($E_{a,i}$)	55 kJ/mol	180 kJ/mol
Specific enthalpy ($\Delta h_{u,CO_2,i}$)	1700 kJ/kg CO ₂	-7000 kJ/kg O ₂

During the reaction of the siderite the release of the CO₂ and addition of O₂ gases varies along the kiln length. Hence, the mass of the material is subjected to mass change throughout the kiln, as shown by the following reaction.

$$\dot{M}_S(z) = \dot{M}_{S,0} - [\dot{M}_{S,0} \cdot x_{CO_2,FeCO_3} \cdot U_{S,FeCO_3}(z) - \dot{M}_{S,0} \cdot x_{O_2,FeO} \cdot U_{S,FeO}(z)] \quad (3-70)$$

and the mass released from the CO₂ to the bulk gas phase or O₂ which added to the bulk bed are calculated as the following:

$$\dot{M}_{S,loss}(z) = \dot{M}_{S,0} \cdot x_{CO_2,FeCO_3} \cdot [I - U_{S,FeCO_3}(z)], \quad (3-71)$$

$$\dot{M}_{S,add}(z) = \dot{M}_{S,0} \cdot x_{O_2,FeO} \cdot [I + U_{S,FeO}(z)], \quad (3-72)$$

where $\dot{M}_{S,0}$ is the inlet mass flow rate of siderite kg/s, $\dot{M}_{S,loss}$ is the mass loss of CO₂ kg/s and $\dot{M}_{S,add}$ is the mass of oxygen added in kg/s.

3.6 Titanium dioxide

3.6.1 Titanium dioxide processing

Titanium dioxide (TiO_2) is a naturally occurring inorganic compound which exists in three polymorphic forms, namely anatase, rutile, and brookite [Kolditz (1980), Gesenhues (2001), Heine et al. (2001)]. The most of TiO_2 is found in the form of anatase. Rutile is the most stable form and possesses excellent pigmentary properties [Dumont and B'elanger (1978)]. TiO_2 is most commonly used as a white pigment. Its brightness and high refractive index makes its suitable to use in coatings such as paints, plastics, paper and inks. It does not only make white opaque coating but can also be used to make colored coatings with other colored pigments by providing them the required hiding power. Higher grade TiO_2 is used in cosmetic industry as it resists the UV light and does not discolor over a long period of exposure. TiO_2 also finds its application in Light emitting diodes (LED), liquid crystal displays due to its photocatalytic properties. It can also increase the acid resistance of vitreous enamels.

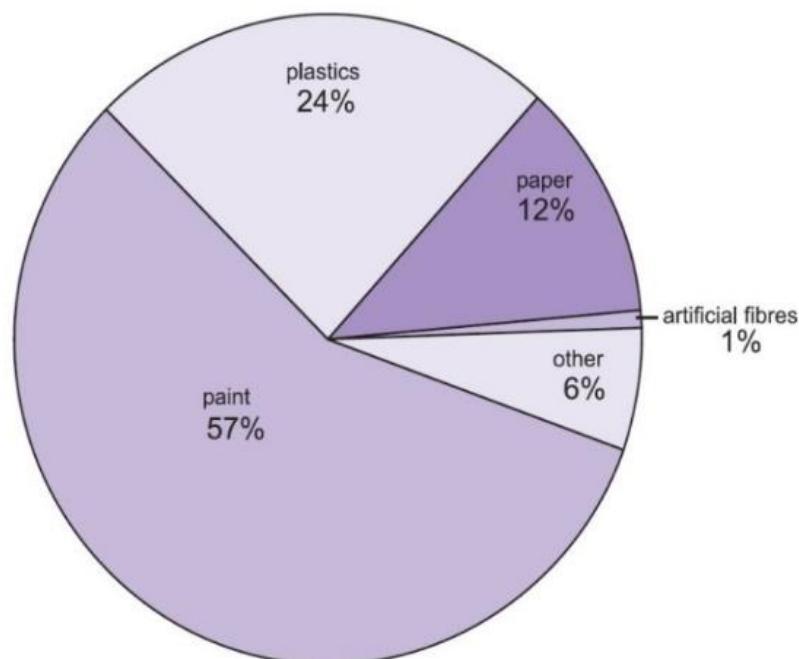


Figure 3-13: Uses of titanium dioxide [essentialchemicalindustry.org]

TiO_2 is mainly obtained from ilmenite ore. Ilmenite is the most abundant ore around the world and contains 53% TiO_2 of titanium dioxide. Rutile is the next most abundant

and contains around 98% titanium dioxide in the ore [Alan (1984)]. TiO_2 is produced on industrial scale by using two processes namely sulphate or chloride. The choice of method depends on the type of ore available and the type of produced pigment. Sulfate process uses ilmenite ore containing 45-60% TiO_2 as a raw material and yields anatase or rutile pigment, while chloride process utilizes rutile ore with 99% of TiO_2 as a raw material to produce rutile pigment. Figure 3-14 gives a brief comparison between these processes.

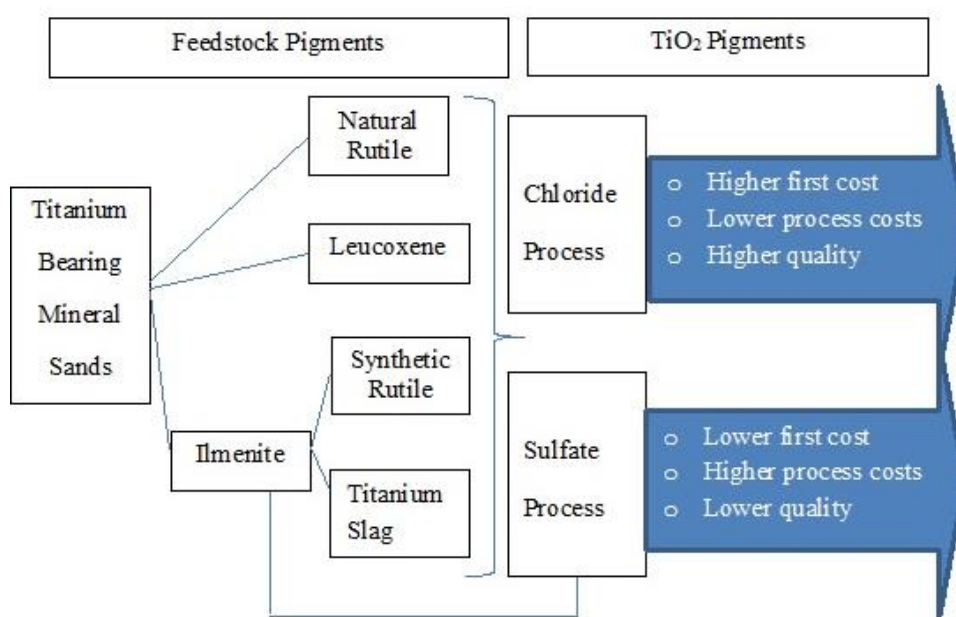


Figure 3-14: Processes of formation of TiO_2 pigments and their feed stock

Sulfate process is an old process and uses simple technology. The flow diagram of this process is shown in the Figure 3-15

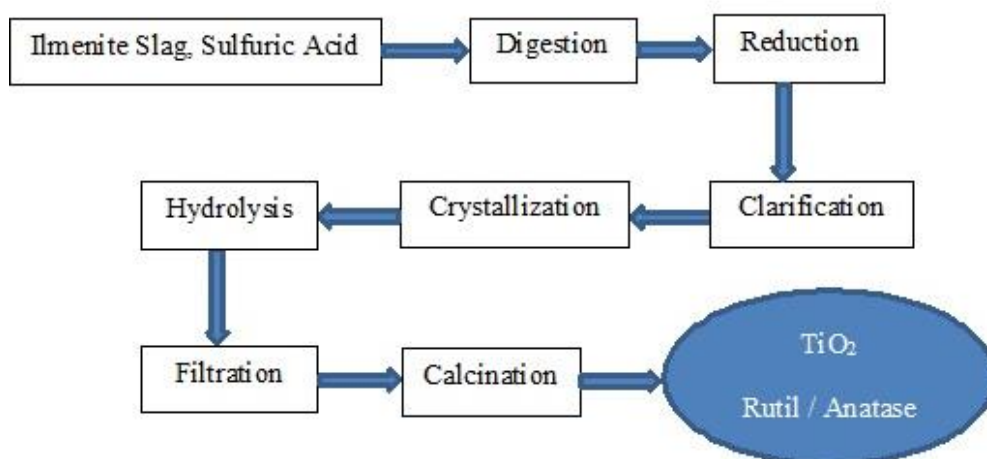
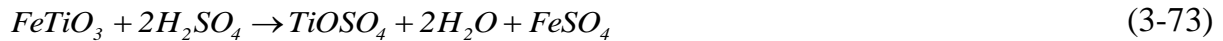


Figure 3-15: Process flow diagram of titanium dioxide

In this process, the raw materials such as ilmenite (FeTiO_3) or titanium slag or their carefully blended mixture is soaked in highly concentrated sulphuric acid (80% - 95%) for several hours. On digestion with sulphuric acid the feedstock yields FeSO_4 and TiOSO_4 [Kolditz (1980), Gesenhues (2001), Heine et al. (2001)].



FeSO_4 and TiOSO_4 are dissolved in cold water. The resulting liquor contains Fe^{+3} ($\text{Fe}_2(\text{SO}_4)_3$)-undissolved and Fe^{+2} (FeSO_4)-dissolved. It is then passed through scrap iron to reduce Fe^{+3} to Fe^{+2} in order to dissolve iron completely [Gesenhues (2001), Heine et al. (2001)].

The liquor still contains the undissolved solids and sent to the clarifier tank. The undissolved solids settle in this step and are removed. The clarified liquor then undergoes vacuum crystallization. It removes the iron present in the liquor [Buxbaum and Pfaff (2005), Morimoto et al. (1969), Pervushin et al. (2002)]

The remaining TiOSO_4 is hydrolyzed by using steam to produce hydrated oxide of titanium $\text{TiO}(\text{OH})_2$. Very small extent of solid titanyl sulphate hydrate $\text{TiOSO}_4 \cdot \text{H}_2\text{O}$ also produces in this process [Omori et al., (1969)].



The hydrolysate contains 55% by weight of water. It is dewatered in the rotary drum filter and a cake is obtained which is sent to the rotary kiln for further calcination. During calcination the water and sulfates are removed and TiO_2 (anatase) undergo phase transition at 800-1000°C to produce TiO_2 (rutile) [Shannon and Pask (1965), Morimoto et al. (1972)].

3.6.2 Process model implementation

The calcination of the titanium dioxide rotary kiln is one of the most important stages in the processing of TiO_2 . This operation has two main purposes: Firstly, to dry a

slurry composed mainly of TiO_2 and water. Secondly, to transform the TiO_2 from anatase to rutile. The material which is fed to the rotary kiln for calcination through by the sulphate method has a chemical formula of $TiO_2 \cdot 0.064SO_3 \cdot 5.295H_2O$ [Ginsberg and Modigell (2011), Morimoto et al. (1972)]. Table 3-12 illustrates briefly the chemical reactions taking place during the calcination of the titanium oxide, temperature range and heat of reaction for each reaction. The moisture and adsorbed water are removed at about $500^\circ C$ [Sullivan and Cole (1959)]. The desulphurization occurs between 600 and $700^\circ C$ where sulphate groups are removed from the $TiOSO_4$. Finally the phase transition from anatase to rutile occurs at about 700 – $900^\circ C$ [Udupa (1982)].

Table 3-12: The chemical reactions that occur within the kiln [Ginsberg et al. (2010)].

Reaction	Chemical reaction	Temperature range	Heat of reaction $\Delta h_{0,i}$
Water evaporation	$H_2O_{liq} \rightarrow H_2O_{vap}$	$0-100^\circ C$	$2260 \text{ kJ/kg}_{H_2O}$
Desorption of water Dehydration	$TiO(OH)_2 \rightarrow TiO_2 + H_2O(g)$ 97.87g/mol 79.87g/mol 18g/mol	$100 - 500^\circ C$	$354 \text{ kJ/kg}_{TiO(OH)_2}$
Dehydration	$TiOSO_4 \cdot H_2O \rightarrow TiOSO_4 + H_2O(g)$ 177.97g/mol 159.95g/mol 18g/mol	$<500^\circ C$	$118 \text{ kJ/kg}_{TiOSO_4 \cdot H_2O}$
Desulphurisation	$TiOSO_4 \rightarrow TiO_2 + SO_2(g) + 1/2 O_2$ 159.95g/mol 79.87g/mol 64.1g/mol	$600- 700^\circ C$	$-34 \text{ kJ/kg}_{TiOSO_4}$
Rutilisation (Anatase to rutile)	$TiO_2(a) \rightarrow TiO_2(r)$ 79.8g/mol 79.8g/mol	$700-900^\circ C$	18 kJ/kg_{TiO_2}

Thermal decomposition reaction in solid state can be expressed by

$$\frac{dU_{s,i}}{dt} = k_i \cdot f(U), \quad (3-75)$$

where $\frac{dU_{s,i}}{dt}$ is the reaction rate, k_i is the reaction rate constant, $f(U)$ is the reaction model and U is the conversion fraction of the reaction. Rate constant is related to temperature by Arrhenius equation.

$$k_i = k_{A,i} \exp\left(\frac{-E_{a,i}}{R_{uin} \cdot T_s}\right) \quad (3-76)$$

where $k_{A,i}$ is the pre-exponential factor, $E_{a,i}$ is the activation energy of the specie i .

The function $f(U)$ is expressed frequently as:

$$f(U) = (1-U)^{n_i} \quad (3-77)$$

where n_i is the order of reaction and the subscript i represents $H_2O, TiO(OH)_2, TiOSO_4 \cdot H_2O, TiOSO_4, TiO_2$.

Table 3-13 describes the data on kinetics of the chemical reactions, taking place in the calcination stage.

Table (3-13): Kinetics parameters for calcination of TiO_2 reaction.

i	Reaction	$k_{A,i}$ (s^{-1})	$E_{a,i}$ (kJ/mol)	n_i	$\Delta h_{Ri,S}$ (kJ/mol)
1	$H_2O(l) \rightarrow H_2O(g)$	-	-	-	44±0.06 Schlunder et al. (1984)
2	$TiO(OH)_2 \rightarrow TiO_2 + H_2O(g)$	4.1×10^3	45±1.5	3.0	90±8.0 Przepiera et al. (2003)
3	$TiOSO_4 \cdot H_2O \rightarrow TiOSO_4 + H_2O(g)$	5.0×10^5	75±19	0.5	90±8.0 Udupa et al. (1982)
4	$TiOSO_4 \rightarrow TiO_2 + SO_2(g) + 1/2O_2$	5.0×10^9	230±12	0.3	396±173 Udupa et al. (1982)
5	$TiO_2(a) \rightarrow TiO_2(r)$	1.7×10^{23}	491±120	2/3	-5.6±0.8 Mackenzie et al. (1982)

The spatial conversion over the kiln length is given by the following equation:

$$\frac{dU_{S,i}}{dz} = \frac{dU_{S,i}}{dt} \cdot \frac{1}{v_p}, \quad (3-78)$$

Then the heat of reaction can be calculated according to the following equations:

$$\frac{dR_S}{dz} = \frac{dU_{S,i}}{dz} \cdot \dot{M}_S(z) \cdot x_{S,i} \cdot \Delta h_{u,i}. \quad (3-79)$$

Mass of the material under consideration changes due to the presence of chemical reactions (1-4) axially along the kiln and is described by

$$\dot{M}_S(z) = \dot{M}_{S,0} - \sum \dot{M}_{S,0} \cdot x_i \cdot U_{S,i}(z), \quad (3-80)$$

where $\dot{M}_{S,0}$ is the inlet mass flow rate of titanium kg/s

The mass change due to removal of H₂O (reactions 1-3), O₂ and SO₂ (reaction 4) to the gas phase are calculated as the following:

$$\dot{M}_{S,loss}(z) = \dot{M}_{S,0} \cdot x_{S,i} \cdot [1 - U_{S,i}(z)]. \quad (3-81)$$

3.7 Kaolin

3.7.1 Kaolin processing

Kaolin often called china clay is mineral clay mainly comprised of kaolinite (40-70%) [Moulin et al. (2001)]. Kaolinite is composed of layers of tetrahedral silica and octahedral alumina attached through oxygen. It consists of 46.54% SiO₂, 39.5% Al₂O₃ and 13.96% H₂O and is represented by a chemical formula of Al₂O₃·2SiO₂·2H₂O [Murrar (2000)]. Kaolinite clay occurs in abundance in soils which are formed from the chemical weathering of rocks in hot and moist climates. The world's production of kaolin have surpassed 25 million tonnes [Nkoumbou et al. (2009)] and its demand is estimated to grow 2.1 percent per year through 2020 [minerals.usgs.gov].

The properties of kaolin such as whiteness, softness, fine particle size and chemical inertness make it functional ingredient in various industrial applications. The paper

industry is the major user of kaolin where it is applied as coating pigment and filler. The whiteness, softness and better hiding power of kaolin makes the paper to be light in weight and enhances its printing characteristics. Kaolin is also used in ceramic industry to make the white ware where it provides white color to ceramic. It is also used in refractories as it has higher fusion point due to presence of significant amount of alumina. Kaolin is chemically inert and possess excellent dielectric properties which make it suitable to use in porcelain electric insulators [Murray and Kogel (2005)] Various other industries such as rubber, adhesives, paints etc. employ kaolin as a filler. Kaolin can induce and accelerate blood clotting its derivative- aluminosilicate has been successfully used as infusion in traditional gauze [Ptacek et al. (2011)].

The raw kaolin obtained here is either sent for dry refining or it is washed with high pressure water to separate stone and sand. The stones may be crushed to different grades and used in other industries. The removed sand is sent to building industry. Kaolin ore after mining is processed to achieve the product with desired properties through the different methods namely dry process, wet process and thermal process [Thurlow (2005)]. The products of dry or wet process can be marketed as such for their further use. However, if a higher grade product is desired, the dry or wet processed kaolin is subjected to thermal process. In thermal process a refined and dried material undergoes calcination. The wet process yields a more refined product as compared to the dry process and will be discussed here. The process steps involved wet process are shown in figure 3-16

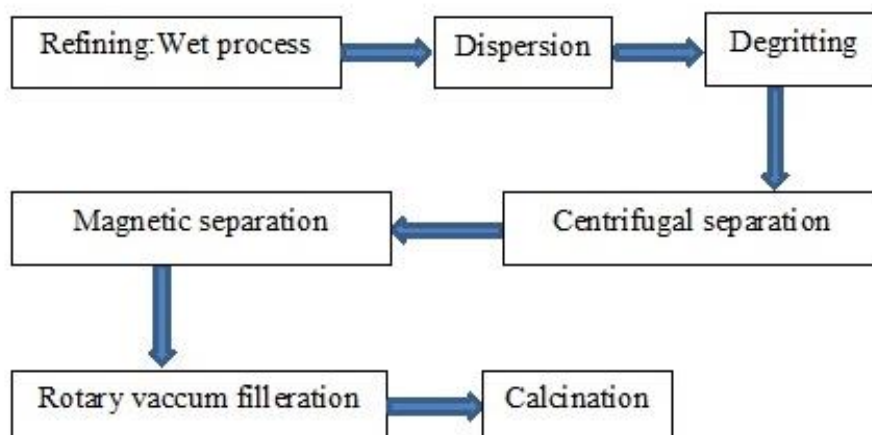


Figure 3-16: Process flow diagram of kaolin

In wet process, the mineral clay is dispersed in water along with a dispersant to obtain a mineral-water suspension. The suspension undergoes gritting where coarse impurities like sand and mica is separated from fine material using screens, hydrocyclone or hydroseparator. The degrittied suspension is sent to centrifuges where it is classified in various particle size fractions. The coarse fraction obtained here is sent to delamination or used to produce filler clays. During lamination, vermicular stacks and books of kaolin experience shearing which converts the stack or book into plates of high aspect ratio i.e. higher length to diameter ratio [Kraft et al. (1972)]. The fine fraction obtained here contain impurities like iron oxides, iron hydroxides, anatase, mica etc. which imparts the undesired color to the kaolin. It is passed through different beneficiation processes like magnetic separation, selective flocculation, froth flotation and leaching to remove these impurities so that the product with required brightness could be achieved. The refined clay is then sent to a drying plant where it is first thickened, dewatered and dried. The dried clay is milled and sold as such or goes through calcination to yield a higher grade product.

3.7.2 Process model implementation

Kaolin is heated to a temperature below its melting point during its calcination. It loses all its water in its structure and undergoes other physic-chemical changes. This process makes the kaolin chemically inert and enhances its pigmentary properties [Thurlow (2005) and Ptacek et al. (2010)]. During calcination of kaolin, it loses its free moisture followed by dehydroxylation reaction at 450-700 °C in which the chemically bound water is driven off. It loses 14% of mass with the removal of in bound hydroxylions and as a result, amorphous metakaolin is obtained. At further heating to temperature 925 to 1050 °C, metakaolin transforms to the 'spinel phase' [Moulin et al. (2001) and Kostuch et al. (1993)]. Kaolin begins to form mullite on heating above 1050 °C.[Thomas (2010)]. Table 3-14 explains the different reactions taking place during the calcination of kaolin, the corresponding temperature ranges and their heat of reactions:

Table 3-14: Reactions during calcination of kaolin

Reaction	Chemical reaction	Temperature range °C	Heat of reaction
Water evaporation	$H_2O_{liq} \rightarrow H_2O_{vap}$	0-100°C	2258.2 kJ/kg _{H₂O}
Dehydroxylation	$Al_2O_3 \cdot 2SiO_2 \cdot 2H_2O \rightarrow$ $Al_2O_3 \cdot 2SiO_2 + 2H_2O$	450 - 700°C	891 kJ/kg _{Al₂O₃·2SiO₂·2H₂O} [Petzold et al. (1985)]
Spinel formation	$2(Al_2O_3 \cdot 2SiO_2) \rightarrow$ $2Al_2O_3 \cdot 3SiO_2 + SiO_2$	925-1050°C	-212.9 kJ/kg _{2(Al₂O₃·2SiO₂)} [Mazumdar and Mukherjee (1983)]
Mullite formation	$3(Al_2O_3 \cdot 2SiO_2) \rightarrow$ $2(3Al_2O_3 \cdot 2SiO_2) + 5SiO_2$	>1050°C	1301.7 kJ/kg _{3(Al₂O₃·2SiO₂)} [Ptacek et al (2012)]

The reaction rate for each reaction component follows Equation :

$$\frac{dU_{s,i}}{dt} = k_i \cdot f(U), \quad (3-82)$$

where $\frac{dU_{s,i}}{dt}$ is the reaction rate, k_i is the reaction rate constant, $f(U)$ is the reaction model and U is the conversion fraction of the reaction. Rate constant is related to temperature by Arrhenius equation

$$k_i = k_{A,i} \exp\left(\frac{-E_{a,i}}{R_{uin} \cdot T_S}\right), \quad (3-83)$$

where $k_{A,i}$ is the pre-exponential factor, $E_{a,i}$ is the activation energy of the specie i.

The function f (U) is expressed frequently as:

$$f(U) = (1 - U)^{n_i}, \quad (3-84)$$

where n_i is the order of reaction, The subscript i is equal to H_2O , $Al_2O_3 \cdot 2SiO_2 \cdot 2H_2O$, $2(Al_2O_3 \cdot 2SiO_2)$, $3(Al_2O_3 \cdot 2SiO_2)$, TiO_2 respectively.

The values of these parameters are shown in table 3-15.

Table 3-15: Reaction parameters of reactions occurring kaolin calcination.

i	Process	$k_{A,i}$ (s^{-1})	$E_{a,i}$ (kJ/mol)
1	$H_2O(l) \rightarrow H_2O(g)$	5.0×10^7	61.0
2	$Al_2O_3 \cdot 2SiO_2 \cdot 2H_2O \rightarrow Al_2O_3 \cdot 2SiO_2 + 2H_2O(g)$ 258g/mol 222g/mol 36g/mol	1.0×10^7	145.0 [Ptacek et al. (2013)]
3	$2(Al_2O_3 \cdot 2SiO_2) \rightarrow 2Al_2O_3 \cdot 3SiO_2 + SiO_2$ 444g/mol 384g/mol 60g/mol	5.0×10^{33}	856.0 [Ptacek et al. (2012)]
4	$3(Al_2O_3 \cdot 2SiO_2) \rightarrow 2(3Al_2O_3 \cdot 2SiO_2) + 5SiO_2$ 1152g/mol 852g/mol 300g/mol	1.0×10^{17}	522.0 [Gualtieri et al. (1995)]

The spatial conversion over the kiln length and given by the heat of reaction:

$$\frac{dU_{S,i}}{dz} = \frac{dU_{S,i}}{dt} \cdot \frac{1}{v_p}, \quad (3-85)$$

$$\frac{dR_S}{dz} = \frac{dU_{S,i}}{dz} \cdot \dot{M}_S(z) \cdot x_{i,S} \cdot \Delta h_{u,i}, \quad (3-86)$$

with

$$\dot{M}_S(z) = \dot{M}_{S,0} - \sum \dot{M}_{S,0} \cdot x_i \cdot U_{S,i}(z), \quad (3-87)$$

where $\dot{M}_{S,0}$ is the inlet mass flow rate of kaolin

3.8 Aluminum dross

3.8.1 Aluminum dross processing

Aluminum dross is generally made up of aluminum oxides, sulfide of aluminum, nitride, carbide and salts [Samson (2014)]. It is considered as waste product obtained from the aluminum refinery. It is usually produced from the melting of aluminum scrap such as the used beverage cans. Dross is processed in rotary kilns to recover Aluminum [Kulik and Daley (1990), Peterson Newton (2002)]. Dross is classified to black or white dross which depends on the amount of the metal content. White (wet) dross has high metal, low oxides and low salt content while the black (dry) dross in contrast has low metal content and high amount of salt and oxides with granular-like form. It is also used as a cement additive to increase its stiffness and abrasion resistance and as refractory bricks and filler material in concrete production. It is also used in Al composites production where it gives superior wear resistance, steel slag additive where it changes the chemistry during the steel slag desulphurization [Carvalho (1991)].

Aluminium the abundant and cheap metal available in earth is consumed around 50k metric tonnes in a year contribute around 1% of global GDP and this consumption is increasing around 0.5% - 1% every year. Aluminum is the most widely used metal after iron. Global production of aluminum in 2005 was 31.9 million tonnes [Hetherington, L.E. (2007), en.wikipedia.org]. During production of aluminum from ore around 40% of pure aluminum is carried away in the dross. This dross contains additional elements such as magnesium, zinc etc. in it. Pure aluminum can be reclaimed from dross through many processes that involve chemical, physical and electric [rspublication.com] methods which are more economical than producing aluminum from its ore bauxite by Bayer process or Hall-Heroult process. Recovering this metal from dross can be used to meet the increase in the demand for the metal. By reclaiming aluminum from the dross industries can improve the production of aluminum with the dross they have, so that cost incurred in purchasing virgin metal to meet up the production quantity will be decreased.

Dross is recovered by treating it in the rotary slag furnace fired with oil or gas. The flow diagram of this process is shown in figure 3-17.

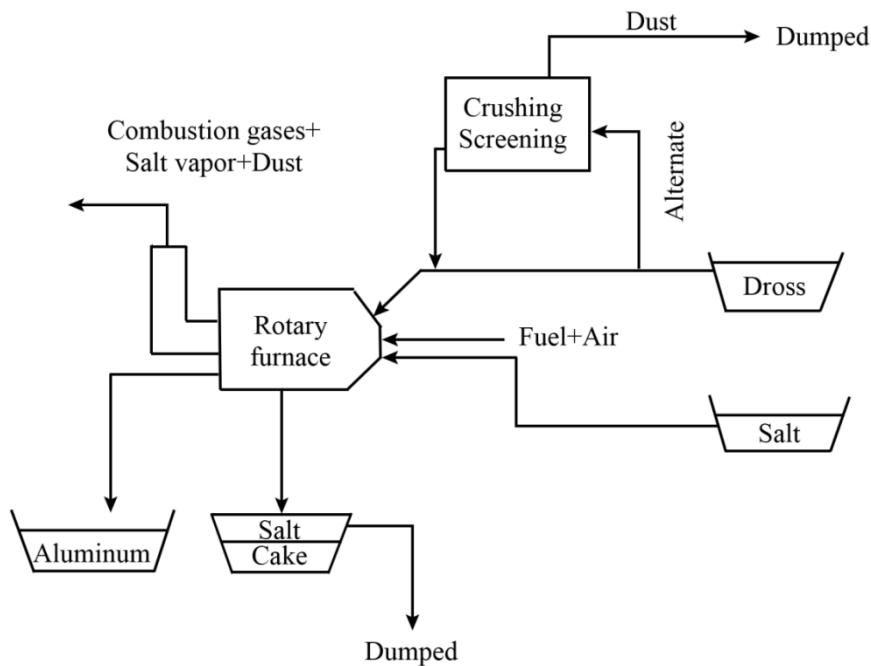
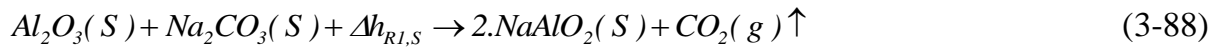


Figure 3-17: The rotary salt furnace process [Lavoie and Dube (1991)].

Dross is first pulverized into coarse powder and screened. The dust is removed here while the other fraction of dross is introduced in the kiln with the salt flux of around 50% of the dross weight. This salt does not only inhibit the formation of oxides of aluminum but also breaks down the already formed layers of aluminum thereby facilitating winning aluminum from the residues [rpublication.com]. The salt cake, formed as a result of this process is a mixture of aluminum oxides and aluminum nitrides, metal and salts. More than 1 ton of salt cake is produced for every ton of dross treated [Lavoie S, Dube G (1991)].

3.8.2 Process model implementation

The aluminum dross mixed with sodium carbonate undergo two chemical reactions calcination (endothermic) and oxidation (exothermic) take place simultaneously and are very crucial to the calcination process.



Endothermic reaction: $\Delta h_{R1,S} = + 1220$ kJ/mol



Exothermic reaction: $\Delta h_{R2,S} = - 1670$ kJ/mol

At a temperature range of 50-100 °C mass loss is observed due to the physical water and volatilization of organic substances, and then the main reaction takes place in the temperature range of 600-650 °C. The total mass loss (25 %) is the sum of mass loss due to organic substances and moist (2 %) and CO₂ release (23%) in the calcination reaction. The main exothermic reaction starts with a mass increase of around 13% in the range of 600 °C. Shrinking core model is used to model of the endothermic reaction (calcination reaction). The conversion degree of calcination can be calculated as a function of decomposition time t as

$$\frac{dU_{S,Calcination}}{dt} \cdot [R_\alpha] = 1, \quad (3-90)$$

$$\frac{dU_{S,Calcination}}{dt} \cdot [R_\beta + R_K \cdot f_2(U_S)] = 1, \quad (3-91)$$

and oxidation of aluminum dross can be calculated as the function of decomposition time

$$\frac{dU_{S,Oxidation}}{dt} = k_{Oxidation} \cdot f(U), \quad (3-92)$$

The equilibrium pressure for calcination and the reaction rate coefficient defined by

$$P_{eq,Calcination} = P_{max,Calcination} \cdot \exp\left(-\frac{\Delta h_{R,Calcination,S}}{R_{uni} \cdot T_S}\right) \quad (3-93)$$

$$k_{,Calcination} = k_{A,Calcination} \exp\left(\frac{-E_{a,Calcination}}{R_{uin} \cdot T_S}\right) \quad (3-94)$$

$$k_{,Oxidation} = k_{A,Oxidation} \exp\left(\frac{-E_{a,Oxidation}}{R_{uin} \cdot T_S}\right) \quad (3-95)$$

Then the spatial conversion over the kiln length can be given by the following equation respectively:

$$\frac{dU_{S,Calcination}}{dz} = \frac{dU_{S,Calcination}}{dt} \cdot \frac{1}{v_P}, \quad (3-96)$$

$$\frac{dU_{S,Oxidation}}{dz} = \frac{dU_{S,Oxidation}}{dt} \cdot \frac{1}{v_P}. \quad (3-97)$$

Then the heat of reaction can be calculated according to the following equation:

$$\frac{dR_S}{dz} = \left[\frac{dU_{S,Calcination}}{dz} \cdot \dot{M}_S(z) \cdot x_{CO_2,S} \cdot \Delta h_{u,CO_2} + \frac{dU_{S,Oxidation}}{dz} \cdot \dot{M}_S(z) \cdot x_{O_2,S} \cdot \Delta h_{u,O_2} \right]. \quad (3-98)$$

The values of parameters used in these equations are listed in table 3-16.

Table 3-16: Parameters and their typical values

Parameter	Calcination	Oxidation
Pre-exponent coefficient ($p_{max,i}$)	$7.0 \times 10^{12} \text{ bar}$	-
Proportion (x_i)	0.23 kgCO ₂ / kg	0.13 kgO ₂ / kg
Molar reaction enthalpy ($\Delta h_{Ri,S}$)	110 kJ/mol FeCO ₃	168 kJ/mol CaCO ₃
Arrhenius constant ($k_{A,i}$)	$5.0 \times 10^{-4} \text{ 1/s}$	$5 \times 10^5 \text{ 1/s}$
Activation energy ($E_{a,i}$)	-55 kJ/mol	-200 kJ/mol
Specific enthalpy ($\Delta h_{u,CO_2,i}$)	27700 kJ/kg CO ₂	-45800 kJ/kg O ₂

During the reaction of the aluminum dross the release of the CO₂ and O₂ gases varies along the kiln length. Hence, the mass of the material is subjected to mass change throughout the kiln, as shown by the following reaction.

$$\dot{M}_S(z) = \dot{M}_{S,0} - [\dot{M}_{S,0} \cdot x_{CO_2} \cdot U_{S,Calcination}(z) - \dot{M}_{S,0} \cdot x_{O_2} \cdot U_{S,Oxidation}(z)], \quad (3-99)$$

$$\dot{M}_{S,loss}(z) = \dot{M}_{S,0} \cdot x_{CO_2} \cdot [1 - U_{S,Calcination}(z)], \quad (3-100)$$

$$\dot{M}_{S,add}(z) = \dot{M}_{S,0} \cdot x_{O_2} \cdot [1 + U_{S,Oxidation}(z)], \quad (3-101)$$

where $\dot{M}_{S,0}$ is the inlet mass flow rate of aluminum dross kg/s, $\dot{M}_{S,loss}$ is the mass loss of CO₂ kg/s and $\dot{M}_{S,add}$ is the mass of oxygen added in kg/s.

3.9 Conclusion

Eight different thermal processes are discussed in this chapter in detail. The reaction mechanisms of these processes are presented in terms of conversion degrees by using various sub models, which were then implemented in the system of equations representing the overall process. The processes, their reaction mechanisms, heat of reaction and the sub models are listed in table 3-17.

Table 3-17: Overview of reaction mechanisms, heat of reaction, and employed models for thermal processes.

Material	Chemical reaction	Heat of reaction	Model
Cement	1. $CaCO_3 \rightarrow CaO + CO_2$	+1780 kJ/kg $CaCO_3$	Spang
	2. $2CaO + SiO_2 \rightarrow 2CaO \cdot SiO_2 (C_2S)$	-732 kJ/kg C_2S	
	3. $C_2S + CaO \rightarrow 3CaO \cdot SiO_2 (C_3S)$	+59 kJ/kg C_3S	
	4. $3CaO + Al_2O_3 \rightarrow 3CaO \cdot Al_2O_3 (C_3A)$	+25 kJ/kg C_3A	
	5. $4CaO + Al_2O_3 + Fe_2O_3 \rightarrow 4CaO \cdot Al_2O_3 \cdot Fe_2O_3 (C_4AF)$	-25 kJ/kg C_4AF	
Limestone	$CaCO_3 \rightarrow CaO + CO_2$	3820 kJ/kg CO_2	Shrinking core
Magnesite	$MgCO_3(S) \rightarrow MgO(S) + CO_2(g) \uparrow$	2645 kJ/ kg CO_2	Shrinking core
Dolomite	1. $CaCO_3 \cdot MgCO_3(S) \rightarrow MgO \cdot CaCO_3(S) + CO_2(g)$	2645 kJ/ kg CO_2	Shrinking core
	2. $MgO \cdot CaCO_3(S) \rightarrow MgO \cdot CaO(S) + CO_2(g)$	3820 kJ/kg CO_2	
Siderite	$FeCO_3(S) \rightarrow FeO(S) + CO_2(g) \uparrow$	1700 kJ/kg CO_2	Shrinking core
	$2FeO(S) + 1/2O_2(g) \rightarrow Fe_2O_3(S)$	-7000 kJ/kg O_2	Arrhenius
Titanium oxide	1. $TiO(OH)_2 \rightarrow TiO_2 + H_2O(g)$	354.75kJ/kg $TiO(OH)_2$	Ginsberg
	2. $TiOSO_4 \cdot H_2O \rightarrow TiOSO_4 + H_2O(g)$	118.25kJ/kg $TiOSO_4 \cdot H_2O$	
	3. $TiOSO_4 \rightarrow TiO_2 + SO_2(g) + 1/2O_2$	-34 kJ/kg $TiOSO_4$	
	4. $TiO_2(a) \rightarrow TiO_2(r)$	18 kJ/kg TiO_2	
Kaolin	1. $Al_2O_3 \cdot 2SiO_2 \cdot 2H_2O \rightarrow Al_2O_3 \cdot 2SiO_2 + 2H_2O$	891kJ/kg $Al_2O_3 \cdot 2SiO_2 \cdot 2H_2O$	Arrhenius
	2. $2(Al_2O_3 \cdot 2SiO_2) \rightarrow 2Al_2O_3 \cdot 3SiO_2 + SiO_2$	-212.9kJ/kg $2(Al_2O_3 \cdot 2SiO_2)$	
	3. $3(Al_2O_3 \cdot 2SiO_2) \rightarrow 2(3Al_2O_3 \cdot 2SiO_2) + 5SiO_2$	1301.7kJ/kg	
Aluminum dross	1. $Al_2O_3 + Na_2CO_3 \rightarrow 2NaAlO_2 + CO_2(g) \uparrow$	27700 kJ/kg CO_2	Shrinking core
	2. $4Al(S) + O_2(g) \rightarrow 2Al_2O_3(S)$	-45800 kJ/kg O_2	Arrhenius

4 Experiments in a pilot rotary kilns

4.1 Experimental setup and procedure

A semi-industrial kiln was used to perform thermal treatment tests for the selected material to validate the developed model. This kiln has a length of $L = 5$ m and an inner diameter of $D = 0.4$. The kiln was equipped with refractory material with thickness of 150 mm. It was fired directly with natural gas with a maximum power of 200 kW. A schematic the experimental setup used in this study is shown in figure 4-1.

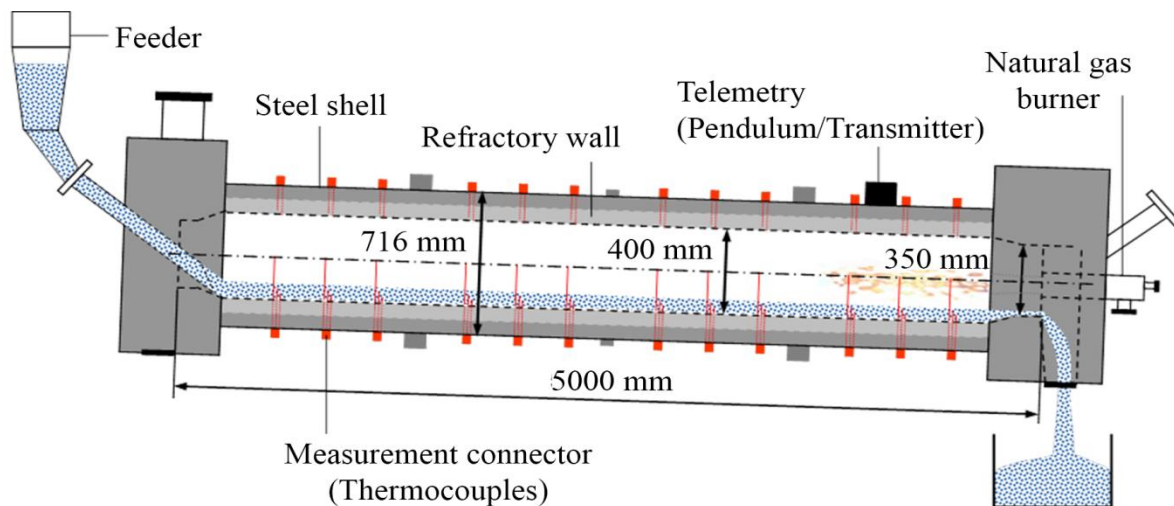


Figure 4-1: Schematic diagram of experimental setup

Various measurement connections are designed at different axial positions inside the kiln to detect the temperatures. Thermocouples of Type K (NiCr-Ni) with a diameter of 1 mm were installed at these measurement connections. The measurement principle is shown in Figure 4-2. Thermocouples were placed at the radial distances of 200 mm (gas), 42 mm, 22 mm and 5 mm to the wall as shown at the right side of figure 4-2. Thermocouples

were installed on the surface and at a depth of 5 mm into the inner wall at the opposite side. The thermocouple, positioned in the gas phase (200 mm) was protected against the radiation influence of the inner wall and the solid bed by a shield tube. The axial positions of the cross section with distributed thermocouples are shown on the left side of figure 4-2. The product temperature at the outlet of the kiln at $z = 5$ m and flue gas temperature at the inlet of the kiln at $z = 0$ m were also measured. The temperature was measured and its values were recorded as a function of time. These values were then transmitted to a measurement PC through a wireless connection. This PC has a software to record this data. Moreover, temperatures were assigned with a circumferential position through a pendulum, installed at the data transmitter. Thus, a radial, circumferential and axial temperature profile could be measured simultaneously. Additionally, a pyrometer was used to measure the temperature of the outer shell at different axial positions.

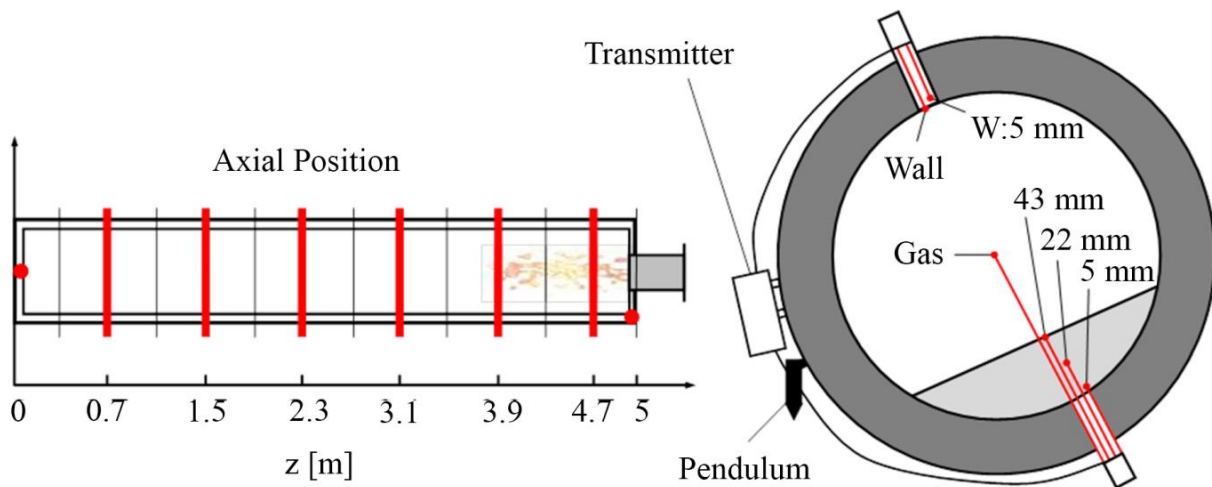


Figure 4-2: Measurement principle in the pilot rotary kiln

To start with the experimental series, the desired parameters like rotational speed and inclination angle of the kiln were selected. Then the kiln was heated for 3 hours, followed by the introduction of the material at a desired rate. The steady state mass throughput is achieved in 1 hour, while the thermal steady state was achieved after duration of 8 to 12 hours depending upon the experimental conditions. The measurements are recorded at the steady state and the supply of bulk material and fuel was stopped. The rotary

kiln was kept on rotating for another 10 hours in order to cool down slowly as the fast cooling may deform the kiln due to thermal stresses. Thus, 18 to 22 hours were needed to accomplish each series of experiments.

The kiln was operated at constant energy of 80 kW and an air excess number of 3.15. The excess air number was predicted from the exhaust gas measurements and included the possible false air which might have entered the kiln through gaskets. An excess air number of 2.5 was predicted from the measurements of the supplied air. Thus, false air amounted to approximately 20 % of the total air volume supplied to the kiln. The peripheral temperature inside the kiln at a cross sectional position of 3.1 m and at a time $t_{exp} = 11$ hours and 32 minutes is shown in the figure 4-3.

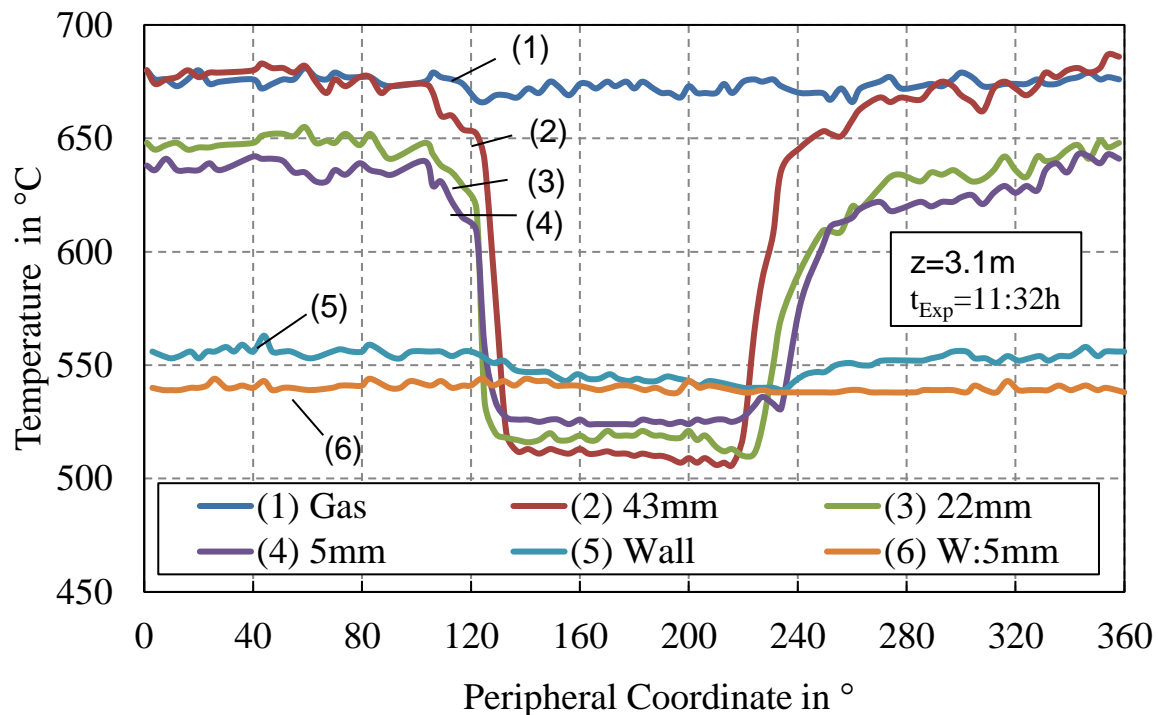


Figure 4-3: Peripheral temperatures in the interior of the rotary kiln
($z = 3.1$ m, $T_{exp} = 11$ h 32 min).

The figure shows the temperature of the gas and the wall along the peripheral coordinate remains nearly constant with a maximum temperature difference of 20 °C. The other thermocouples which are in direct contact with the bulk bed show a nearly constant

temperature till the peripheral angle of around 120° and decreases sharply at this position. The temperature again increases after an angle of 220° . These thermocouples show a temperature which is 50°C below than that measured by the stationary thermocouples in the gas phase. This could be due to the fact that they are not covered by a protective tube and are thus subject to the influence of the radiation on the "cooler" wall and bulk material surfaces and as well as the gas flow is not homogeneously distributed in the cross-section of the tube.

In order to define the temperatures at the axial positions, the temperatures of the gas phase and the inner wall recorded over the cross-section are arithmetically averaged, while the average cross-sectional temperatures of the bulk bed are determined. The averaged temperatures at the axial position of 3.1 m over the duration of the experiment is shown in figure 4-4.

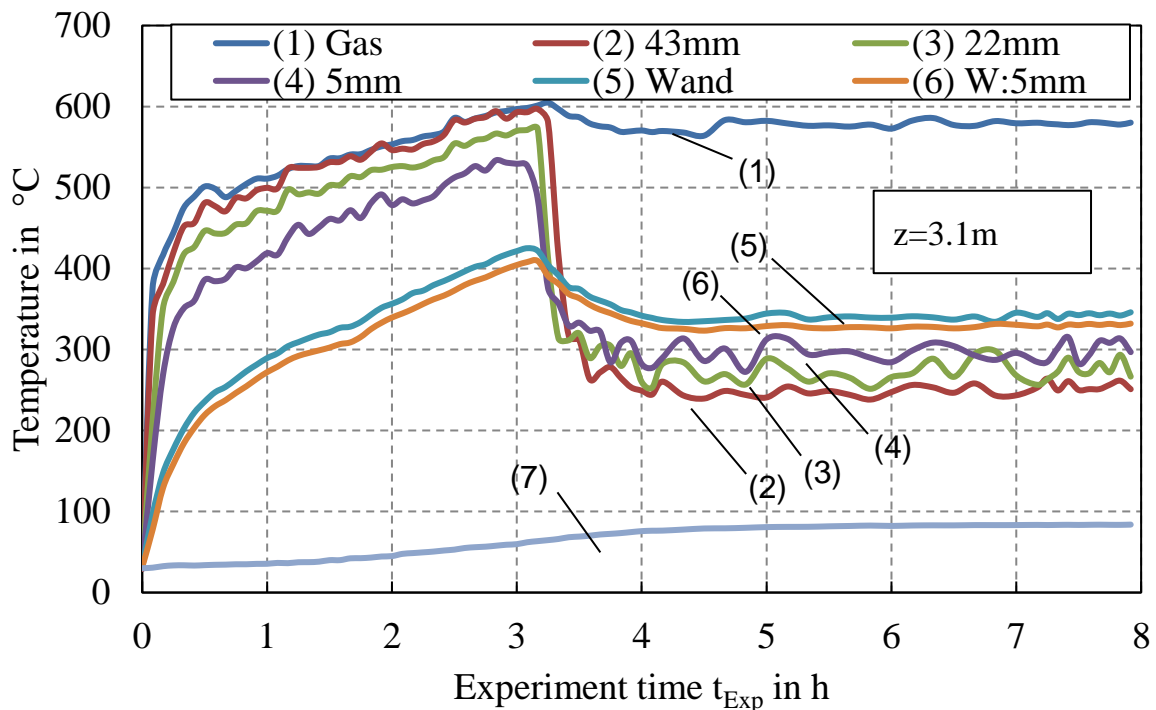


Figure 4-4: Average temperature range of a function of operating time.

The gas and inner wall temperatures increase during the heating phase to the maximum value and then decrease to a nearly constant value due to the heat transfer to bulk solids

($t = 3$ hours). The temperature of the kiln shell increase from 6-90 minutes due to the conduction from the wall to the shell of the kiln. After 5 hours of operation, it achieves a constant value and a steady state is achieved. After the steady state is achieved, the values of temperature recorded at each axial location till the end of the experiment are averaged and the axial profiles of temperatures are compared with the results obtained from developed model.

4.2 Aluminum dross

Test materials including Al_2O_3 : Na_2CO_3 in a ratio of 1:1.25 and 3% limestone were mixed together before entering semi-industrial kiln for thermal treatment as shown in figure 4-1.

The axial profile of filling degree of the bulk material through the kiln is shown in figure 4-5. The material enters the kiln with filling degree of $F_{z=0} = 11\%$ and increases due to the simultaneous reactions of oxidation and calcination and reaches filling degree of $F_{z=3} = 15.8\%$. The filling degree starts to decline sharply and the material undergoing the rotational motion leaves the kiln with $F_{z=L} = 2\%$.

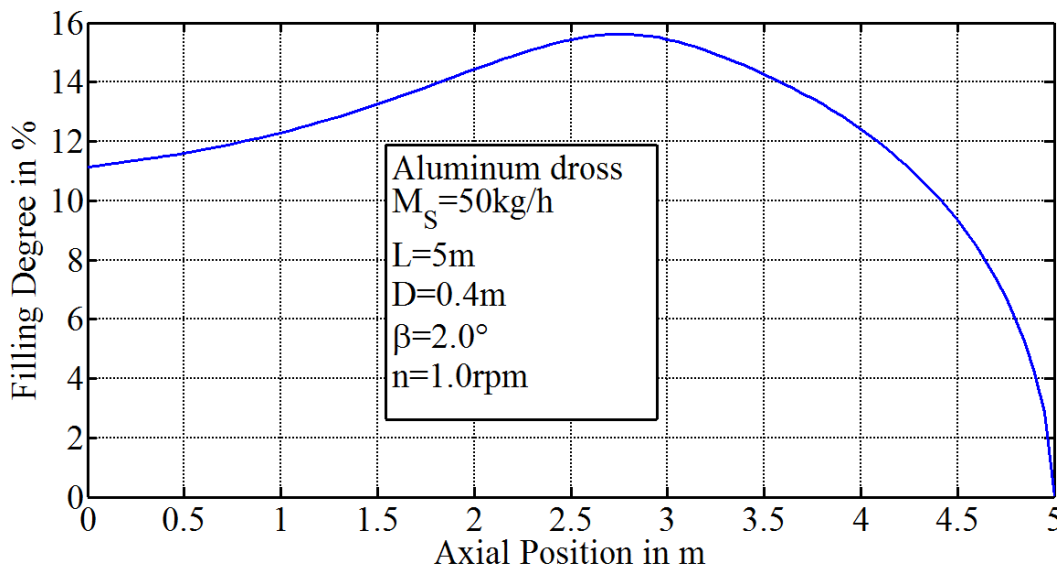


Figure 4-5: The axial filling degree profile for aluminum dross decomposition in the pilot rotary kiln ($L = 5$ m, $D = 0.4$ m).

The axial profile of the temperature of the solid bed, the gases, the inner wall and the shell, in addition to the axial profile of the conversion degree inside the kiln are shown in figure 4-6 and 4-7.

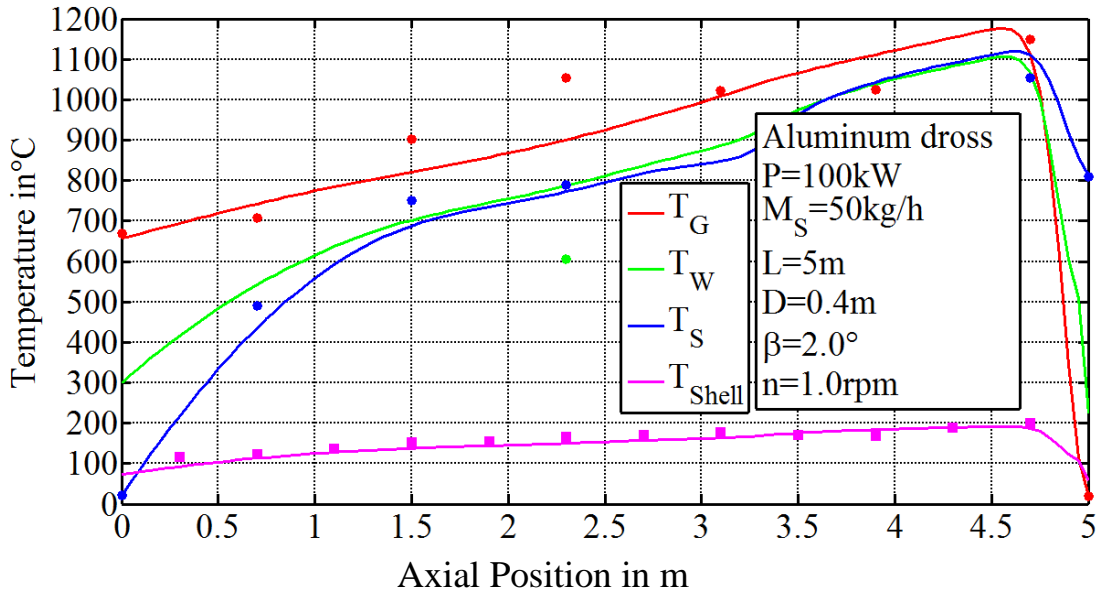


Figure 4-6: Axial temperature profiles for aluminum dross decomposition in the pilot rotary kiln (L = 5 m, D = 0.4 m).

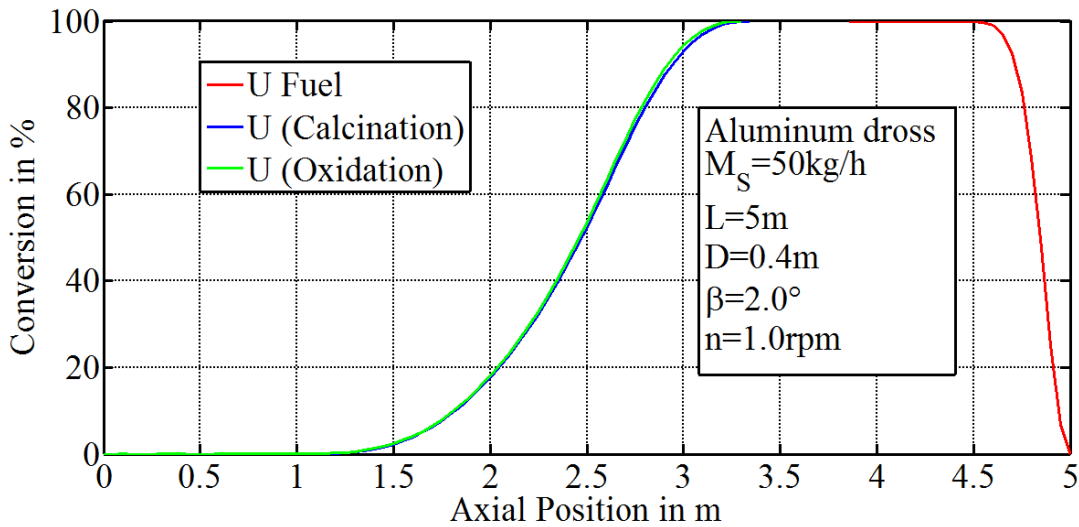


Figure 4-7: The axial conversion profiles for aluminum dross decomposition in the pilot rotary kiln (L = 5 m, D = 0.4 m).

The bulk material enters the kiln without any pre-calcination where $U_{S,0} = 0\%$ with temperature of $T_{S,0} = 20\text{ }^{\circ}\text{C}$. The material is exposed to the hot gases and its temperature increases as shown in figure 4-6 but without any noticeable conversion of the material. The temperature of bulk bed exceeds the temperature of the calcination at $z = 1.5\text{ m}$ where the calcination and the oxidation start simultaneously with the temperature of the bulk of $T_{S,1.5} = 600\text{ }^{\circ}\text{C}$. As these reactions take place simultaneously and due to the contradicting nature of both e.g. oxidation is exothermic and calcination is endothermic, and the enthalpy of the oxidation reaction $\Delta h = -1670\text{ kJ/mol}$ being greater than the enthalpy of calcination $\Delta h = 1220\text{ kJ/mol}$, the temperature of the bulk material continues to increase. At $z = 3\text{ m}$ both reaction accomplish and the temperature of the material starts to decrease and later on approaching to the flame zone, the temperature of the bulk bed increases again and reaches the maximum temperature of $T_{S,\text{max}} = 1119\text{ }^{\circ}\text{C}$. It starts decreasing due to the heat transfer with the incoming gases and the material leaves the kiln with $T_{S,L} = 788\text{ }^{\circ}\text{C}$.

The gases enters the kiln with $T_{G,L} = 20\text{ }^{\circ}\text{C}$ and exchange heat with the outgoing solid. Consequently, the temperature of the gases rises and reaches the maximum at the flame zone with temperature of $T_{G,\text{max}} = 1175\text{ }^{\circ}\text{C}$. It decreases linearly due to the continuous heat transfer with the bulk material and wall and the gases leave the kiln with temperature of $T_{G,0} = 656\text{ }^{\circ}\text{C}$.

The results obtained from simulations show a good agreement with the experimental results with a deviation of below 15%. More deviation is observed in the inner wall temperature. This could be due to the conduction through the caking layer at the wall. The data of input parameters for the aluminium dross in a semi-industrial kiln is presented in appendix (A.1). The data on temperature of the flue gas, product, bulk bed, heat loss, and residence time and product quality is presented in appendix (A.2).

4.3 Siderite

Calcination of the siderite was performed in semi-industrial kiln as mentioned in section 4.2. Kiln parameters used during the calcination of siderite are shown in Appendix (B.1).

Axial profile of temperature of gas, solid bed, inner wall and the outer shell are calculated using the developed model. The calculated results are also compared with the experimental results. The developed model is also used to calculate the axial profile of the filling degree and chemical conversion. Figure 4-8 illustrates the axial profile of the filling degree.

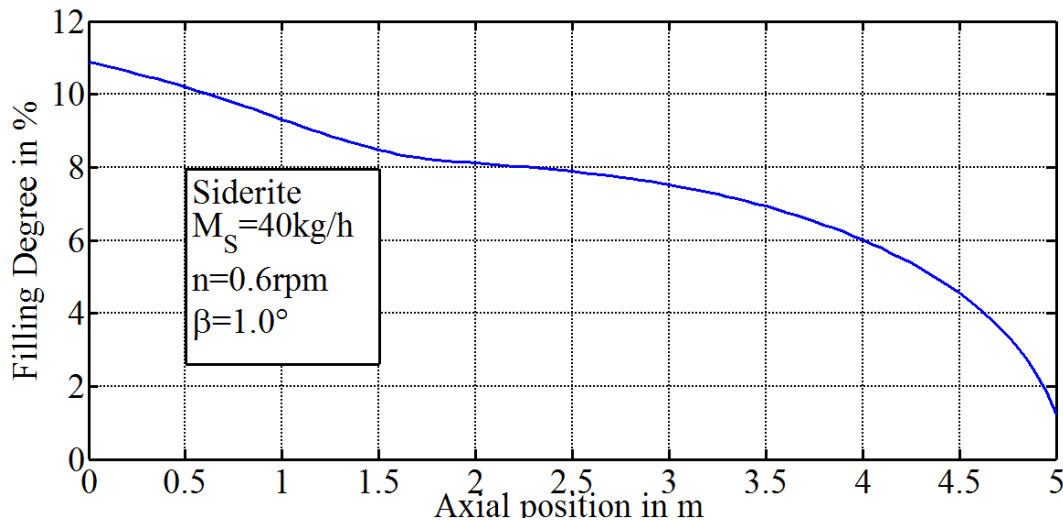


Figure 4-8: The axial filling degree profile for siderite decomposition in the pilot rotary kiln ($L = 5$ m, $D = 0.4$ m).

The filling degree of the bulk material at the entrance is $F_{z=0} = 11\%$ as shown in figure 4 - 8 and decreases linearly to $F_{z=2} = 8\%$ till $z = 2$ m where the calcination reaction completes. Then a smooth decrease in filling degree is seen due to the oxidation reaction. At $z = 4$ m, the oxidation reaction accomplishes and the filling degree is found to be $F_{z=4} = 6\%$. It decreases sharply thereafter and material leaves the kiln with $F_{z=L} = 1\%$.

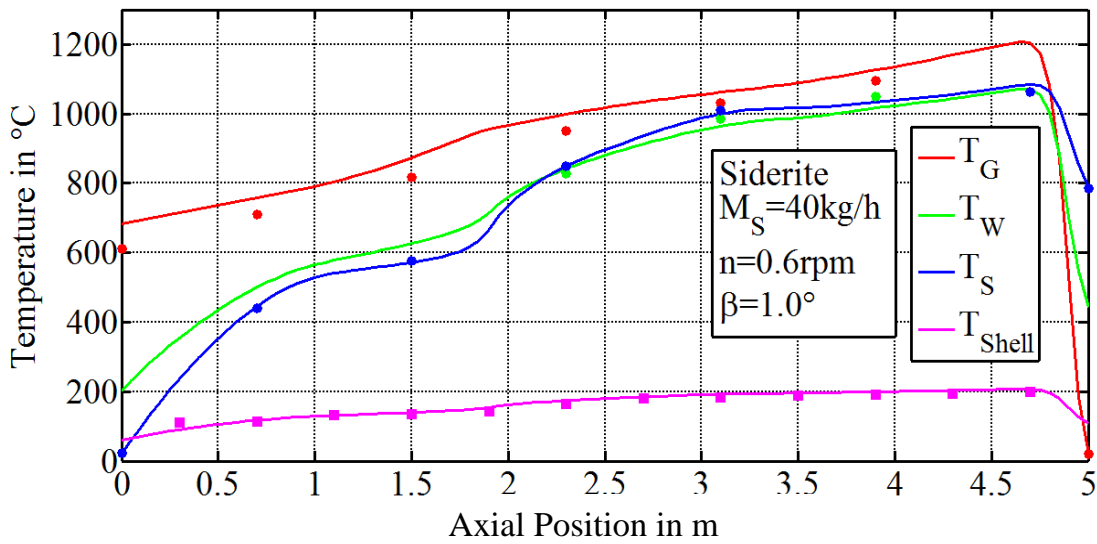


Figure 4-9: Axial temperature profiles for siderite decomposition in the pilot rotary kiln (L = 5 m, D = 0.4 m).

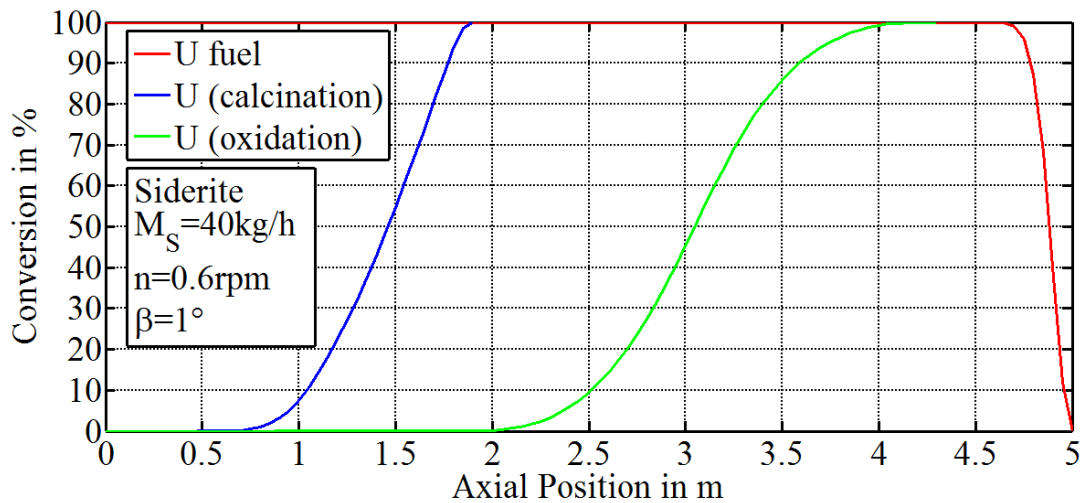


Figure 4-10: The axial conversion profiles for siderite decomposition in the pilot rotary kiln (L = 5 m, D = 0.4 m).

The axial profile of the temperature of the bulk bed, gas, the inner surface and the outer shell in addition to the axial profile of the conversion degree are depicted in figure 4-9 and 4-10 respectively. The bulk material enters the kiln with $T_{S,0} = 20\text{ }^{\circ}\text{C}$ with no conversion due to the low temperature ($U_{S,0} = 0\%$) of the material. The temperature of the material increases sharply due to the heat transfer between the combustion gases. At $z = 0.75\text{ m}$, the temperature reaches $580\text{ }^{\circ}\text{C}$. At this temperature, the calcination reaction starts and temperature increases at a lower rate as the larger part of heat is consumed in deriving the endothermic calcination. The oxidation reaction with its exothermic nature followed the calcination reaction and at $z = 2\text{ m}$ and the temperature of the material increases due to the oxidation and the heat transfer to the bulk bed till $T_{S,z=4} = 1050\text{ }^{\circ}\text{C}$. At this point the reaction accomplishes, it increases slowly to $T_{S,\text{max}} = 1090\text{ }^{\circ}\text{C}$. It then decreases due to the heat transfer with the wall and the incoming gases and the material leaves the kiln with $T_{S,L} = 800\text{ }^{\circ}\text{C}$. In contrary, the gases enter the kiln with $T_{G,L} = 20\text{ }^{\circ}\text{C}$ and then are heated up by the outgoing material in the cooling zone until it reached the maximum temperature at the flame zone which was $T_{G,\text{max}} = 1200\text{ }^{\circ}\text{C}$. The axial temperature of the gases declines till $z = 2\text{ m}$ where the calcination reaction accomplishes and decreases steeply due to the increase in the heat transfer from the gases to the bulk material. The gases leave the kiln with $T_{G,0} = 680\text{ }^{\circ}\text{C}$. The results obtained from developed model show good agreement with the experimental results with mean deviation of below 10 %. The data on temperature of the flue gas, product, bulk bed, heat loss, and residence time and product quality is presented in appendix (B.2).

5 Experiments in industrial rotary kiln based on literature data

5.1 Magnesite

5.1.1 Kiln and process parameters

The rotary kiln used in magnesite production is depicted schematically in figure 5-1. The kiln has a length of $L = 90$ m, an outer diameter of $D_{\text{shell}} = 3.76$ m, and an internal diameter of $D = 3.04$ m. The kiln shell is shielded from the thermal load inside the kiln with refractory bricks. Two layers of refractory bricks are placed inside the kiln. The first layer has a thickness of $s_{w,1} = 75$ mm and the second layer has a thickness of $s_{w,2} = 104$ mm. The ratio of the length and the diameter (L/D) is 24. The kiln is inclined with $\beta = 1^\circ$ and the rotational speed is $n = 1$ rpm. It was operated with a power of $P = 18.5$ MW using coal as fuel in the kiln. The fuel and air with excess air number of $\lambda = 1.06$ produced a premixed flame with flame length of $L_{\text{Flame}} = 20$ m. Magnesite was fed with mass flow rate $\dot{M}_{S,z=0} = 25$ t/h and. At the outlet of the kiln product is withdrawn at a rate of $\dot{M}_{S,z=L} = 12$ t/h. The raw material was preheated before entering the kiln till the temperature of the solid reached $T_{S,0} = 420$ °C. The material have undergone calcination during the preheating process and the conversion degree was found to be 2 %. An overview of the technical data is provided in appendix (C.1).

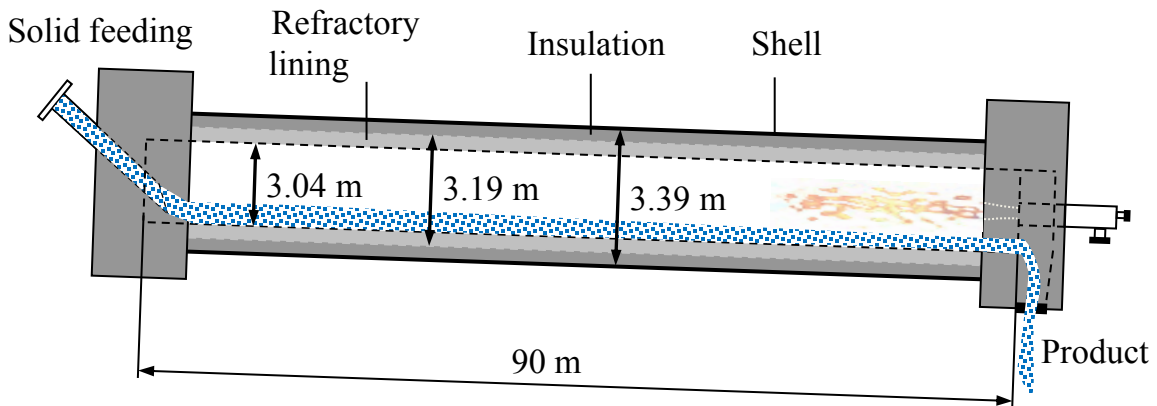


Figure 5.1: Schematic diagram of the rotary kiln for magnesite calcination.

5.1.2 Results and validations

The axial profile of the filling degree with the spatial coordinates is shown in figure 5-2.

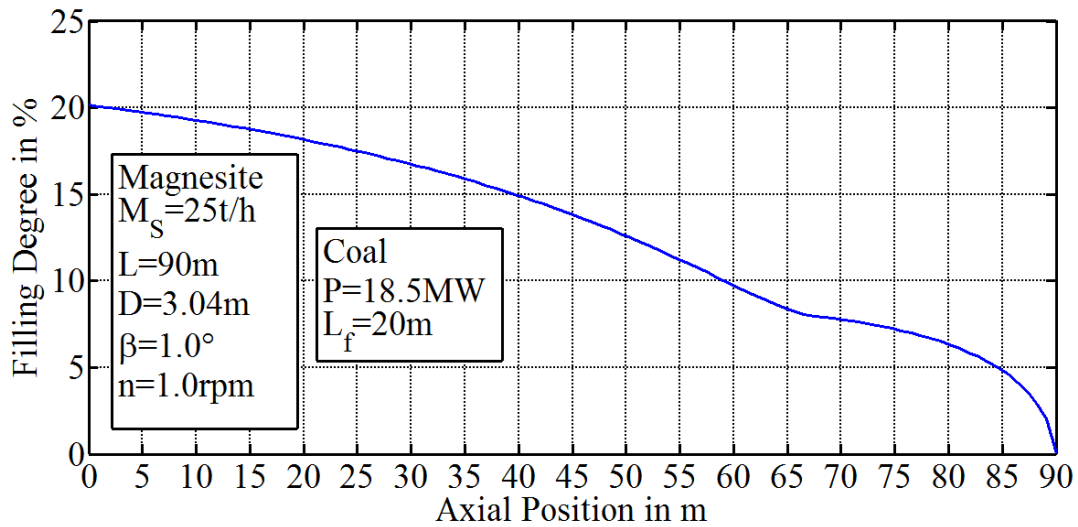


Figure 5-2: The axial filling degree profile for magnesite decomposition in a rotary kiln ($L = 90\text{ m}$, $D = 3.04\text{ m}$).

At the entrance of the kiln $z = 0$ m, the filling degree is almost $F_{z=0} = 20.15$ %. The filling degree of the kiln shows a liner decrease due to the gravitational force and the release of CO_2 which comes from the chemical reaction. The filling degree reached the value of 8 % at $z = 67.6$, and then starts to decrease and reaches the value of 0.02 % at $z = 90$ m.

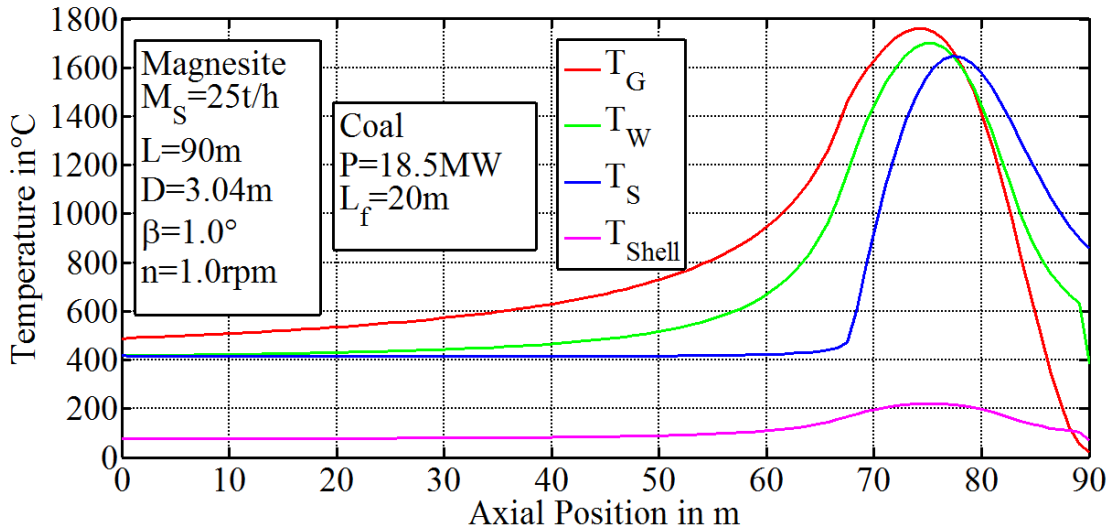


Figure 5-3: Axial temperature profiles for magnesite decomposition in a rotary kiln
($L = 90$ m, $D = 3.04$ m).

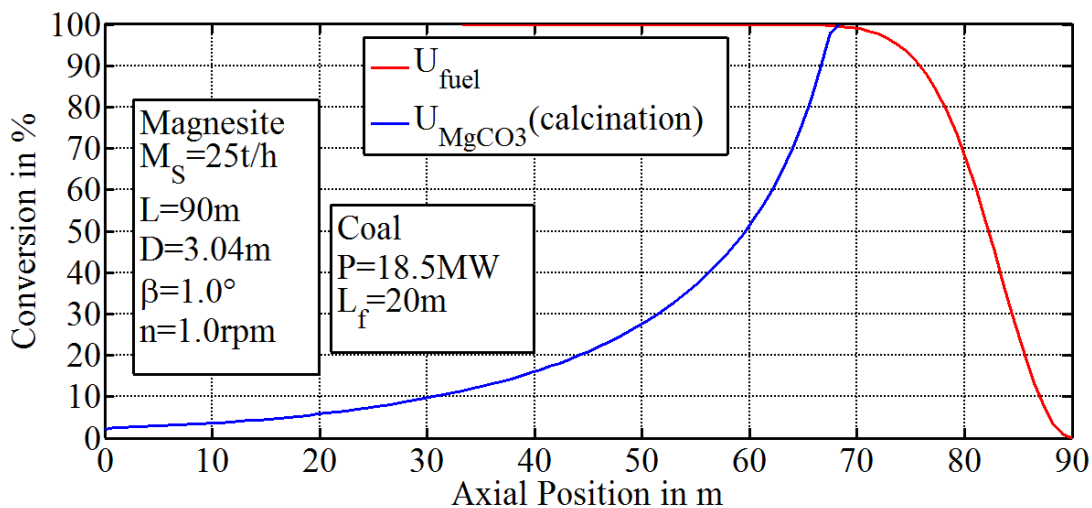


Figure 5-4: The axial conversion profiles for magnesite decomposition in a rotary kiln
($L = 90$ m, $D = 3.04$ m).

The results of the simulation for the axial profile of the bulk bed, gas phase, the inner wall surface and the outer shell as well as conversion degree of both fuel and magnesite are shown in figure 5-3 and 5-4. The solid material enters to the kiln with temperature of $T_{S,0} = 420$ °C. At this temperature, magnesite calcines with conversion degree $U_{S,0} = 2$ % as shown in figure 5-4. The axial temperature profile of the bulk bed shows negligible change in the temperature till $z = 64.8$ m as can be seen from figure 5-3 due to the endothermic calcination reaction of magnesite. As shown in figure 5-4, the calcination reaction is completed at $z = 67$ m. Hence temperature profile of the bulk solid shows sharp increase as the supplied heat is used to heat up the material which attains maximum temperature of $T_{S,max} = 1876$ °C. The temperature of the bulk bed decreases after reaching the maximum temperature as it loses the heat to the wall and the gas and the exit temperature of the bulk bed is found to be $T_{S,L} = 787$ °C. On the other hand, the gas temperature increase due to the fuel conversion until the end of the flame where temperature of the gas reaches $T_{G,max} = 1914$ °C at $z = 73$ m. The axial profile of the gas temperature between $z = 73$ m and $z = 64.8$ m shows steep decrease as in this region bulk bed possesses low temperature which increases the heat transfer rate between gas and solid. The gas leaves the kiln with temperature of $T_{G,0} = 471$ °C.

As shown in figure 5-5 with solid lines, Magnesite contains 52 % of CO_2 by mass and the rest of magnesite is MgO. Magnesite have lost 2 % of CO_2 due to its calcination in the preheating zone before entering the kiln. The loss of CO_2 increases as magnesite undergo further calcination in kiln. The total mass of the magnesite decreases but the content of the MgO increases till it reaches 98 %. The validation of the results of the simulation is carried out by comparing the results from the literature (points shown in figure 5-5) [Ludera (1974)].

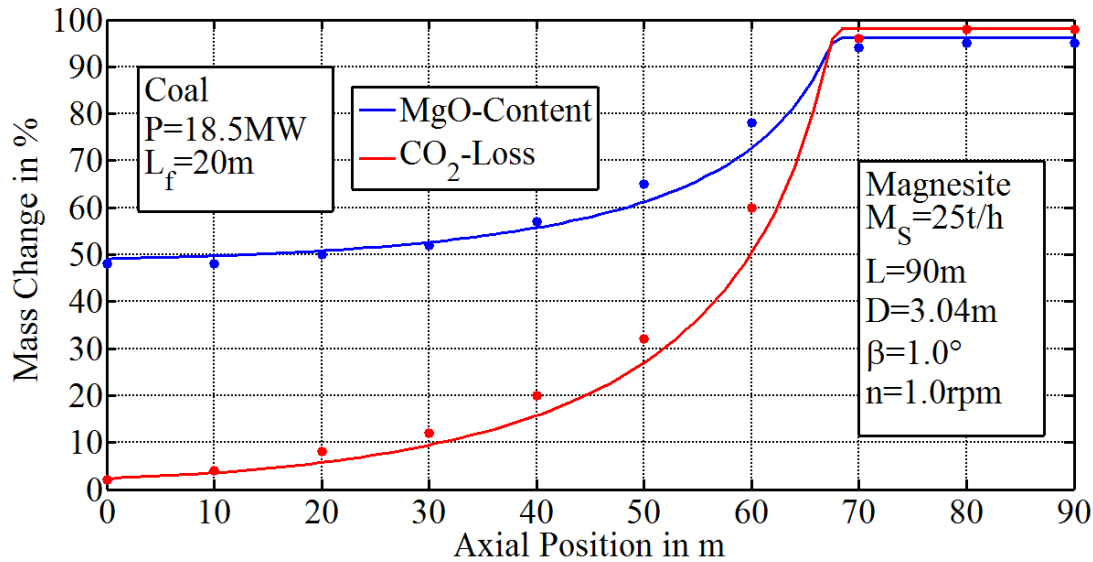


Figure 5-5: The chemical composition profiles for magnesite decomposition in a rotary kiln ($L = 90$ m, $D = 3.04$ m).

The comparison of simulation and literature from mass change of CO_2 and MgO content show very good agreement with a maximum deviation below 10%. The data on maximum bulk bed and gas temperature as well as the flue gas temperature, the wall heat loss, residence time and product quality are summarized in appendix (C.2).

5.2 Dolomite

5.2.1 Kiln and process parameters

The schematic diagram of the rotary kiln used for the calcination of dolomite is shown in figure 5-6. This kiln has a length of $L = 119$ m and an outer diameter of $D_{\text{shell}} = 3.5$ m.

It is constructed with double refractory layers i.e. first layer with thickness of 140 mm, while the second with a thickness of 185 mm in order to protect the shell from the thermal damage and to reduce heat loss to the environment. The kiln is inclined with a inclination angle of $\beta = 2.0^\circ$ and operates with a rotational speed of $n = 1$ rpm. A premixed flame burner with a power of $P = 40.5$ MW was used with an air excess number of $\lambda = 1.3$ and a flame length of $L_{\text{Flame}} = 18$ m. Dolomite entered the kiln with at a rate of $\dot{M}_{S,z=0} = 40.7$ t/h

with a particle size of $d_p = 25$ mm. Due to the mass loss during calcination output mass flow of the product is $\dot{M}_{S,z=L} = 23.6$ t/h. Technical data is reported in appendix (D.1).

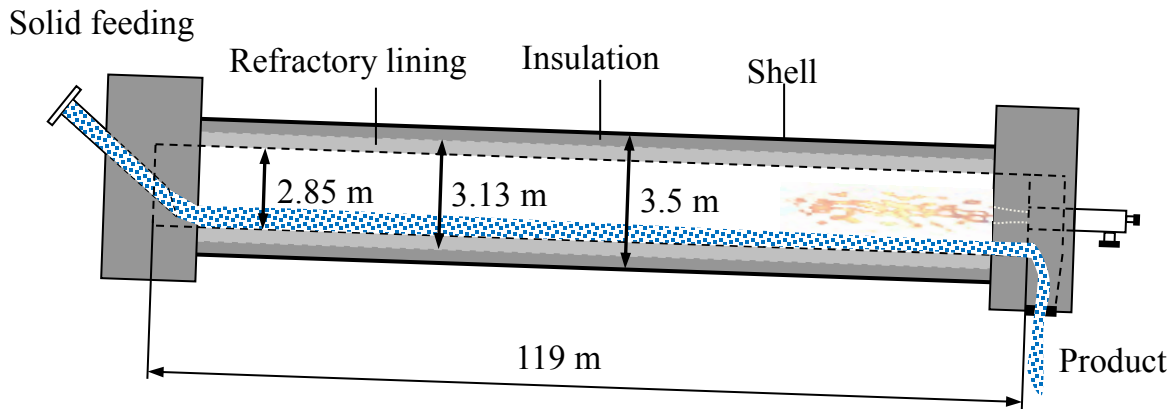


Figure 5-6: simplified sketch of kiln outline used in dolomite production.

5.2.2 Results and validation

The variation of filling degree with the axial length is illustrated in the figure 5-7.

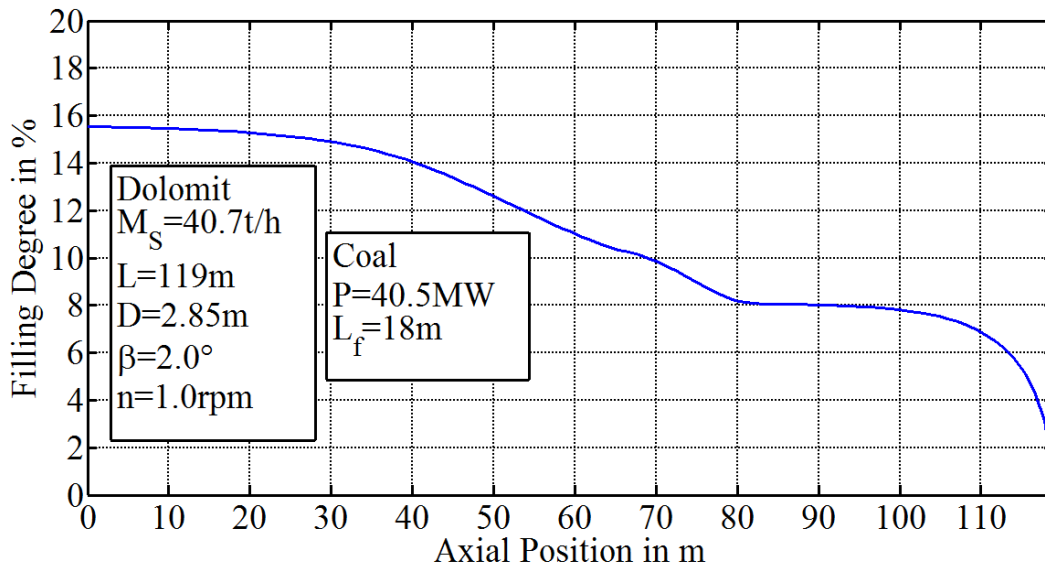


Figure 5-7: The axial filling degree profile for dolomite decomposition in a rotary kiln ($L = 119$ m, $D = 2.85$ m).

Filling degree at the kiln inlet ($z = 0$ m) is 15.5 % and decrease slightly from $z = 0$ m till $z = 40$ m. This is due to the absence of any chemical reaction in this region and the

material is just dried and heated up here. Thereafter, it shows a significant decrease till $z = 68$ m, where the calcination of the magnesite takes place. The calcination of limestone starts at $z = 70$ m and the filling degree decreases with a relatively greater slope and attains a value of 8 % at $z = 80$ m. The filling degree keeps on decreasing till end of the kiln ($F_L = 1$ %).

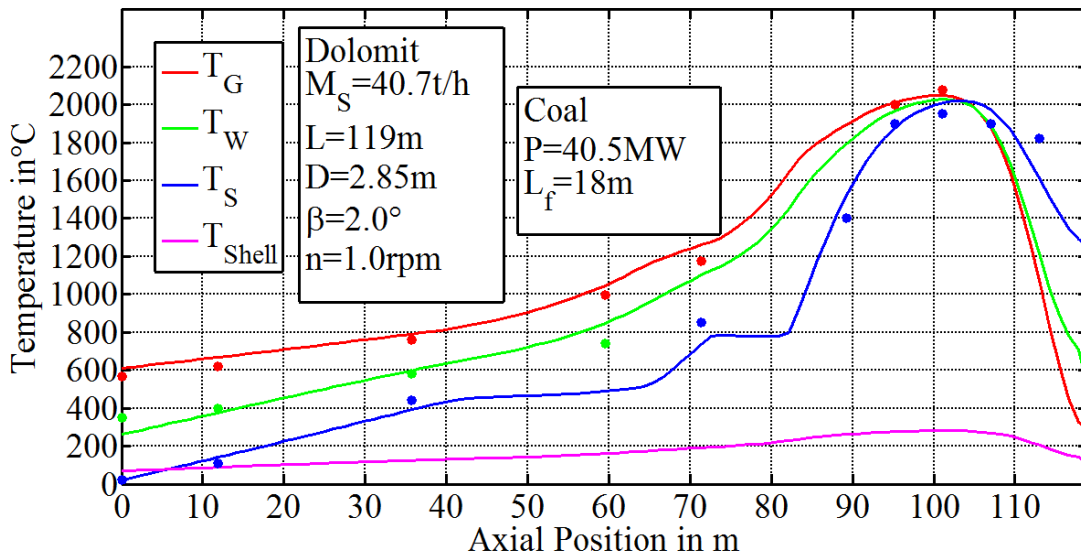


Figure 5-8: Axial temperature profiles for dolomite decomposition in a rotary kiln ($L = 119$ m, $D = 2.85$ m).

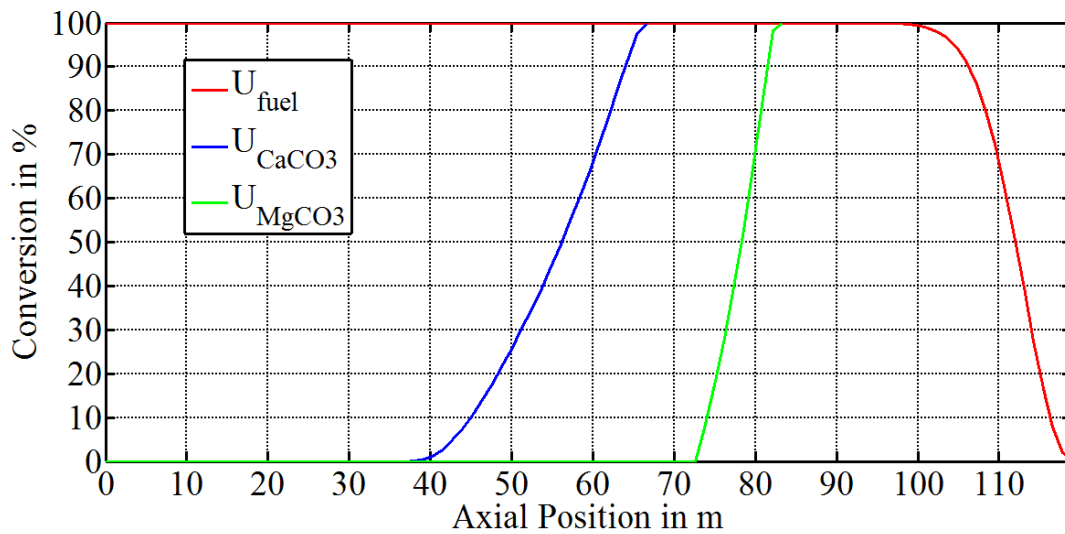


Figure 5-9: The axial conversion profiles for dolomite decomposition in a rotary kiln ($L = 119$ m, $D = 2.85$ m).

The results for the axial temperature profile of the bulk bed T_S , the gas T_G , inner wall surface T_W and the outer shell surface T_{Shell} , as well as the conversion degree of the dolomite are shown in figure 5-8 and 5-9. The air enters the kiln with $22\text{ }^\circ\text{C}$ and excess air number $\lambda = 1.3$. The combustion of the coal provides the necessary thermal energy for reaction and the gas reaches the peak temperature of $T_{G,max} = 2049\text{ }^\circ\text{C}$. Subsequently, the temperature of the combustion gases decreases due to the heat transfer to the solid bed and to the wall. The gas leaves the kiln with $T_{G,0} = 611\text{ }^\circ\text{C}$. On the other hand, the feed material enters with $T_{S,0} = 20\text{ }^\circ\text{C}$ and it is heated up due to the heat transfer between the gas, wall and the material. The temperature of the solid shows linear increase till $z = 40\text{ m}$, where the temperature reaches to $450\text{ }^\circ\text{C}$. At this point, the calcination of the magnesite starts and the supplied heat is consumed in deriving the reaction due to the endothermic reaction. Consequently, the temperature of the material shows slight increase till $z = 68\text{ m}$ and temperature of solid at this point is around $500\text{ }^\circ\text{C}$. On the completion of the calcination reaction of the magnesite, the temperature of the material shows sharp increase ($T_S = 780\text{ }^\circ\text{C}$ at $z = 72\text{ m}$). After that the temperature of the material does not change noticeably around the above mentioned value, as the calcination of the limestone ends an around $z = 82\text{ m}$. After complete calcination (both magnesite and limestone), temperature of the calcined dolomite increases to sintering temperature ($1800\text{ }^\circ\text{C}$), which is close to its melting point. At this temperature, the porosity of dolomite reduces resulting in an increased bulk specific density of the product making it suitable for refractory applications. Figure 5-8 depicts the conversion degree of the dolomite including the calcination of magnesite and limestone. The profile of conversion degree also endorses that the calcination of the magnesite and limestone completes at $z = 68\text{ m}$ and $z = 82\text{ m}$ respectively. The results of T_G , T_S and T_W obtained from the simulation model are compared with literature data by Ludera (1974) and are shown in figure 5-8 as point value. The results of simulations show good agreement with the experimental results with a maximum deviation of below 10 %. The data on maximum bulk bed and gas temperature as well as the flue gas temperature, the wall heat loss, residence time and product quality are summarized in appendix (D.2).

5.3 Titanium dioxide

5.3.1 Kiln and process parameters

Figure 5-10 shows the schematic of the kiln used for calcination of the titanium oxide. The kiln has a length of $L = 45$ m and an outer diameter of $D_{\text{shell}} = 2.8$ m i.e. length to diameter (L/D) is around 20. Kiln shell is protected from thermal load by an insulation layer with a thickness of $s_{w,2} = 120$ mm and refractory layer of thickness $s_{w,1} = 130$ mm. The kiln is inclined with $\beta = 3^\circ$ and is operated with rotational speed of $n = 0.33$ rpm. The combustion process here was carried out in a separate combustion chamber and the gases fed to the kiln with volumetric flow rate of $V_g = 13160$ m³_{STP}/h with a temperature of $T_{G,L} = 1038$ °C. The mass flow rate of the material was maintained at $\dot{M}_{S,z=0} = 8.25$ t/h, while the mass flow rate of the outlet product was $\dot{M}_{S,z=L} = 3.68$ t/h. Detailed technical data is provided in appendix (E.1).

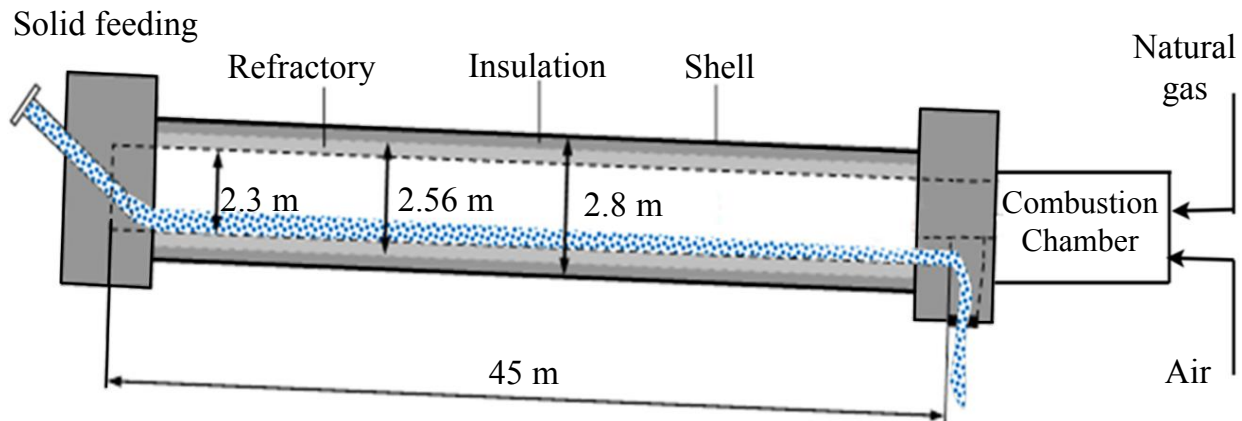


Figure 5-10: Simplified sketch of kiln outline used in titanium dioxide production.

5.3.2 Results and validations

The axial profile of the filling degree within the kilns is shown in figure 5-11. At the inlet the filling degree is $F_{z=0} = 6.9$ % and it decreases due to the slope of the kiln. Starting from $z = 0$ m till $z = 36$ m, the material undergoes different chemical and physical

changes e.g. dehydration of the physical and the chemical water which lead to change in the mass of the bulk bed. Hence, the filling degree decreases from $F_{z=0} = 6.9\%$, to $F_{z=36} = 3\%$. Afterwards the filling degree shows moderate change till $z = 42$ m whereas, steep decrease is seen thereafter till outlet $F_{z=L} = 1\%$.

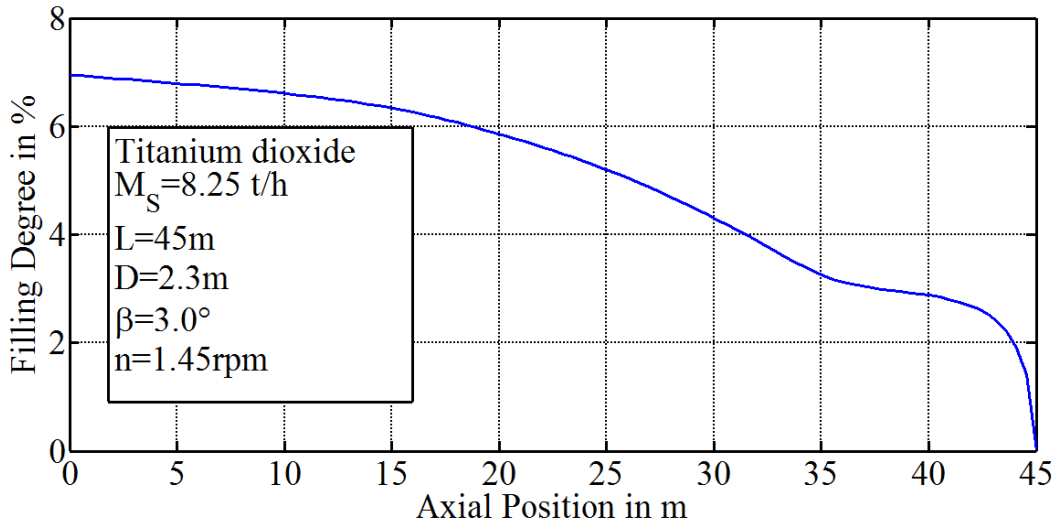


Figure 5-11: The axial filling degree profile for titanium dioxide decomposition in a rotary kiln ($L = 45$ m, $D = 2.3$ m).

The Figures 5-12 and 5-13 represent the spatial change of the temperature of the bulk bed T_s , the gas T_G , inner wall surface T_w and the outer shell surface T_{Shell} in addition to the conversion degree of titanium oxide within the kiln. The combustion process was carried in a separate combustion chamber and the gases enter the kiln with pre-specified temperature $T_{G,L} = 1038$ °C. The temperature of the gases decreases steadily through the kiln due to the heat transfer between the wall surface and the bulk material till they leave the kiln with $T_{G,0} = 421$ °C.

The bulk material on other hand enters the kiln with $T_{s,0} = 45$ °C. The temperature of the bulk bed shows a negligible change from $z = 0$ m to $z = 36$ m. The temperature of material shows a sudden increase after $z = 36$ m. This result can be explained using results presented in figure 5-13. The bulk material start to dehydrate at temperature lower

than 100 °C and as dehydration is an endothermic process, the temperature of the bulk material does not rise significantly. At $z = 15$ m, it reaches $T_{S,z=15} = 100$ °C and the evaporation of the physical water starts. The temperature of the solid shows a constant temperature till $z = 36$ m where the evaporation is completed. The desorption increases gradually from $z = 15$ m to $z = 36$ m with $U_{S,Desorption} = 10\%$ at $z = 36$ m, then instantaneously the rate of desorption increases and completes within 1 m due to the availability of the heat supply after finishing the evaporation. The temperature of the bulk bed sharply increases. It can also be seen that as the temperature of the bulk exceeds 600 °C desulphurization takes place while it is followed by the rutilisation after the temperature of the bulk bed reaches 700 °C. Both of these processes accomplish within 1 m of the kiln. The temperature of the material at the outlet is found to be $T_{S,L} = 933$ °C.

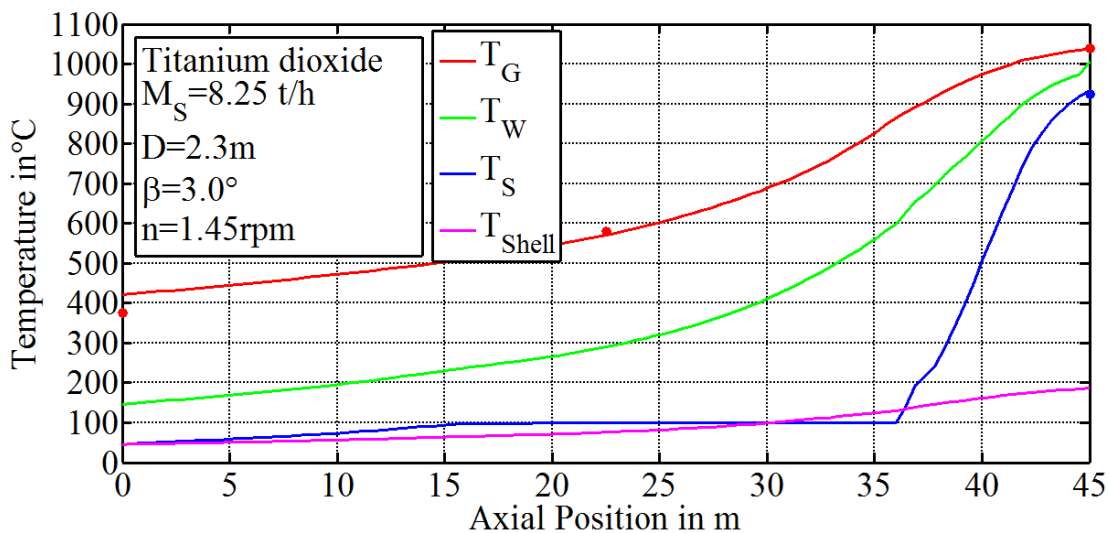


Figure 5-12: Axial temperature profiles for titanium dioxide decomposition in a rotary kiln ($L = 45$ m, $D = 2.3$ m).

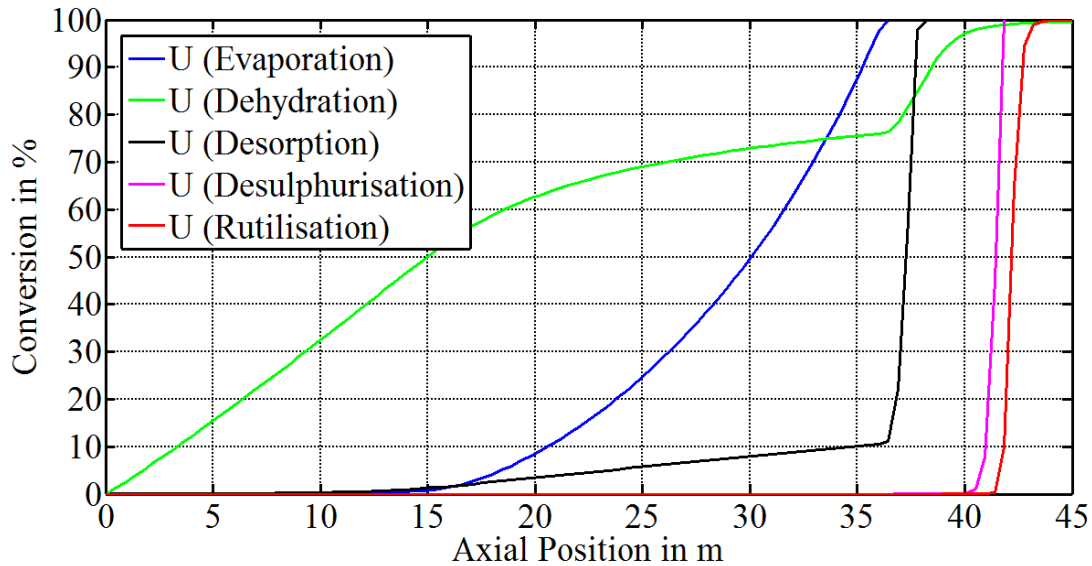


Figure 5-13: The axial conversion profiles for titanium dioxide decomposition in a rotary kiln (L = 45 m, D = 2.3 m).

The figure 5-14 shows the amount of substances in relation to the amount in final product as fed material is subjected to various physical and chemical processes within the rotary kiln. Figure also shows the profile of corresponding temperature. The feed material losses 44.5 % of its mass during these processes.

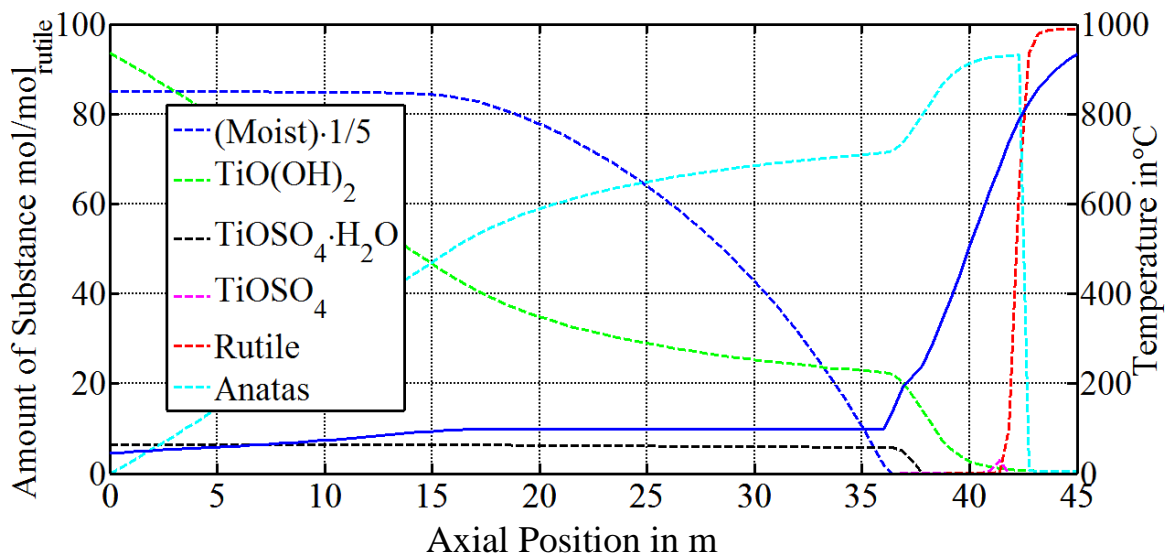


Figure 5-14: The axial amount of substance profiles for titanium dioxide decomposition in a rotary kiln (L = 45 m, D = 2.3 m).

The results of T_G , T_s , T_w and T_{Shell} obtained from the result of the simulation model are also compared with the literature Ginsberg (2011) shown by points in figure 5-12. The results of simulations show good agreement with the experimental results with a maximum deviation of around 12 %. The data on maximum bulk bed and gas temperature as well as the flue gas temperature, the wall heat loss, residence time and product quality are summarized in appendix (E.2).

6 Experiments in industrial rotary kilns

6.1 Cement

6.1.1 Kiln and process parameters

Cement is most commonly produced by using the dry process as discussed earlier in section 3-3. The model developed in this study is employed to predict the process behavior during the manufacturing of the cement. The kiln and process parameters, as well as the material properties are taken from an industrial case.

The simplified diagram of the industrial rotary kiln for cement production is shown in figure 6-1. The kiln has a length of $L = 60$ m and an outer diameter of $D_{\text{Shell}} = 4.1$ m. The reaction atmosphere is insulated from the shell body via two layers: first the thermal refractory bricks with a thickness of $s_{w,1} = 150$ mm and the second layer with thickness $s_{w,2} = 100$ mm as insulation layer. The ratio of length to diameter (L/D) is around 14.6. The inclination angle of the kiln is $\beta = 2.29^\circ$ and it is operated with a rotational speed of $n = 8$ rpm and with a power of $P = 38.7$ MW. Coal is used as fuel whereas, air is injected mainly through the burner nozzles with an air excess number of $\lambda = 1.3$. It is divided into primary and secondary air. The flame length is $L_{\text{Flame}} = 10$ m and the preheated combustion air temperature is found to be 696°C . The material is fed with a mass flow rate of $\dot{M}_{s,z=0} = 129$ t/h. The product is withdrawn at a rate of $\dot{M}_{s,z=L} = 118.5$ t/h. The raw material is preheated before entering to a temperature of $T_{s,0} = 890^\circ\text{C}$. The material undergoes calcination of limestone during the preheating process and the conversion degree is found to be 85 %. Technical data and the material composition are provided in appendix (F.1, F.2).

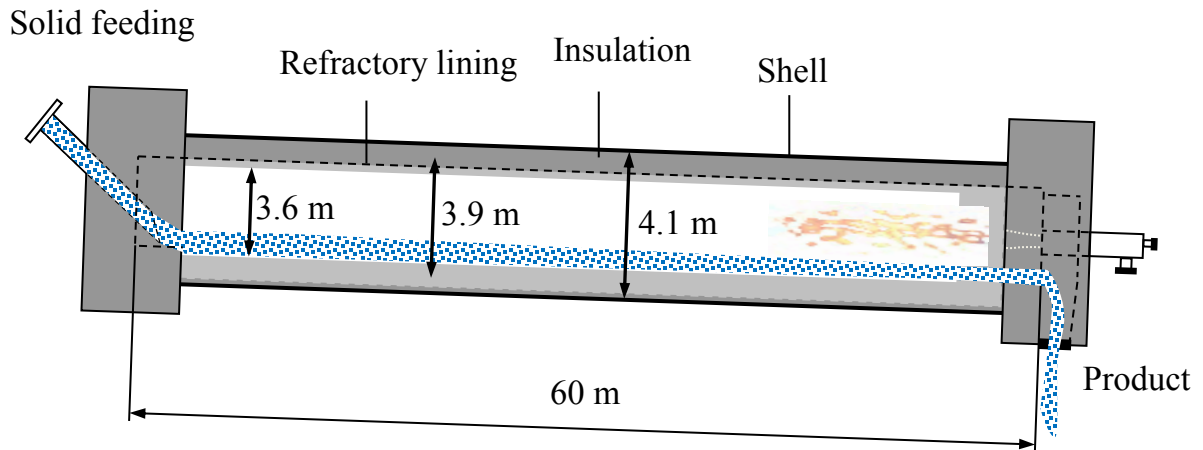


Figure 6-1 Schematic diagram of the industrial cement rotary kiln

6.1.2 Results and validations

The figure 6-2 shows the axial profile of filling degree. At the inlet of the rotary kiln ($z = 0$ m) the filling degree is almost $F = 7.4\%$. It decreases smoothly till $z = 50$ m. At this point, the calcination of the limestone completes. The filling degree shows a steep decline from $z = 50$ m till $z = 60$ m due to the rotation and inclination of the kiln. Filling degree is $F_L = 1\%$ at the outlet of kiln.

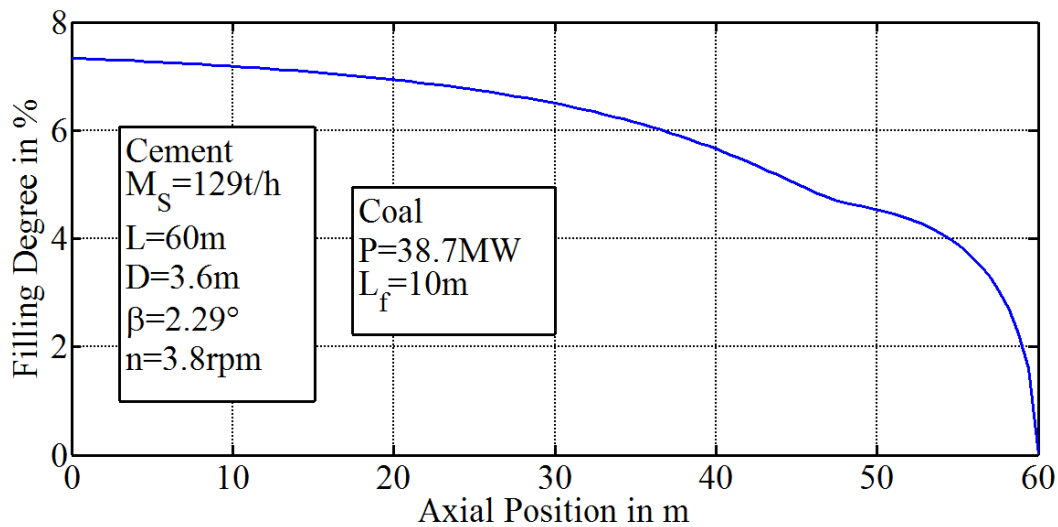


Figure 6-2: The axial filling degree profile for cement sintering in an industrial rotary kiln ($L = 60$ m, $D = 3.6$ m).

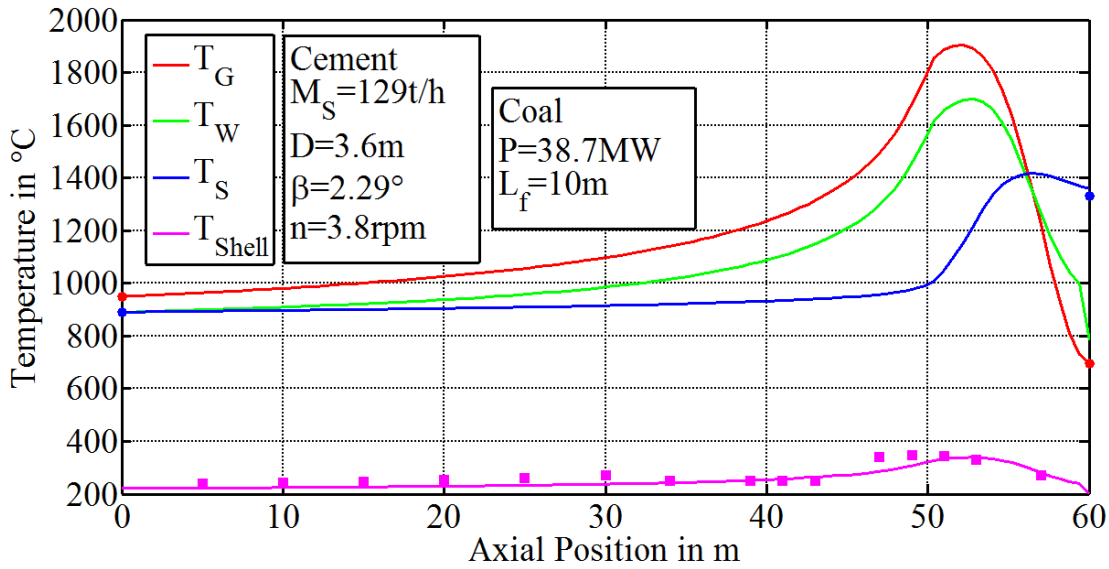


Figure 6-3: Axial temperature profiles for cement sintering in an industrial rotary kiln ($L = 60$ m, $D = 3.6$ m).

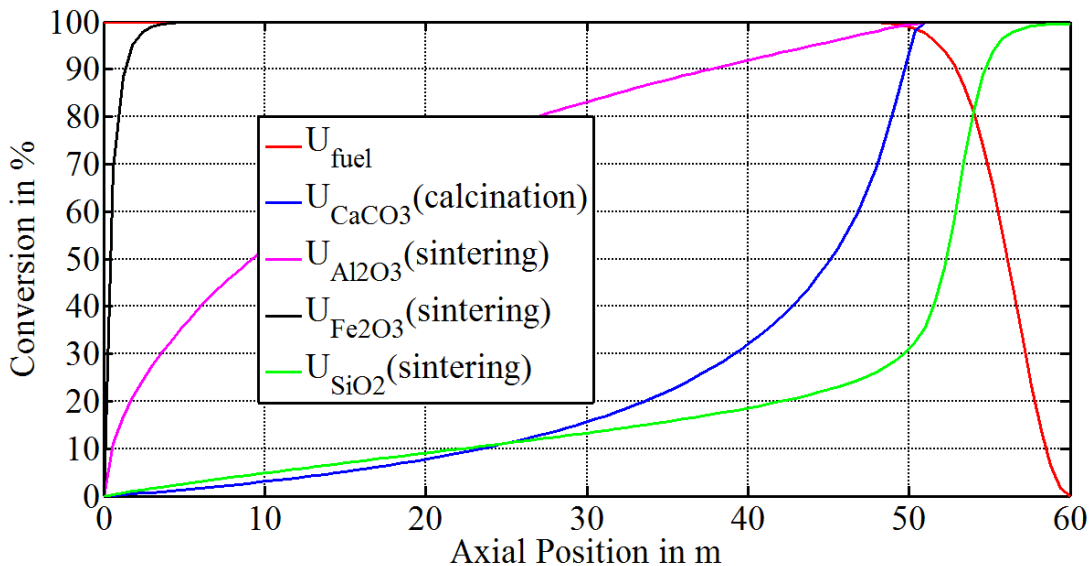


Figure 6-4: The axial conversion profiles for cement sintering in an industrial rotary kiln ($L = 60$ m, $D = 3.6$ m).

The results of model based on the simulation for axial profile of temperature of the bulk bed T_S , gas phase T_G , the inner wall surface T_W and the outer shell surface T_{Shell} as well as the conversion degree of fuel and the cement are shown in figure 6-3 and 6-4. Due to the combustion reaction in the flame zone, the temperature of the gas increases to

$T_{G,max} = 1905$ °C at the end of the flame. The temperature of the gas decreases due to the heat transfer to the bulk bed and the kiln wall and it leaves the kiln with a temperature of $T_{G,0} = 945$ °C. The raw meal is fed to the kiln at a temperature of $T_{S,0} = 890$ °C. The material is exposed to a calcination throughout the kiln and completes at around $z = 50$ m. The figure 6-3 reveals that the temperature change of solids with the axial length is not changing notably due to the endothermic limestone calcination. Temperature rises after $z = 50$ m sharply due to the flame and occurrence of exothermic reactions in this region. The material is further heated due to heat transfer from the gas and achieve the maximum temperature of $T_{S,max} = 1443$ °C. After reaching the peak temperature, it losses heat to the gas and the wall and its temperature decreases. It leaves the kiln with a temperature of $T_{S,L} = 1370$ °C. The industrial data on the temperature of the shell, solid at inlet and gas at inlet and outlet is also shown (point values) in figure 6-3. The simulation results are in good agreement with industrial data with a maximum deviation below 10 %. The solid enters the kiln with an elevated temperature 890 °C prior to the sintering process, the solid material is preheated and partially calcinated in the preheater cyclones, the solid material with 85 % calcinated limestone enters the rotary kiln and completed at $z = 50$ m. The formation of oxides starts slightly at the $z = 0$ m, due to existence of CaO. Due to the chemical endothermic reaction, the temperature does not show notable elevation, so the formation of oxides is limited. After the completion of calcination reaction, the temperature shows a steep increase as the material approaches peak temperature zone and the endothermic calcination reaction completes. Starting from $z = 50$ m, the oxides formation shows a significant increase in quantity. The figure 6-5 expresses the concentration of the oxides related to the lime.

The results obtained through simulation (solid lines) are compared with the data obtained from industry (points). Both these results agree very well. Thus, this model can explain the process of clinker formation successfully. The data on maximum bulk bed and gas temperature as well as the flue gas temperature, the wall heat loss, residence time and product quality are summarized in appendix (F.3).

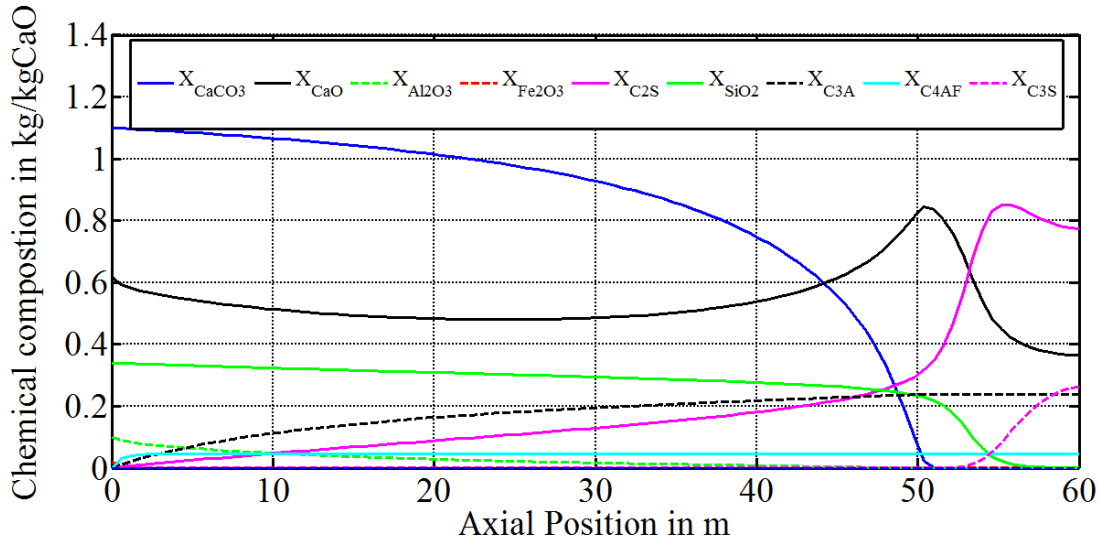


Figure 6-5: The chemical composition for cement sintering in an industrial rotary kiln ($L = 60$ m, $D = 3.6$ m).

6.2 Limestone

6.2.1 Kiln and process parameters

The schematic representation of the rotary kiln used in the calcination of limestone is shown in figure 6-6. The kiln has a length of $L = 86$ m and an outer diameter of $D_{\text{shell}} = 3.45$ m. The kiln is divided into two segments: first, from $z = 0$ m to $z = 53$ m with an internal diameter $D = 3.05$ m and two different layers of refractory. With a thickness of the first layer $s_{w,1} = 160$ mm, and a thickness of the second layer $s_{w,2} = 40$ mm. Second, the segment from $z = 53$ m to $z = 86$ m with an internal diameter $D = 2.92$ m with other two different layers of refractory, the first layer has a thickness of 200 mm, while the thickness of the second layer is 65 mm. The ratio of length to diameter (L/D) is around 28. The inclination angle of the kiln is $\beta = 3^\circ$. It is operated with a rotational speed of $n = 1.45$ rpm and with a power of $P = 38$ MW. Pulverized lignite is used as fuel whereas, air is injected mainly through the burner nozzles divided into primary and secondary air with an air excess number of $\lambda = 1.06$. The burner is located 0.5 m inside the kiln at the far end which ensures the flame length $L_{\text{Flame}} = 20$ m and combustion air temperature is found to be 445°C . The limestone is fed with a mass flow rate of $\dot{M}_{S,z=0} = 45$ t/h and a

particle size of $d_p = 26 \text{ mm}$. At the outlet of the kiln product is obtained at a rate of $\dot{M}_{S,z=L} = 25 \text{ t/h}$. The raw material is preheated before entering the kiln till the temperature of the solid reaches $T_{S,0} = 850 \text{ }^\circ\text{C}$. The material undergoes calcination during the preheating process and the conversion degree is found to be 15 %. All the Technical data is provided in appendix (G.1).

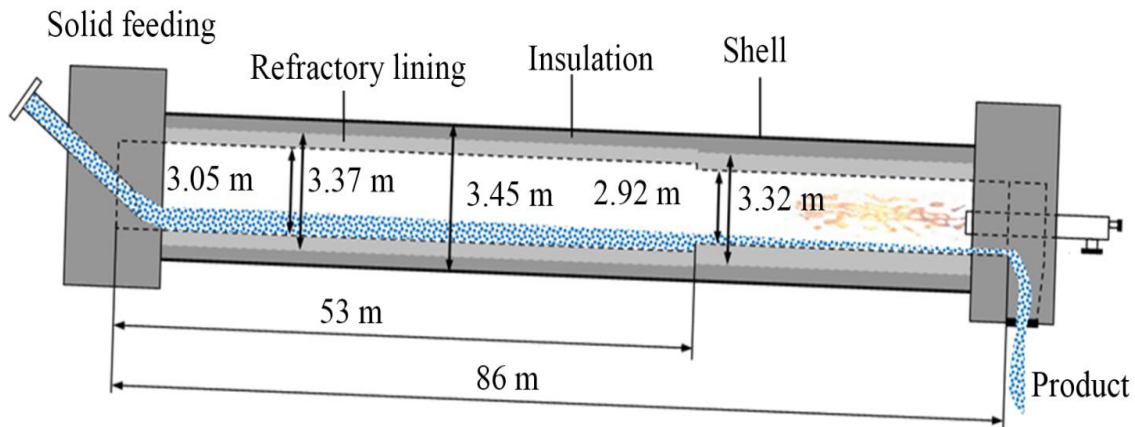


Figure 6-6: Schematic diagram of the rotary kiln for limestone calcination.

6.2.2 Results and validation

The figure 6-7 shows the axial profile of filling degree. At the inlet of the rotary kiln ($z = 0 \text{ m}$) the filling degree is almost $F = 6.6 \%$. It decreases till the point where the cross section of the kiln gets narrow where a slight increase in the filling degree from the value of $F_{z=53} = 5.9 \%$ till $F_{z=54} = 6 \%$ is noted. The filling degree decreases as the material moves in the axial direction from $z = 54 \text{ m}$ to $z = 86 \text{ m}$ towards the outlet to a value of $F_L = 1.5 \%$. The filling degree faces constant decline after $z = 54 \text{ m}$, while the biggest gradient lies between $z = 80 \text{ m}$ to $z = 86 \text{ m}$.

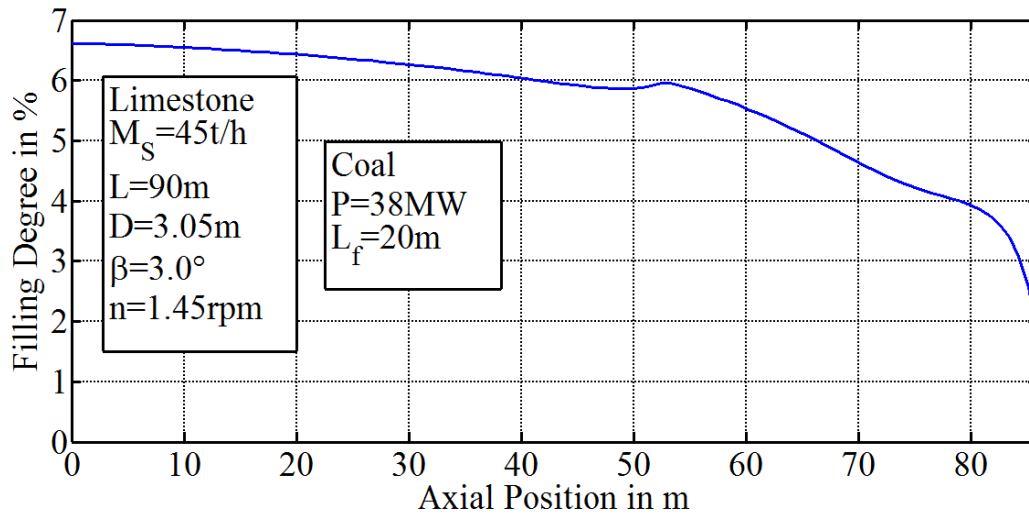


Figure 6-7: The axial filling degree profile for limestone decomposition in an industrial rotary kiln ($L = 86$ m, $D = 3.05$ m).

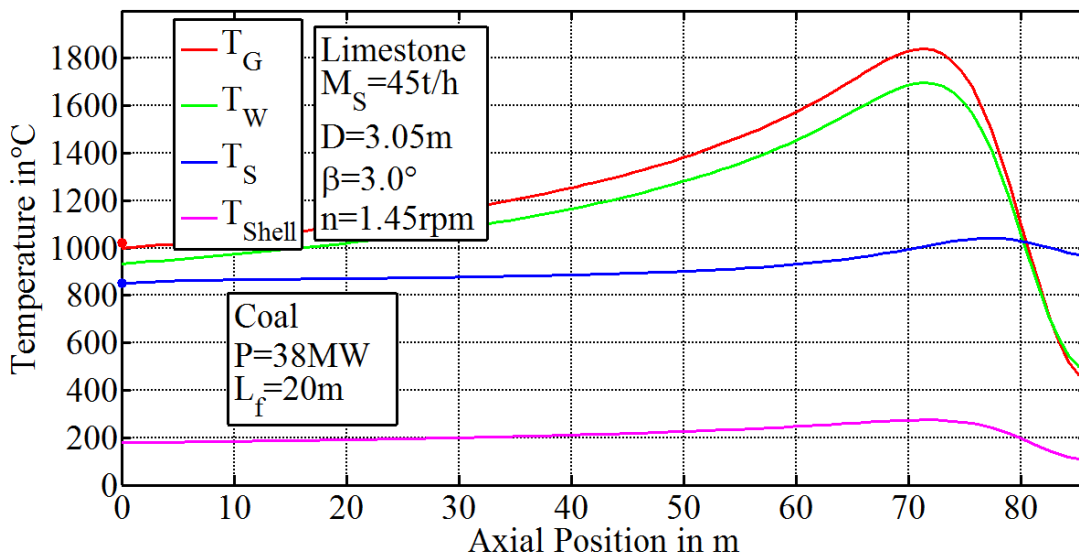


Figure 6-8: Axial temperature profiles for limestone decomposition in an industrial rotary kiln ($L = 86$ m, $D = 3.05$ m).

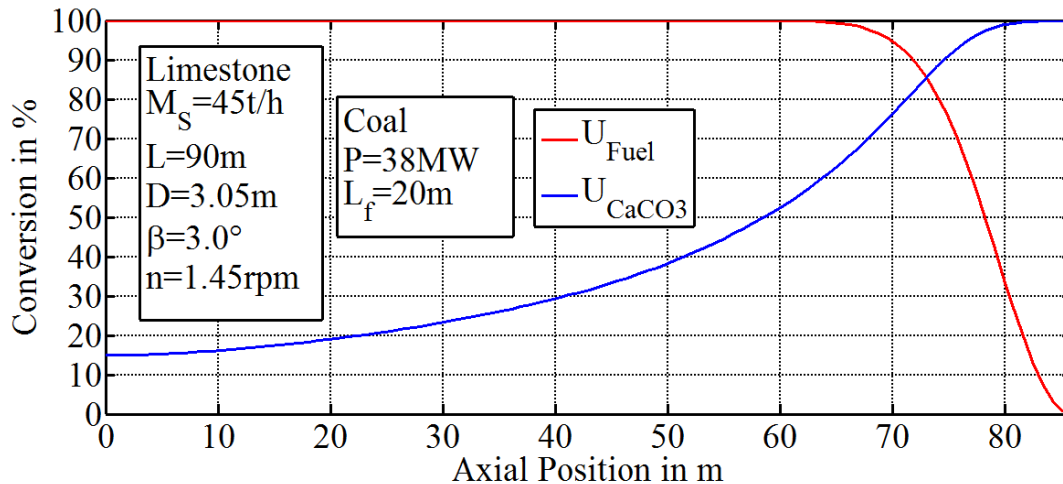


Figure 6-9: The axial conversion profiles for limestone decomposition in an industrial rotary kiln ($L = 86$ m, $D = 3.05$ m).

The results of model based on the simulation for axial profile of temperature of the bulk bed T_s , gas phase T_G , the inner wall surface T_w and the outer shell surface T_{shell} as well as the conversion degree of fuel and the limestone are shown in figure 6-8 and 6-9. Due to the combustion reaction in the flame zone, the temperature of the gas increases to $T_{G,max} = 1839$ °C at the end of the flame . The gas temperature decreases due to the heat transfer to the bulk bed and the kiln wall and the gas leaves the kiln with an exhaust temperature of $T_{G,0} = 1000$ °C. The Limestone is fed to the kiln at a temperature of $T_{s,0} = 850$ °C. The limestone is calcined to a certain degree during the preheating and the conversion degree of the limestone which enters the kiln is $U_{s,0} = 15$ %. It is heated to the maximum temperature of $T_{s,max} = 1040$ °C inside the kiln due to heat transfer from the gas and the wall and the conversion of limestone $U_{s,L} = 99.9$ % is achieved by burning the brown coal dust. After reaching this temperature, it losses heat to the gas and the wall and its temperature decreases to a product temperature of $T_{s,L} = 961$ °C. The figure 6-9 shows that the gradient of conversion increase with the gas temperature. The maximum gradient lies in the region of the flame end. The results made by industrial measurements for the temperature of the gas and the solid at inlet and outlet are also shown in figure 6-8. Moreover, the simulation results fits very well with industrial data a maximum deviation of around (3 %). The data on maximum bulk bed and gas temperature as well as the flue

gas temperature, the wall heat loss, residence time and product quality are summarized in appendix (G.2).

6.3 Kaolin

6.3.1 Kiln and process parameters

The schematic diagram of the rotary kiln used in the processing of kaolin is shown in figure 6-10. The kiln has a length of $L = 34$ m and an outer diameter of $D_{\text{shell}} = 2.76$ m so that the ratio of length to diameter (L/D) is around 16.1. The kiln wall is insulated two layers of refractories: first, thermal refractory bricks with its thickness $s_{w,1} = 300$ mm and the second layer with thickness $s_{w,2} = 30$ mm as insulation layer. The inclination angle of the kiln is $\beta = 1.7^\circ$. It is operated with a rotational speed of $n = 1.4$ rpm and with a power of $P = 2.88$ MW. Natural gas is used as a fuel and air with an excess number of $\lambda = 1.12$ is injected mainly through the burner nozzles which is divided into primary and secondary air. The flame length is $L_{\text{Flame}} = 12$ m and a combustion air temperature is found to be 470°C . The material is fed with a mass flow rate of $\dot{M}_{S,z=0} = 3.8$ t/h with a particle size of $d_p = 3\mu\text{m}$. The production rate of this kiln is $\dot{M}_{S,z=L} = 3.2$ t/h. The raw material is preheated before entering the kiln till the temperature of the solid reaches $T_{S,0} = 400^\circ\text{C}$. The material undergoes calcination of kaolin during the preheating process. Technical data is provided in appendix (H.1).

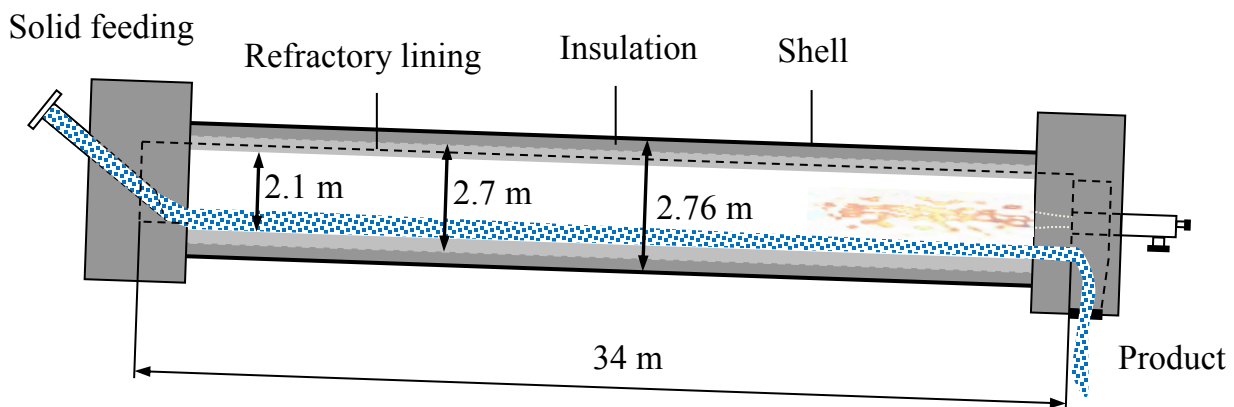


Figure 6-10: Schematic diagram of the rotary kiln for kaolin

6.3.2 Results and validation

The axial profile of filling degree of the kaolin is depicted in figure 6-11. The filling degree is $F_{z=0} = 14.3\%$ at the inlet of the kiln. The profile of the filling degree shows a steady decrease, in the range from the entrance ($z = 0$ m) to $z = 15$ m with $F_{z=15} = 12.3\%$. After $z = 15$ m, the filling degree decreases with a comparatively bigger slope due to the mass loss of the material as a result of dihydroxylation reaction. This reaction completes at $z = 27$ m and the filling degree here has a value of $F_{z=27} = 8\%$. Subsequently, the filling degree does not change significantly during the formation of spinal and mulitt and the filling degree at the exit of kiln is $F_{z=L} = 1\%$.

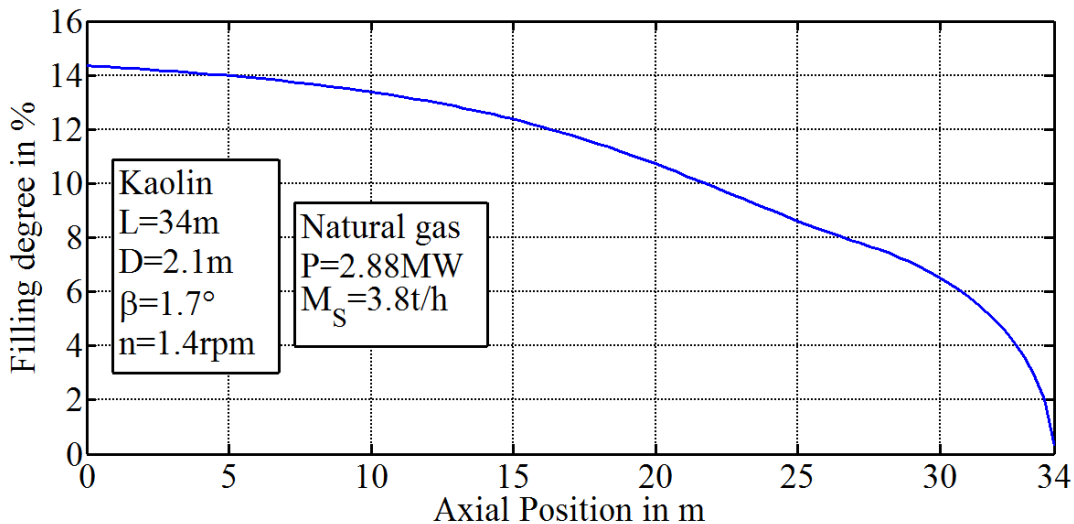


Figure 6-11: The axial profile of filling degree for kaolin decomposition in an industrial rotary kiln ($L = 34$ m, $D = 2.1$ m).

The figure 6-12 and 6-13 show the simulation results of axial profile of temperature of the bulk bed T_s , gas phase T_G , the inner wall surface T_w and the outer shell surface T_{shell} as well as the conversion degree of fuel and the limestone (solid lines). It can be seen from the figure 6-12 that the temperature of the gas increases from $T_{G,L} = 471\text{ }^\circ\text{C}$ to $T_{G,z=27} = 1556\text{ }^\circ\text{C}$ due to the combustion in the flame zone. The combustion in the process is carried out with a premixed flame of natural gas. The temperature of the gas reaches its

peak at $z = 27$ m and decreases to $T_{G,0} = 563$ °C due to the heat transfer with the bulk material and the wall.

The kaolin is fed to the kiln at a temperature of $T_{S,0} = 400$ °C, the temperature of the bulk material increases steadily from the entrance ($z = 0$ m) until $z = 15$ m. The dihydroxylation reaction starts at $z = 15$ m and completes at $z = 27$ m as shown by its conversion degree in figure 6-12. The temperature of solid rises with nearly same slope as before. After $z = 27$ m subsequently the spinel formation starts which is an instantaneous reaction as shown in figure 6-13. The temperature of the bulk bed increases sharply after $z = 27.5$ m where the spinel formation completed to peak temperature of $T_{S,max} = 1177$ °C at $z = 29.2$ m. The bulk materia exchanges heat with the gases and the wall and leaves the kiln at $T_{S,z=L} = 921$ °C. The comparison of simulations results with industrial data (points) is also presented in figure 6-12. It can be clearly seen that they match well. The maximum deviation between them is found to be below 10 %. The data on maximum bulk bed and gas temperature as well as the flue gas temperature, the wall heat loss, residence time and product quality are summarized in appendix (H.2).

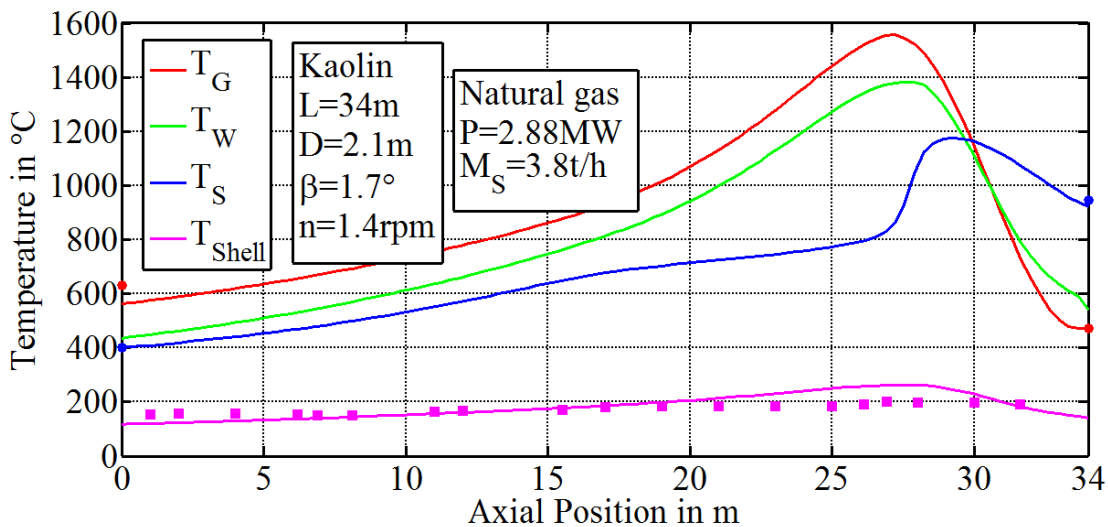


Figure 6-12: Axial temperature profiles for kaolin decomposition in an industrial rotary kiln ($L = 34$ m, $D = 2.1$ m).

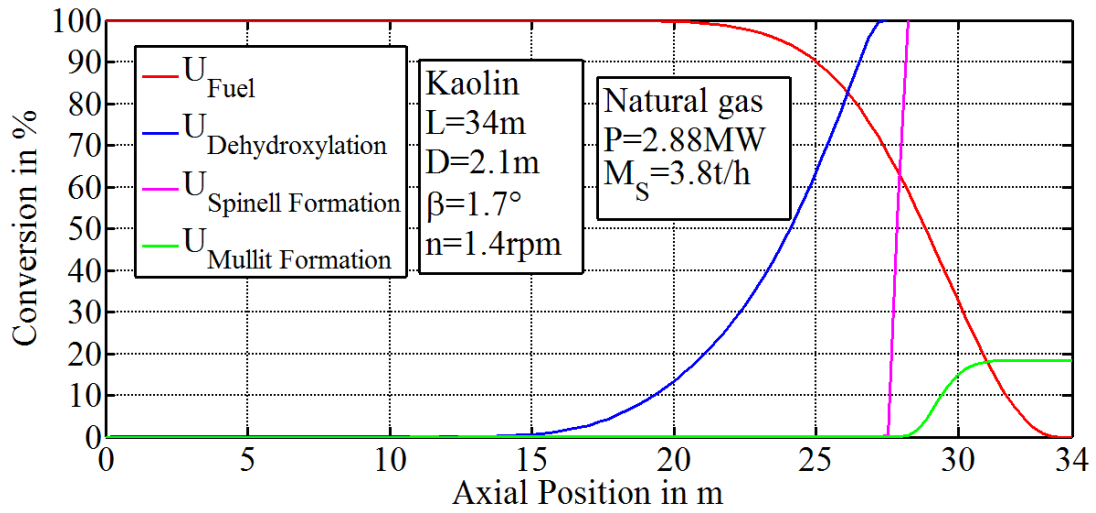


Figure 6-13: The axial conversion profiles for kaolin decomposition in an industrial rotary kiln ($L = 34\text{ m}$, $D = 2.1\text{ m}$).

7 Conclusion and future work

7.1 Conclusion

A mathematical model was developed to simulate the process behavior of the bulk materials in direct fired rotary kilns. This model includes the coupled phenomenon of heat transfer, bulk bed motion behavior, the axial bulk material transport and bulk bed reaction behavior. In the present work special emphasis has been given to the heat released or absorbed during the chemical reactions undergone by material being processed inside the rotary kiln. In order to show variability and to prove the stability of the developed model, in total eight different thermochemical processes were modelled.

The model is based on the discretization of the rotary kiln into infinitesimally small volume elements. In these volume elements, the phases of the gas, the bulk bed and the kiln wall are defined, whereas for each of the phases the differential energy balance is written. Especially the term for bulk bed reaction was analyzed in detail. The reaction terms are represented as the conversion degree using theoretical models such as the Spang model for cement, shrinking core model for limestone, magnesite, dolomite, aluminum dross and siderite, and Ginsberg model for titanium dioxide.

These reaction terms are coupled with the models for the heat transfer, gas-bulk bed, gas-kiln wall, bulk bed-kiln wall, outer kiln shell-ambient and the heat transport in the kiln wall as well as the bulk bed transport in axial and transversal direction. This leads to a system of coupled ordinary differential equations and a set of non-linear algebraic equations which is solved with Matlab (2016) code.

It is now possible to simulate the axial profiles of the temperatures (gas, bulk bed, kiln wall, kiln shell), the filling degree (bulk bed height) and the bulk bed reaction

conversion degree. Out of this for the first time the mass change of the bulk bed as well as quality of the bulk product can be described in detail along the kiln length.

To validate the theoretical model, experiments have been done for selected process in a pilot rotary kiln of 5 m length and in industrial rotary kilns of 86 m, 60 m, 34 m length. Furthermore, the simulations were validated for selected materials based on literature data of industrial rotary kilns of 119 m, 90 m, 45 m length.

A wide parameter variation (rotational speed, inclination angle, kiln dimensions, process behavior) was realized by the different kiln conditions. In dependence on the data availability, a comparison of simulated and experimental data for the axial temperature profiles and the product quality was done. The model is found to be good in its predictions. This model can be used on the one hand for the optimization of the rotary kiln process and on the other hand for the design, the construction and the engineering of the rotary kiln plants.

7.2 Future work

The following studies could be carried out in future to further improve this model:

- 1) During the development of this model, the sub processes are modelled by using macroscopic models which use the mean particle size for defining the bed. However, the bed is made up of polydispersed bulk materials. Segregation effect can occur, so that a core with small particles is enclosed by an outer ring with larger particles (ring-core structure), forms inside the bed. Due to segregation effects, large temperature gradients in the bulk bed are particularly noticeable in case of polydispersed bulk materials. Since such polydispersed bulk materials are frequently treated in industrial applications, the consideration of the segregation effects in the process model is recommended. To determine the heat transport in the bulk bed and to specify the reaction behavior of each grain fraction.
- 2) Due to the transverse segregation effects of polydispersed particles, the residence times of the individual particles also fluctuate. For example, larger particles are significantly shorter in residence time in the active layer of the bed

than smaller particles, which they accumulate exclusively in the core of the bed. It is therefore recommended to use the help of population balances to determine the property distributions of the individual grain classes and to insert the corresponding statistical residence time distributions into the process model.

References

- (1) Agustini, S.S.; Queck, A.; Specht, E.: Modeling of the Regenerative Heat Flow of the Wall in Direct Fired Rotary Kilns. *Heat transfer Engineering*, 29,1,2008, S.57-66
- (2) Atesok Gündüz.; Dincer Hayrünisa.: Feasibility Studies for Calcination and Sintering of Hekimhan–Deveci Siderite Ores, I.T.U. Maden Fakültesi, Cevher ve Kömür Hazırlama Anabilim Dalı
- (3) Belanger, P.R.; Dumont, G.: Steady-state study of a titanium dioxide rotary kiln. *Industrial and Engineering Chemistry Process Design and Development*, 17, 2, 1978, S.107-114
- (4) Boateng, A.A.: *Rotary Kilns* (2th ed.). New York, McGraw-Hill, 2008
- (5) Boateng, A.A.; Barr, P.V.: A thermal model for the rotary kiln including heat transfer within the bed. *International Journal of Heat and Mass Transfer*, 39, 10, 1996, S.2131-2147
- (6) Boynton, R.S.: *Chemistry and Technology of Lime and Limestone*, New York, John Wiley and Sons, 1980
- (7) Buxbaum, G.; Pfaff G.: *Industrial inorganic pigments*. 2005, Wiley-VCH, 3. Auflage.
- (8) Bye, G.C.: *Portland Cement*, 3rd edition. London, Thomas Telford Limited Jan. 2011
- (9) Carvalho, L.S.: Estado da arte da tecnologia do tratamento de escória na indústria do alumínio. In: III Seminário de Tecnologia da Indústria do alumínio, 20 a 21 de agosto de 1991. São Paulo, Brasil. ABAL, pp. 169-192.
- (10) Cheng, C.; Specht, E.: Reaction rate coefficients in decomposition of lumpy limestone of different origin. *Thermochimica Acta*, 2006, 449, 8-15
- (11) Cherubini, F.; Raugei, M.; Ulgiati, S.: LCA of Magnesium Production Technological Overview and Worldwide Estimation of Environmental Burdens. *Resources, Conservation and Recycling*, 52, 2008, 1093-1100.
- (12) Deelman, J.C.: Low-temperature nucleation of magnesite and dolomite, *Neues Jahrbuch für Mineralogie, Monatshefte*, 1999, pp. 289-302.
- (13) Deer, W. A.; R. A. Howie.; Zussman, J.: *An Introduction to the Rock Forming Minerals*, Longman, 1966, pp. 489-493. ISBN 0-582-44210-9.
- (14) Dumont, G.; B´elanger P. R.: Steady-state study of a titanium dioxide rotary kiln. *Industrial and Engineering Chemistry Process Design and Development*, 17(2), 1978,107-114
- (15) Frisch V.: Vereinfachtes mathematisches Modell der Wärme Übertragung im Zementdrehrohrofen unter Berücksichtigung chemischer Reaktionen Dissertation, TU Clausthal, 1983
- (16) Gallagher P K.; Warne S.St.J.: Thermomagnetometry and Thermal Decomposition of Siderite. *Thermochimica Acta*, 1981, 43: 253-267.

- (17) Georgallis, M.; Nowak, P.; Salcudean, M.; Gartshore, I.S.: Modelling the rotary lime kiln. *The Canadian Journal of Chemical Engineering*, 83, 2005, S.212-223
- (18) GeoScience Australia.: Magnesium Fact Sheet. Retrieved November 01, 2009, from Australian Atlas of Mineral Resources, Mines & Processing Centres: <http://www.australianminesatlas.gov.au>
- (19) Gesenhues, U.: Calcination of metatitanic acid to titanium dioxide white pigments. *Chemical Engineering and Technology*, 2001, 24(7):685–694.
- (20) Ginsberg, T.; Modigell, M.: Dynamic modelling of a rotary kiln for calcination of titanium dioxide white pigment. *Computer and Chemical engineering*, 2011, 35, pp.2437-46.
- (21) Ginsberg, T.; Modigell, M.; Wilsmann, W.: Thermochemical characterisation of the calcination process step in the sulphate method for production of titanium dioxide. *Chemical engineering research and design*, 2010, 89, pp.990-94.
- (22) Gnielinski, V.: Ein neues Berechnungsverfahren für die Wärmeübertragung im Übergangsbereich zwischen laminarer und turbulenter Rohrströmung. *Forschung im Ingenieurwesen-Engineering Research*, 61, 9, 1995, S.240-248
- (23) Gualtieri, A.; Belloto, M.; Artioli, G.; Clark, S.: Kinetic Study of the Kaolinite-Mullite Reaction Sequence. Part II: Mullite Formation. *Phys Chem Minerals*, 1995, 22, pp.215-22.
- (24) Guruz HK.; Bac N: Mathematical modeling of rotary cement kilns by the zone method. *Can J Chem Eng*, 1981, 59:540–548
- (25) Hamilton, J.: *Australia's Mining Monthly*, 2000
- (26) Heine, H.; Kischkewitz, J.; Woditsch, P.; Westerhaus, A.; Griebler Gardiner, S.P. and Long, V.D. (1966). Thermal decomposition of a blackband ironstone. II. Kinetics. *J. Appl. Chem.*, 16: 132-136.
- (27) Herz, F.: Entwicklung eines mathematischen Modells zur Simulation thermischer Prozesse in Drehrohröfen. Docupoint-Verlag, 2012
- (28) Hetherington, L. E.: *World Mineral Production: 2001–2005*. British Geological Survey, 2007, ISBN 978-0-85272-592-4.
- (29) Imber, M.; Paschkis, V.: A new theory for a rotary-kiln heat exchanger. *International Journal of Heat and Mass Transfer*, Volume 5, Issue 7, July 1962, Pages 623-638.
- (30) Jagtap S.B.; Pande A.R.; Gokarn A.N.: Kinetics of Thermal Decomposition of Siderite: Effect of Particle Size, *International Journal of Mineral Processing* (36), 1992, 113-124
- (31) Jeschar, R.; Kostowski, E.; Alt, R.: *Wärmestrahlung in International Studies in Science and Engineering*, Papierflieger, Clausthal-Zellerfeld, 2004
- (32) Kolditz, L.: *Anorganische Chemie, Band 2*. VEB Deutscher Verlag der Wissenschaften, 1980, Berlin.
- (33) Kostuch JA.; Walters V.; Jones TR.: High performance concretes incorporating metakaolin, a review. In: Dhir RK, Jones MR, editors. *Concrete 2000, economic and durable concrete through excellence*. London: E and FN Spon. p.1799-811.

- (34) Kulik, G.J.; Daley, J.C.: Aluminum Dross Processing in the 90's, in 2nd Int. Symp. Recycl. Met. Eng. Mater, TMS-AIME, Warrendale, 1990, PA, pp.427
- (35) Lavoie S.; Dube G.; A salt-free treatment of aluminium dross using plasma heating. *J Metals*, 1991, 2, 54–5.
- (36) Ludera, M.L.; Beitrag zum Wärmeübergang in Dolomit- und Magnesitdrehrohröfen. *TIZ-Fachbericht*, 109, 10, 1985, S.760-765
- (37) Ludera, M.L.; Beitrag zum Wärmeübergang in Dolomit- und Magnesitdrehrohröfen. *TIZ-Fachbericht*, 109, 8, 1986, S.524-531
- (38) Mackenzie, K. J. D.: The calcination of titania V, Kinetics and mechanism of the anatase-rutile transformation in the presence of additives. *Transactions and Journal of the British Ceramic Society*, 1975, 74(3):77–84.
- (39) Manitius, A; Kurceyuz, E.; Kawecki, W.: Mathematical model of the Aluminum Oxide Rotary Kiln. *Industrial Engineering and Chemical, Process Design and Development*, 13, 2, 1974, S.132 - 142
- (40) Martins, M.A.; Oliveira, L.S.; Franca, A.S.: Modeling and simulation of petroleum coke calcination in rotary kilns. *Fuel*, 2001, 80, pp.1611-22.
- (41) Mastorakos E.; Massias, A.; Tsakiroglou, CD.; Goussis, D.A.; Burg-anos V.N.; Payatakes, A.C: CFD predictions for cement kilns including flame modeling, heat transfer and clinker chemistry. *Applied Mathematical Modelling*, 23, 1999, S.55–76
- (42) Mazumdar, S.; Mukherjee, B.: Structural Characterization of the Spinel Phase in the Kaolin-Mullite Reaction Series through Lattice Energy. *Journal of the American Ceramic Society*, 1983, 66(9), pp.610-12.
- (43) Mellmann, J.:The transverse motion of solids in rotating cylinders - forms of motion and transition behavior. *Powder Technology*, 118, 2001, S.251-270
- (44) USGS. Geological Survey Mineral Commodity Summaries. Retrieved March 17, 2008, January, from <http://minerals.usgs.gov/minerals/pubs/commodity/magnesium>
- (45) Mintus, F.; Hamel, S.; Krumm, W: Wet Process Rotary Cement Kilns, Modeling and Simulation. *Clean Tech. Environ. Policy*, 2006, 8(2), 112-122
- (46) Morimoto, T.; Nagao M.; Omori T.: Heat of immersion of titanium dioxide in water. 1. The effect of the hydration treatment of titanium dioxide. *Bulletin of the Chemical Society of Japan*, 1969, 42(4):943–946.
- (47) Moulin E.; Blanc P.; Sorrentino D.: Influence of key cement chemical parameters on the properties of metakaolin blended cements. *Cem Concr Compos*, 1995, 23(6), 463–9.
- (48) Moulin E.; Blanc P.; Sorrentino D.: Influence of key cement chemical parameters on the properties of metakaolin blended cements. *Cem Concr Compos*, 2001, 23(6), 463–9.
- (49) Mujumdar, K.S.; Ranade, V.V.: Simulation of Rotary Cement Kilns Using a One-Dimensional Model. *Chemical Engineering Research and Design*, 2006, 84(A3), 165-177.
- (50) Murrar Haydn H.: Traditional and new applications for kaolin, smectite. palygorskite: a general overview. *Appl Clay Sci*, 2000, 17:207–21.

- (51) Murray, H.H.: In Ullmann's encyclopedia of industrial chemistry. Weinheim, Wiley-VCH Verlag GmbH & Co, 2007, pp.203-35. 171.
- (52) Murray, H.H.: Industrial Applications of Kaolin. Georgia Kaolin Company, Elizabeth, 2007
- (53) Murray, H.H.; Kogel, J.E.: Engineered clay products for the paper industry. Applied Clay Science, 2005, 29, pp.199-206.
- (54) Nkoumbou C.; Njoya A.; Njoya D.; Grosbois C.; Njopwouo D.; Yvon J.: Kaolin from Mayouom (Western Cameroon). Industrial suitability evaluation. Appl Clay Sci, 2009, 43:118–24.
- (55) Nørskov, L.K.; Dam-Johansen, K.; Glarborg, P.; Jensen, P.A.; Larsen, M.B. Combustion of solid alternative fuels in the cement kiln burner. Ph.D. thesis, Technical University of Denmark, Kgs. Lyngby, 2012
- (56) Oates, J.A.H.: Lime and limestone, chemistry and technology production uses, Weinheim: Wiley-VCH, 1998.
- (57) Omori, T.; Imai, J.; Nagao, M.; Morimoto, T.: Heat of immersion of titanium dioxide in water. II. The effect of the crystallinity of anatase. B. Chem. Soc. Jpn. 42 (8), 1969, 2198–2202.
- (58) Ongstad, I.; Haugerod, O.; Mezzetta, G.: Environmental Aspects of Magnesium Production by Electrolysis. Proceedings of International Symposium on Advances in Production and Fabrication of Light Metals and Metal Matrix Composites, 1992
- (59) Pan Yongxin.; Zhu Rixiang.: Low-Temperature Magnetic Behavior related to Thermal Alteration of Siderite, Geophysical Research Letters (29), 2002, 1-4.
- (60) Pearce, K.W.: A heat transfer model for rotary kilns. Journal of institute of fuel, 7, 1973, S.363-371
- (61) Peray, K.E.; Waddell, J.J.: The rotary cement kiln. Chemical Publishing Co., Inc, New York, 1972
- (62) Perry, R.H.; Green, D.W.: Chemical Engineer Handbook. New York, McGraw-Hill, 1999
- (63) Pervushin, V. Y.; Denisova T. A.; Tolchev A. V.; Marchenko V. P.; Pletnev R. N.; Tyustin V. A.; Kleshchev D. G.: Structural changes in hydrated titanium dioxide during aging in air and heat treatment. Russian Journal of Applied Chemistry, 2002, 75(5):696-699.
- (64) Peterson, R.D.; Newton, L.: Review of Aluminum Dross Processing, Light Metals, TMS-AIME, Warrendale, 2002, PA, pp.1029
- (65) Ptacek, P. et al.: Isothermal kinetic analysis of the thermal decomposition of kaolinite: The thermogravimetric study. Thermochemica Acta, 2010, 501, pp.24-29.
- (66) Ptacek, P. et al.: The kinetics of Al-Si spinel phase crystallization from calcined kaolin. Journal of Solid State Chemistry, 2010, 183, pp.2565-69.
- (67) Ptacek, P. et al.: The kinetic analysis of the thermal decomposition of kaolinite by DTG technique. Powder Technology, 2011, 208, pp.20-25.

- (68) Ptacek, P. et al.: The kinetics and mechanism of kaolin powder sintering I. The dilatometric CRH study of sinter-crystallization of mullite and cristobalite. *Powder Technology*, 2012, 232, pp.24-30.
- (69) Ptacek, P. et al.: The influence of structure order on the kinetics of dehydroxylation of kaolinite. *Journal of the European Ceramic Society*, 2013, 33(13-14), pp.2793-99.
- (70) Sadighi, S.; Shirvani, M.; Arshad, A.; Rotary Cement Kiln Coating Estimator. *The Canadian Journal of Chemical Engineering*, 89, 2011, 116-125
- (71) Saeman, W.C.: Passage of solid through rotary kilns:factors affecting time passage. *Chemical Engineering Progress*, 47, 10, 1951, S.508-514.
- (72) Samson Oluropo Adeosun.; Olatunde Israel Sekunowo.; Omotayo Oluwaseyi Taiwo.; Wasiu Ajibola Ayoola.; Adebowale Machado.:Physical and Mechanical Properties of Aluminum Dross. *Advances in Materials*, 2014, Vol. 3, No. 2, pp. 6-10.doi: 10.11648/j.am.20140302.11
- (73) Sass, A.: Simulation of the heat-Transfer Phenomena in a Rotary Kiln. *Industrial and Engineering Chemical Process Design and Development*, 6, 4, 1967, S.532-535.
- (74) Schlunder, E.-U.; Mollekopf, N.: Vacuum contact drying of free flowing mechanically agitated particulate material. *Chemical Engineering and Processing*, 1984, 18(2), 93-111.
- (75) Schupe, W.: Vereinfachte Berechnung des Strahlungswärmeübergangs in Industrieöfen und Vergleich mit Messungen in einer Versuchsbrennkammer. Dissertation, Technische Universität Clausthal, 1974
- (76) Shannon, R.D.; Pask, J.A.: Kinetics of the anatase-rutile transformation. *J. Am. Ceram. Soc.* 48 (8), 1965, 391-398.
- (77) Sivertsen, L. V.; Haagensen, J. O.; Albright, D.: A Review of Life Cycle Environmental Performance of Automotive Magnesium. *Sustainability of Environmental Systems and Materials*. SAE Technical Paper, SAE World Congress, 2003, 01-0641.
- (78) Spang, H.A.: A dynamic model of a cement kiln. *Automatica*, 8, 1972,S.309-323
- (79) Specht E : Kinetik der Abbaureaktionen Habilitationsschrift, TU Clausthal, 1993
- (80) [Specht et al. (1986)] Specht, E.; Kainer, H.; Jeschar, R.: Die Reaktions- Porendiffusions-
- (81) Sullivan, W. F.; Cole, S. S.: Thermal chemistry of colloidal titanium dioxide. *Journal of the American Ceramic Society*, 1959, 42, 127–133.
- (82) Taylor, H.F.W.: *Cement Chemistry*. Academic Press, 1990
- (83) Teodorovich G. I.; *Authigenic Minerals in Sedimentary Rocks*, USSR Academy of Sciences Press, 1961
- (84) Thomas, R.; *High temperature processing of kaolinitic materials*. PhD Thesis. University of Birmingham, 2010
- (85) Thurlow, C.: *China clay from Cornwall and Devon, An illustrated account of the modern China Clay Industry*, 2005, 4th ed. St Austell: Cornish Hillside Publications.
- (86) Udupa, M. R.: Thermal decomposition of Cerium (IV), Cerium(III), Chromium(III) and Titanium(IV) Sulphates. *Thermochimica Acta*, 1982, 57(3):377–381.

- (87) Vasconcelos C.; McKenzie J. A.; Bernasconi S.; Grujic D.; Tien A. J. : Microbial mediation as a possible mechanism for natural dolomite formation at low temperatures. Nature 337:220-222. Bibcode: 1995 Natur. 377. 220V. Doi:10.1038/377220a0.
- (88) Venkatesh, V.: Lime Reburning. The rotary lime kiln. Chemical recovery in the alkaline pulping processes, Revised Edition, Co-Edited by Robert P. Green and Gerald Hough, 1992
- (89) Wingate, M.: Small-scale Lime-burning, A Practical Introduction, London, Intermediate Technology Publications, 1985
- (90) Wocadlo, T.: Experimentelle Untersuchung und mathematische Modellierung eines großtechnischen Pyrolyse-Drehrohrofens zur Reinigung kontaminierter Böden. VDI-Verlag, 1994-136
- (91) Woche, H.; Specht, E.; Schmidt, J.: Local heat transfer in tubes after sudden change of diameter. Chemical Engineering Technology, Vol. 28, No.6, 2005, S.677-683
- (92) Woche, H.; Specht, E.; Schmidt, J.: Wärmeübergang im Einlaufbereich von Rohren . Kälte Luft Klimatechnik, 2007, S.37-41
- (93) Sai, P., S., T., Surender, G., D., Damodaran, A., D., Suresh, V., Philip, Z., G., Sankaran, K., "Residence time distribution and material flow studies in a rotary kiln", Metall. Trans. B, 21B, 1005-1011 (1992).

Internet web links

<http://minerals.usgs.gov/minerals/pubs/commodity/cement/mcs-2011-cemen.pdf>

<http://www.cembureau.be/topics>

<https://www.vdz-online.de/en/topics/cement-sector>

<https://www.statista.com/search/?q=magnesite>

<http://www.essentialchemicalindustry.org/chemicals/titanium-dioxide.html>

<https://minerals.usgs.gov/minerals/pubs/commodity/clays/mcs-2016-clays.pdf>

http://www.rpublication.com/ijeted/ijeted_index.htm ISSN 2249-6149

Appendix A

A.1 Input parameters for the aluminum dross in a pilot kiln.

Parameter	Value	Unit
Rotary kiln		
Length L	5.0	m
Internal diameter (process) D	0.4	m
Inclination β	2	°
Rotational speed n	1	rpm
Burner		
Fuel type	Natural gas	—
Power P	100	kW
Air excess number λ	2	—
Combustion air temperature	20	°C
Flame length L_{Flame}	0.4	m
Bulk Material		
Mass flow \dot{M}_s	50	kg/h
Temperature of the feed $T_{s,0}$	22	°C
Average particle diameter d_p	50	μm
Dynamic angle of repose Θ	44	°
Specific heat capacity $c_{p,s}$	1000	J/kg/K
Density ρ_s	1260	kg/m ³
Thermal conductivity λ_s	1	W/m/K
Emissivity of the solid ε_s	0.6	—
Lining / wall		
Thickness of refractory $s_{w,1}$	80	mm
Thickness of high temperature insulation $s_{w,2}$	70	mm
Thermal conductivity refractory $\lambda_{w,1}$	1.5	W/m/K
Thermal conductivity insulation $\lambda_{w,2}$	0.7	W/m/K
Density refractory $\rho_{w,1}$	2500	kg/m ³
Specific heat capacity $c_{p,w,1}$	990	J/kg/K
Emissivity of the inner wall surface	0.9	—
Surroundings		
Temperatur T_U	20	°C
Air velocity w_U	2	m/s

A.2 Simulation results for aluminium dross calcination

Parameter	Reference state
$T_{G,max}$	1175°C
$T_{G,0}$	656°C
$T_{S,max}$	1119°C
$T_{S,L}$	811°C
$U_{calcination}$	100%
$U_{oxidation}$	100%
Product rate	$\dot{M}_{S,L} = 45 \text{ kg/h}$ ($E_S = 8 \text{ MJ/kg}_{Product}$)
MRT	97.4 min
F_{max}	15.8%
Wall heat loss	16 kW (16%)

Appendix B

B.1 Input parameters for the Siderite in a pilot kiln

Parameter	Value	Unit
Rotary kiln		
Length L	5.0	m
Internal diameter (process) D	0.4	m
Inclination β	1	°
Rotational speed n	0.6	rpm
Burner		
Fuel type	Natural gas	—
Power P	100	kW
Air excess number λ	1.2	—
Combustion air temperature	20	°C
Flame length L_{Flame}	0.4	m
Bulk Material		
Mass flow \dot{M}_S	40	kg/h
Temperature of the feed $T_{S,0}$	22	°C
Average particle diameter d_p	50	μm
Dynamic angle of repose Θ	37	°
Specific heat capacity $c_{p,s}$	1000	J/kg/K
Density ρ_s	2240	kg/m ³
Thermal conductivity λ_s	1	W/m/K
Emissivity of the solid ε_s	0.6	—
Lining / wall		
Thickness of refractory $s_{w,1}$	80	mm
Thickness of high temperature insulation $s_{w,2}$	70	mm
Thermal conductivity refractory $\lambda_{w,1}$	1.5	W/m/K
Thermal conductivity insulation $\lambda_{w,2}$	0.7	W/m/K
Density refractory $\rho_{w,1}$	2500	kg/m ³
Specific heat capacity $c_{p,w,1}$	990	J/kg/K
Emissivity of the inner wall surface	0.9	—
Surroundings		
Temperatur T_U	20	°C
Air velocity w_U	2	m/s

B.2 Simulation results for Siderite calcination

Parameter	Reference state
$T_{G,max}$	1200°C
$T_{G,0}$	680°C
$T_{S,max}$	1090°C
$T_{S,L}$	800°C
$U_{calcination}$	100%
$U_{oxidation}$	100%
Product rate	$\dot{M}_{S,L} = 28.7 \text{ kg/h}$ ($E_S = 12.5 \text{ MJ/kg}_{\text{Product}}$)
MRT	84.7 min
F_{max}	11%
Wall heat loss	15 kW (15%)

Appendix C

C.1 Input parameters for the magnesite industrial kiln [Ludera (1974)]

Parameter	Value	Unit
Rotary kiln		
Length L	90	m
Internal diameter (process) D	3.04	m
Inclination β	1	°
Rotational speed n	1	rpm
Burner		
Fuel type	Coal	—
Power P	18.5	MW
Air excess number λ	1.3	—
Combustion air temperature	20	°C
Flame length L_{Flame}	20	m
Bulk Material		
Mass flow \dot{M}_s	25	t/h
Temperature of the feed $T_{s,0}$	420	°C
Average particle diameter d_p	28	mm
Dynamic angle of repose Θ	40	°
Specific heat capacity $c_{p,s}$	1200	J/kg/K
Density ρ_s	1442	kg/m ³
Thermal conductivity λ_s	0.7	W/m/K
Emissivity of the solid ε_s	0.3	—
Lining / wall		
Thickness of refractory $s_{w,1}$	75	mm
Thickness of high temperature insulation $s_{w,2}$	104	mm
Thermal conductivity refractory $\lambda_{w,1}$	1.5	W/m/K
Thermal conductivity insulation $\lambda_{w,2}$	0.7	W/m/K
Density refractory $\rho_{w,1}$	2600	kg/m ³
Specific heat capacity $c_{p,w,1}$	1000	J/kg/K
Emissivity of the inner wall surface	0.9	—
Surroundings		
Temperatur T_U	20	°C
Air velocity w_U	5	m/s

C.2 Simulation results for magnesite calcination

Parameter	Reference state
$T_{G,max}$	1761°C
$T_{G,0}$	488°C
$T_{S,max}$	1649°C
$T_{S,L}$	860°C
U_{MgCO_3} (calcination)	100%
Product rate	$\dot{M}_{S,L} = 12$ t/h ($E_S = 5.5$ MJ/kg Product)
F_{max}	20%
Wall heat loss	2.36 MW (12.7%)

Appendix D

D.1 Input parameters for the dolomite industrial [Ludera (1974)]

Parameter	Value	Unit
Rotary kiln		
Length L	119	m
Internal diameter (process) D	2.85	m
Inclination β	2.0	°
Rotational speed n	1.0	rpm
Burner		
Fuel type	Coal	—
Power P	40.5	MW
Air excess number λ	1.3	—
Combustion air temperature	20.0	°C
Flame length L_{Flame}	18.0	m
Bulk Material		
Mass flow \dot{M}_s	40.7	t/h
Temperature of the feed $T_{s,0}$	22	°C
Average particle diameter d_p	30	mm
Dynamic angle of repose Θ	33	°
Specific heat capacity $c_{p,s}$	1200	J/kg/K
Density ρ_s	1590	kg/m ³
Thermal conductivity λ_s	0.8	W/m/K
Emissivity ε_s	0.5	—
Lining / wall		
Thickness of refractory $s_{w,1}$	70	mm
Thickness of high temperature insulation $s_{w,2}$	20	mm
Thermal conductivity refractory $\lambda_{w,1}$	1.4	W/m/K
Thermal conductivity insulation $\lambda_{w,2}$	0.6	W/m/K
Density refractory $\rho_{w,1}$	2645	kg/m ³
Specific heat capacity $c_{p,w,1}$	986	J/kg/K
Emissivity of the inner wall surface	0.6	—
Surroundings		
Temperatur T_U	20	°C
Air velocity w_U	2	m/s

D.2 Simulation results for dolomite calcination

Parameter	Reference state
$T_{G,\max}$	2049°C
$T_{G,0}$	611°C
$T_{S,\max}$	2022°C
$T_{S,L}$	1245°C
$U_{\text{CaCO}_3 \cdot \text{MgCO}_3}$ (calcination)	100%
$U_{\text{MgO CaCO}_3}$ (calcination)	100%
Product rate	$\dot{M}_{S,L} = 23.69 \text{ t/h}$ ($E_S = 6.1 \text{ MJ/kg}_{\text{Product}}$)
MRT	242 min
F_{\max}	15.7%
Wall heat loss	3.9 MW (9.85%)

Appendix E

E.1 Input parameters for titanium dioxide industrial kiln [Ptacek et al (2012)]

Parameter	Size	Unit
Rotary kiln		
Length L	45	m
Internal diameter (process) D	2.3	m
Inclination β	3	$^{\circ}$
Rotational speed n	0.33	rpm
Burner		
Fuel type	Natural gas	—
Power P	4.3	MW
Air excess number λ	1.3	—
Combustion air temperature	169	$^{\circ}\text{C}$
Flame length L_{Flame}	0	m
Bulk Material		
Mass flow \dot{M}_s	8.25	t/h
Temperature of the feed $T_{s,0}$	45	$^{\circ}\text{C}$
Average particle diameter d_p	20	μm
Dynamic angle of repose Θ	37	$^{\circ}$
Specific heat capacity $c_{p,s}$	1025	J/kg/K
Density ρ_s	2650	Kg/m ³
Thermal conductivity λ_s	0.439	W/m/K
Emissivity of the solid ε_s	0.8	—
Lining / wall		
Thickness of refractory $s_{w,1}$	130	mm
Thickness of high temperature insulation $s_{w,2}$	120	mm
Thermal conductivity refractory $\lambda_{w,1}$	1.7	W/m/K
Thermal conductivity insulation $\lambda_{w,2}$	0.7	W/m/K
Density refractory $\rho_{w,1}$	2310	Kg/m ³
Specific heat capacity $c_{p,w,1}$	950	J/kg/K
Emissivity of the inner wall surface	0.9	—
Surroundings		
Temperatur T_U	15	$^{\circ}\text{C}$
Air velocity w_U	1.33	m/s

E.2 Simulation results for titanium dioxide production.

Parameter	Reference state
$T_{G,max}$	1038°C
$T_{G,0}$	421°C
$T_{S,max}$	933°C
$T_{S,L}$	933°C
$U_{S,Evaporation}$	100%
$U_{S,Dehydration}$	100%
$U_{S,Desorption}$	100%
$U_{S,Desulphurisation}$	100%
$U_{S,Rutilisation}$	100%
Product rate	$\dot{M}_{S,L} = 3.68 \text{ t/h}$ ($E_S = 4.1 \text{ MJ/kg}_{Product}$)
MRT	212 min
F_{max}	6.9%
Heat loss	0.53 MW (13%)

Appendix F

F.1 Input parameters for the Cement industrial kiln

Parameter	Value	Unit
Rotary kiln		
Length L	60.0	m
Internal diameter (process) D	3.6	m
Inclination β	2.29	°
Rotational speed n	3.8	rpm
Burner		
Fuel type	Coal	—
Power of calciner P_{calciner}	73.5	MW
Power of burner P_{burner}	38.7	MW
Total power P	112.2	MW
Air excess number λ	1.3	—
Combustion air temperature	696	°C
Flame length L_{Flame}	10.0	m
Bulk Material		
Mass flow \dot{M}_S	129	t/h
Temperature of the feed $T_{S,0}$	890	°C
Average particle diameter d_p	200	μm
Dynamic angle of repose Θ	36.5	°
Specific heat capacity $c_{p,s}$	1090	J/kg/K
Density ρ_s	1100	Kg/m ³
Thermal conductivity λ_s	0.4	W/m/K
Emissivity ε_s	0.4	—
Lining / wall		
Thickness of refractory $s_{W,1}$	150	mm
Thickness of high temperature insulation $s_{W,2}$	100	mm
Thermal conductivity refractory $\lambda_{w,1}$	1.6	W/m/K
Thermal conductivity insulation $\lambda_{w,2}$	0.6	W/m/K
Density refractory $\rho_{w,1}$	3142	Kg/m ³
Specific heat capacity $c_{p,w,1}$	1100	J/kg/K
Emissivity of the inner wall surface	0.8	—
Surroundings		
Temperatur T_U	20	°C
Air velocity w_U	2.0	m/s

F.2 The composition of cement

Parameter	Size %
CaCO ₃	79.2
SiO ₂	15
Fe ₂ O ₃	4.5
Al ₂ O ₃	1.3

F.3. Simulation results for cement calcination

Parameter	Reference
T _{G,max}	1905°C
T _{G,0}	952°C
T _{S,max}	1443°C
T _{S,L}	1370°C
Product rate	$\dot{M}_{S,L} = 117.5 \text{ t/h}$ ($E_S = 3.4 \text{ MJ/kg}_{\text{Product}}$)
MRT	22 min
F _{max}	7.4%
Wall heat loss	4.7 MW (12%)

Appendix G

G.1 Input parameters for the limestone industrial kiln.

Parameter	Value	Unit
Rotary kiln		
Length L	86	m
Internal diameter (process) D	3.05/2.92	m
Inclination β	3	°
Rotational speed n	1.45	rpm
Burner		
Fuel type	Coal	—
Power P	38	MW
Air excess number λ	1.06	—
Combustion air temperature	445	°C
Flame length L_{Flame}	20	m
Bulk Material		
Mass flow \dot{M}_s	45	t/h
Temperature of the feed $T_{s,0}$	850	°C
Average particle diameter d_p	26	mm
Dynamic angle of repose Θ	40	°
Specific heat capacity $c_{p,s}$	1090	J/kg/K
Density ρ_s	1540	kg/m ³
Thermal conductivity λ_s	0.3	W/m/K
Emissivity of the solid ε_s	0.3	—
Lining / wall		
Thickness of refractory $s_{w,1}$	160	mm
Thickness of high temperature insulation $s_{w,2}$	40	mm
Thermal conductivity refractory $\lambda_{w,1}$	3	W/m/K
Thermal conductivity insulation $\lambda_{w,2}$	0.6	W/m/K
Density refractory $\rho_{w,1}$	2600	kg/m ³
Specific heat capacity $c_{p,w,1}$	1100	J/kg/K
Emissivity of the inner wall surface	0.8	—
Surroundings		
Temperatur T_U	20	°C
Air velocity w_U	5	m/s

G.2 Simulation results for limestone calcination

Parameter	Reference state
$T_{G,max}$	1556°C
$T_{G,0}$	563°C
$T_{S,max}$	1040°C
$T_{S,L}$	961°C
$U_{CaCO_3}(\text{calcination})$	100%
Product rate	$\dot{M}_{S,L} = 24.7189 \text{ t/h}$ ($E_S = 5.5 \text{ MJ/kg}_{\text{Product}}$)
MRT	84.7 min
F_{max}	6.6%
Wall heat loss	5 MW (13%)

Appendix H

H.1 Input parameters for kaolin industrial kiln.

Parameter	Value	Unit
Rotary kiln		
Length L	34	m
Internal diameter (process) D	2.1	m
Inclination β	1.7	°
Rotational speed n	1.4	rpm
Burner		
Fuel type	Natural gas	—
Power P	2.88	MW
Air excess number λ	1.12	—
Combustion air $\dot{M}_{\text{air,total}}$	3975	kg/h
Combustion air temperature	470	°C
Flame length $L_{\text{Flame, Nozzle}}$	12,0.5	m
Bulk Material		
Mass flow \dot{M}_s	3.982	t/h
Temperature of the feed $T_{s,0}$	400	°C
Average particle diameter d_p	3	μm
Dynamic angle of repose Θ	30	°
Specific heat capacity $c_{p,s}$	$318.3 \cdot (T_s)^{0.1939}$	J/kg/K
Density ρ_s	290...350	kg/m ³
Thermal conductivity λ_s	0.1	W/m/K
Emissivity of the solid ε_s		—
Lining / wall		
Thickness of refractory $s_{w,l}$	300	mm
Thickness of shell	30	mm
Thermal conductivity refractory $\lambda_{w,l}$	1.8	W/m/K
Density refractory $\rho_{w,l}$	2520	kg/m ³
Specific heat capacity $c_{p,w,l}$	1000	J/kg/K
Emissivity of the inner wall surface	0.5	—
Surroundings		
Temperatur T_U	15	°C
Air velocity w_U	1.33	m/s

H.2 Simulation results for kaolin

Parameter	Reference state
$T_{G,max}$	1556°C
$T_{G,0}$	563°C
$T_{S,max}$	1177°C
$T_{S,L}$	921°C
$U_{Dehydroxylation}$	100%
$U_{Spinell}$	100%
U_{Mullit}	18%
Product rate	$\dot{M}_{S,L} = 3.2 \text{ t/h}$ ($E_S = 3.2 \text{ MJ/kg}_{Product}$)
MRT	63 min
F_{max}	14.3%
Heat loss	0.52 MW (13%)

List of Publications

- (1) Herz, F.; Specht, E.; Abdelwahab, A.: Modeling and validation of the siderite decomposition in a rotary kiln. Proceedings of the 11th European Conference on Industrial Furnaces and Boilers (INFUB 2017), April 18-21, 2017, Albufeira, Portugal
- (2) Herz, F.; Specht, E.; Abdelwahab, A.: Simulation of lime burning in rotary kilns. Cement International accepted April 2017
- (3) Herz, F.; Specht, E.; Abdelwahab, A.: Modeling and validation of the siderite decomposition in a rotary kiln. Energy Procedia accepted April 2017

Curriculum vitae

Personal Information

Name	Abdulkadir Ahmed Alnour Alnadif Abdelwahab
Nationality	Libyan
Date of birth	25.04.1977
Place of birth	Algrifa, Libya
Marital Status	Married

Education

1995-2000	B.Sc Mechanical Engineering (Power Engineering), Altahady University College of Engineering Technology, Hoon -Libya.
2005-2007	M.Sc Mechanical Engineering, Faculty of Engineering and Technology, Arab Academy for Science Technology, Alexandria- Egypt
2014- Present	Ph.D study , Institute of fluid Dynamics and Thermodynamics, Otto von Guericke University Magdeburg, Germany